VILNIUS UNIVERSITY
CENTER FOR NATURAL SCIENCES AND TECHNOLOGY

Nail
GAREJEV

Extreme Light-Matter Interaction in Solid-State Dielectric Media with Ultrashort Mid-IR Laser Pulses

DOCTORAL DISSERTATION

Natural Sciences
Physics N 002

VILNIUS 2019

This dissertation was written between 2015 and 2019 at Vilnius University, Laser Research Center. The research was supported by the Research Council of Lithuania.

Academic supervisor:
Prof. Habil. Dr. Audrius Dubietis (Vilnius University, Natural Sciences, Physics, N 002)

Dissertation Defense Panel:

Chairman – Habil. Dr. Virgilijus Vaičaitis (Vilnius University, Natural Sciences, Physics, N 002)

Members:
Assoc. Prof. Dr. Rytis Butkus (Vilnius University, Natural Sciences, Physics, N 002)
Assoc. Prof. Dr. Vygandas Jarutis (Vilnius University, Natural Sciences, Physics, N 002)
Assoc. Prof. Dr. Domas Paipulas (Vilnius University, Natural Sciences, Physics, N 002)
Prof. Habil. Dr. Kęstutis Staliūnas (Universitat Politecnica de Catalunya, Natural Sciences, Physics, N 002)

The dissertation shall be defended at a public meeting of the Dissertation Defense Panel at 13:00 on 27 September 2019 in Room 306 of the Laser Research Center.
Address: Saulėtekio al. 10, Lazerinių tyrimų centras, Room 306, Vilnius, Lithuania.
Tel. +370 5 236 6005;

The text of this dissertation can be accessed at the Vilnius University Library, as well as on the website of Vilnius University:
www.vu.lt/naujienos/ivykiu-kalendorius

VILNIAUS UNIVERSITETAS
FIZINIŲ IR TECHNOLOGIJOS MOKSLŲ CENTRAS

Nail
GAREJEV

Ekstremalioji šviesos ir medžiagos sąveika kietakūniuose dielektrikuose žadinant viduriniosios IR ultratrumpaisiais lazerio impulsais

DAKTARO DISERTACIJA

Gamtos mokslai
Fizika N 002

VILNIUS 2019

Disertacija rengta 2015–2019 metais Lazerinių tyrimų centre, Vilniaus universitete. Mokslinius tyrimus rėmė Lietuvos mokslo taryba.

Mokslinis vadovas:
prof. habil. dr. Audrius Dubietis (Vilniaus universitetas, gamtos mokslai, fizika, N 002)

Gynimo taryba:

Pirmininkas – habil. dr. Virgilijus Vaičaitis (Vilniaus universitetas, gamtos mokslai, fizika, N 002)

Nariai:
doc. dr. Rytis Butkus (Vilniaus universitetas, gamtos mokslai, fizika, N 002)
doc. dr. Vygandas Jarutis (Vilniaus universitetas, gamtos mokslai, fizika, N 002)
doc. dr. Domas Paipulas (Vilniaus universitetas, gamtos mokslai, fizika, N 002)
prof. habil. dr. Kęstutis Staliūnas (Katalonijos politechnikos universitetas, gamtos mokslai, fizika, N 002)

Disertacija ginama viešame Gynimo tarybos posėdyje 2019 m. Rugsėjo mėn. 27 d. 13:00 val. fizikos fakulteto lazerinių tyrimų centro 306 auditorijoje. Adresas: Saulėtekio al. 10, Lazerinių tyrimų centras, 306 aud., Vilnius, Lietuva. Tel. +370 5 236 6005;

Disertaciją galima peržiūrėti Vilniaus universiteto bibliotekoje ir VU interneto svetainėje adresu: www.vu.lt/naujienos/ivykiu-kalendorius

ACKNOWLEDGEMENTS

First of all, I would like to express extreme gratitude to my supervisor, prof. habil. dr. Audrius Dubietis. He has provided great guidance throughout the years and it is hard to imagine a better supervisor. Prof. Dubietis is also an outstanding team leader, who has gathered a wonderful scientific group and has been working tirelessly to make it very productive.

Assoc. prof. dr. Gintaras Tamošauskas has been indispensable for the experimental measurements. He conducted maintenance that kept equipment running with minimal downtime and his advice helped with faster assembly of high quality experimental setups. Additionally, a lot of diagnostic and automation equipment has been created by him.

Assoc. prof. dr. Vytautas Jukna and prof. dr. Gintaras Valiulis performed numerical simulations that helped to explain experimental data.

Experimental scientific work benefited from additional ideas and hands on the spot. It was great doing experiments together with PhD stud. Rosvaldas Šuminas, PhD stud. Agnė Marcinkevičiūtė, Milda Veličkė and Ieva Gražulevičiūtė. For the assistance in less interesting, yet necessary tasks, I am thankful for the help provided by Domas Kudarauskas, Gvidas Beresnevičius and Julius Lukošiūnas.

I thank dr. Donatas Majus for inviting me to the team and introducing me to the field of laser physics; dr. Julius Darginavičius for being my first scientific supervisor during my bachelor studies years; dr. Justinas Galinis for the advice on scientific and technical matters.

Thanks to prof. dr. Mikas Vengris for helping with some equipment and experiments.

Thanks to dr. Akvilė Zabiliūtė-Karaliūnė for a well made initial LaTeX dissertation template.

Finally, I thank my family for supporting and helping me all these years.

This research was partly funded by grants (APP-8/2016, DOK-16439, DOK-17452, P-DAP-19-203) from the Research Council of Lithuania and a grant (VP1-3.1-ŠMM-07-K-03-001) from the European Social Fund under the Global Grant measure.

CONTENTS

LIST OF ABBREVIATIONS

BBO	Beta barium borate, β-BaB_2O_4
CaF_2	Calcium fluoride
CCD	Charge-coupled device
CEP	Carrier-envelope phase
CMOS	Complementary metal–oxide–semiconductor
FS	Fused silica
FWHM	Full width at half maximum
FWM	Four-wave mixing
GVD	Group velocity dispersion
GVM	Group velocity mismatch
IR	Infrared
LiF	Lithium fluoride
OPA	Optical parametric amplification
OPCPA	Optical parametric chirped-pulse amplification
SC	Supercontinuum
SH	Second harmonic
SHG	Second harmonic generation
SPM	Self-phase modulation
TH	Third harmonic
THG	Third harmonic generation
UV	Ultraviolet
XPM	Cross-phase modulation
YAG	Yttrium aluminium garnet

INTRODUCTION

The process of filamentation induced by the propagation of intense femtosecond laser pulses in transparent dielectric media displays universal features, such as long distance propagation that results in self-cleaning and robustness of the spatial mode and produces a narrow plasma channel in its wake, which are universal and do not depend on the physical state of the nonlinear medium. In the time domain, beam filamentation leads to a shock front formation, pulse splitting and compression [1]. Structurally, the light filament consists of mutually interacting compact high intensity core and a large low intensity peripheral energy reservoir, which contains most of the energy. Collective action of nonlinear losses (multiphoton absorption and ionization), self-focusing and diffraction reshapes the incident Gaussian input beam into a Bessel-like beam [2,3]. Long sub-diffractive propagation of the central core and the corresponding ultrashort pulse in the time domain is only possible due to the conical energy flux from the beam periphery [4].

Perhaps the most spectacular and visually perceptible manifestation of filamentation phenomenon is supercontinuum (SC) generation, resulting in a broadband, spatially and temporally coherent radiation with low angular divergence, which is surrounded by a colored conical radiation emitted at different angles with respect to the propagation axis. Supercontinuum is a unique and useful source of ultra-broadband radiation possessing high spectral power density and high coherence comparable to a white-light laser [5]. Supercontinuum generation in bulk dielectric media is a very practical, compact, efficient and reliable method for obtaining coherent broadband radiation in different parts of the optical spectrum, which finds diverse applications in the fields of time-resolved spectroscopy, ultrafast nonlinear optics and photonics [6–9].

SC generation with femtosecond laser pulses in various solid-state dielectric media in the range of normal group velocity dispersion (GVD) was widely studied experimentally and numerically, and its physical mechanism is understood fairly well. The catastrophic self-focusing is halted by the pulse splitting, which is a space-time effect and occurs at the nonlinear focus of the beam [10]. The split sub-pulses subsequently undergo self-steepening of the pulse fronts due to the interplay between the nonlinear effects and chromatic dispersion, inducing sharp intensity gradients (optical shocks) in the temporal profiles of sub-pulses, which give rise to an explosive broadening of the spectrum, i.e. SC generation. More precisely, the red-shifted frequencies are generated by self-steepening of the ascending front of the leading sub-pulse, whereas the blue-shifted frequencies are generated by self-steepening of the descending front of the trailing sub-pulse. As a result, the leading and trailing sub-pulses acquire different carrier frequencies and propagate with different group velocities [11].

Recent advances in the development of high-peak-power near- and mid-infrared ultrashort-pulse laser sources, which are exclusively based on the optical parametric amplification [12–14], provide the possibility to experimentally study filamentation phenomena in wide bandgap solid state dielectric materials, in the range of their anomalous GVD. To this end, a remarkably (almost by 10 times) increased length of the filaments [15] and ultrabroadband SC emission [16] was observed by launching femtosecond pulses at 1.55 µm into fused silica samples. Recent measurements of filamentation in the YAG crystal, pumped by much longer wavelength pulses (3.1 µm) showed SC spectrum spanning over 3 octaves from the ultraviolet to the mid-infrared spectral range [17].

In light of these observations, propagation of intense femtosecond laser pulses in transparent dielectrics with anomalous GVD was shown to favor a new filamentation regime, in which both self-focusing of the beam and pulse compression in time happen together due to the interplay between self-phase modulation and anomalous GVD. In this regime, self-compression of the pulses down to few optical cycles could be achieved [18,19], leading to the formation of spatiotemporal light bullets – self-compressed nonlinear structures that propagate quasistationarily over distances exceeding many diffraction and dispersion lengths [20], or recurrent self-compression cycles at higher input energy [21]. High dynamic range measurements of spatiotemporal structure, energy density fluxes, sub-diffractive and dispersive propagation in free space show that light bullets exhibit the features of polychromatic Bessel-like beams, clearly distinguishing them from soliton-like objects [22]. An unprecedented spectral coverage of the light bullet-induced SC [23] currently attracts a great deal of scientific and technological interest. This interest is inspired by the time-resolved spectroscopy in the molecular fingerprint region and in particular, by the applications in the emerging field of ultrafast mid-infrared nonlinear optics, offering an easy way for production of few optical cycle pulses, which could be further shaped and/or parametrically amplified up to very high peak powers, see e.g. [24,25].

On the other hand, filamentation of mid-infrared laser pulses produces multiple odd harmonics, whose wavelengths fall into the near-infrared, visible and ultraviolet, i.e. into the transparency range of the nonlinear dielectric media, where they could be readily detected by simple means. To this end, generation of third, fifth [26–28] and seventh [29] harmonics by filamentation of mid-infrared laser pulses in air was recently experimentally observed. Some experimental observations of low-order odd harmonics were also reported in semiconductors [30], and in liquid [31,32] and solid state [33–35] dielectric media. Understanding the mechanisms of harmonics generation is of fundamental and practical importance. Generation of low-order odd harmonics (third, fifth, seventh, etc.) in a perturbative regime of laser-matter interaction provides a possibility of direct measurements of nonlinear optical constants of the material, such as nonlinear optical susceptibilities and optical nonlinearities. Moreover, generation of low-order odd harmonics attracts a growing interest, since it might serve as an indicator, which enables to test the alleged role of higher-order Kerr effect and saturating nonlinearities in gaseous [36, 37] and in solid state media [38] in particular.

The objective of the thesis

The objective of this dissertation is to investigate filamentation scenarios of intense laser pulses in the range of zero to anomalous GVD of wide bandgap solid-state dielectric materials and characterize relevant nonlinear effects (i.e., plasma generation, pulse compression, generation of low order odd harmonics) that accompany filamentation and eventually lead to generation of ultrabroadband, multioctave supercontinuum.

The main tasks of the thesis

- Spatiotemporal characterization of filamentation dynamics in sapphire and fused silica in the regimes of weak, moderate and strong anomalous group velocity dispersion.
- Investigation of the role of external focusing geometry in the dynamics of spectral broadening and supercontinuum generation in sapphire at its zero group velocity dispersion point.
- Analysis of low order odd harmonics (third, fifth and seventh) generation during filamentation and supercontinuum generation of mid-infrared pulses in transparent solid-state dielectric medium (CaF_2).
- High dynamic range characterization of spectral evolution of mid-infrared laser pulse-induced spectral broadening and multioctave SC generation in wide bandgap dielectric media: fused silica, YAG and LiF.

Practical and scientific novelty

- Despite the differences in GVD coefficients and nonlinear refractive indexes of sapphire and fused silica, very similar spatiotemporal transformations of the input Gaussian wave-packet in both nonlinear materials were observed. It was demonstrated that in the regime of moderate and strong anomalous GVD, the intensity distributions converge into a characteristic ring-shaped spatiotemporal profile, which is a universal shape of the spatiotemporal light bullet in bulk Kerr medium. In the regime of weak anomalous GVD, pulse splitting is observed which is similar to that in the regime of normal GVD. However, the differences occur in the space-time domain, where the individual sub-pulses develop distinct O-shaped spatiotemporal distributions, which allow interpreting them as quasistationary spatiotemporal light bullets.

- It is demonstrated that focusing of the pump beam either on the input face or inside the nonlinear material results in remarkably different spectral evolutions versus the input pulse energy. In the configuration where the geometrical focus of the input beam is located inside the crystal, the energy threshold for SC generation is reduced by 25%; however, the SC spectral width experiences a dramatic variation on the input pulse energy. In particular, after the SC is generated, further increase of the input energy leads to an almost complete suppression and afterwards a recovery of the SC generation. It is assumed that these features of SC generation scenario are universal and should be considered for optimization of various SC generation schemes, where SC is produced by relatively long femtosecond pulses delivered by recently developed Yb:KGW, Yb:KYW, Yb:fiber, and similar laser systems.

- It was uncovered that the temporal structure of TH radiation consists of free and driven components, which are generated at the boundary of a vacuum and a nonlinear dielectric medium in the conditions of large phase and group-velocity mismatch. The free and driven TH pulses propagate with different group velocities, so the temporal separation between the pulses increases with propagation, producing an evolving interference pattern in the TH spectrum.

- Relevant characteristics of odd harmonics generation, such as the harmonics spectra, energy oscillations, and conversion efficiency, were measured as functions of propagation length and input-pulse energy and intensity. It is demonstrated that fifth and seventh harmonics are generated solely via cascaded four-wave mixing due to cubic nonlinearity of the material, and the contribution of higher order nonlinearities is negligible for input-pulse intensities up to 15 TW/cm^2.

- It is demonstrated that odd harmonics generation brings a relevant contribution to spectral superbroadening in a solid-state dielectric medium as the plasma-dominated filamentation regime is accessed. In particular, it was shown that the plasma-induced pulse compression results in spectral broadening around the carrier wavelength and facilitates large-scale spectral broadening of the third, fifth, and seventh harmonic spectra via cross-phase modulation, eventually yielding an SC spanning more than four octaves from the ultraviolet to the mid-infrared. The overlapping harmonics spectra produce a remarkable spectral broadening into the deep ultraviolet, which extends well beyond the blue-shifted cut-off of a typical SC spectrum set by the material GVD.

- The spectral dynamics versus the input pulse energy in wide bandgap solid state dielectric materials revealed different mechanisms of spectral broadening, which are characterized by the occurrence of specific well-distinguished spectral signatures and which are interpreted in terms of plasma-induced and anomalous group velocity dispersion-induced compression of the driving pulse. It is shown that, under given operating conditions (the input pulse width, the length of the nonlinear medium, and the focusing condition), there exists an optimum input pulse energy, which produces the broadest SC spectrum, allowing to optimize the practical setups for SC generation with mid-infrared laser pulses.

Statements to be defended

1. In the regime of anomalous GVD of solids, the self-focusing wave packet converges into a single light bullet with a universal O-shaped spatiotemporal intensity profile consisting of an extended ring-shaped periphery and a localized core that carries self-compressed, nearly transform-limited pulse.
2. External beam focusing geometry, i.e. location of the input beam waist either on the entrance face or inside the nonlinear medium, strongly affects the dynamics of spectral broadening.
3. Third-harmonic pulse, generated in a solid state medium in the conditions of large group and phase velocity mismatch, naturally consists of free and driven components that propagate with different group velocities.
4. Cascaded four-wave mixing via third-order nonlinearity is the dominant mechanism of fifth and seventh harmonics generation during filamentation of mid-infrared laser pulses in a solid state medium.
5. Generation odd harmonics and their subsequent spectral broadening substantially contribute to the generation of ultrabroadband, multioctave SC spectrum in a solid-state medium.
6. The interplay between self-phase modulation and anomalous GVD, leads to formation of the light bullets with multioctave supercontinuum spectra.

LIST OF PUBLICATIONS

On the dissertation topic

[A1] I. Gražulevičiūtė, **N. Garejev**, D. Majus, V. Jukna, G. Tamošauskas, A. Dubietis, Filamentation and light bullet formation dynamics in solid-state dielectric media with weak, moderate and strong anomalous group velocity dispersion, J. Opt. **18**, 025502 (2015).

[A2] V. Jukna, **N. Garejev**, G. Tamošauskas, A. Dubietis, Role of external focusing geometry in supercontinuum generation in bulk solid-state media, J. Opt. Soc. Am. B **36**, A54–A60 (2019).

[A3] A. Couairon, V. Jukna, J. Darginavičius, D. Majus, **N. Garejev**, I. Gražulevičiūtė, G. Valiulis, G. Tamošauskas, A. Dubietis, F. Silva, D. R. Austin, M. Hemmer, M. Baudisch, A. Thai, J. Biegert, D. Faccio, A. Jarnac, A. Houard, Y. Liu, A. Mysyrowicz, S. Grabielle, N. Forget, A. Durécu, M. Durand, K. Lim, E. McKee, M. Baudelet, M. Richardson, *Filamentation and Pulse Self-compression in the Anomalous Dispersion Region of Glasses*, in: Laser Filamentation Mathematical Methods and Models, eds. A. D. Bandrauk, E. Lorin, J. V. Moloney, (Springer, 2016) pp. 147–165.

[A4] **N. Garejev**, I. Gražulevičiūtė, D. Majus, G. Tamošauskas, V. Jukna, A. Couairon, A. Dubietis, Third- and fifth-harmonic generation in transparent solids with few-optical-cycle midinfrared pulses, Phys. Rev. A **89**, 033846 (2014).

[A5] **N. Garejev**, V. Jukna, G. Tamošauskas, M. Veličkė, R. Šuminas, A. Couairon, A. Dubietis, Odd harmonics-enhanced supercontinuum in bulk solid-state dielectric medium, Opt. Express **24**, 17060–17068 (2016).

[A6] **N. Garejev**, G. Tamošauskas, A. Dubietis, Comparative study of multioctave supercontinuum generation in fused silica, YAG, and LiF in the range of anomalous group velocity dispersion, J. Opt. Soc. Am. B **34**, 88–94 (2017).

Other publications

- [A7] J. Darginavičius, **N. Garejev**, A. Dubietis, Generation of carrier-envelope phase-stable two optical-cycle pulses at 2 µm from a noncollinear beta-barium borate optical parametric amplifier, Opt. Lett. **37**, 4805–4807 (2012).
- [A8] J. Darginavičius, D. Majus, V. Jukna, **N. Garejev**, G. Valiulis, A. Couairon, A. Dubietis, Ultrabroadband supercontinuum and third-harmonic generation in bulk solids with two optical-cycle carrier-envelope phase-stable pulses at 2 µm, Opt. Express **21**, 25210–25220 (2013).
- [A9] D. Majus, G. Tamošauskas, I. Gražulevičiūtė, **N. Garejev**, A. Lotti, A. Couairon, D. Faccio, A. Dubietis, Nature of Spatiotemporal Light Bullets in Bulk Kerr Media, Phys. Rev. Lett. **112**, 193901 (2014).
- [A10] A. Marcinkevičiūtė, **N. Garejev**, R. Šuminas, G. Tamošauskas, A. Dubietis, A compact, self-compression-based sub-3 optical cycle source in the 3–4 µm spectral range, J. Opt. **19**, 105505 (2017).
- [A11] A. Marcinkevičiūtė, V. Jukna, R. Šuminas, **N. Garejev**, G. Tamošauskas, A. Dubietis, Femtosecond filamentation and supercontinuum generation in bulk silicon, Opt. Lett. **44**, 1343–1346 (2019).
- [A12] A. Marcinkevičiūtė, V. Jukna, R. Šuminas, **N. Garejev**, G. Tamošauskas, A. Dubietis, Supercontinuum generation in the absence and in the presence of color centers in NaCl and KBr, Results Phys. **14**, 102396 (2019).
- [A13] M. Vengris, **N. Garejev**, G. Tamošauskas, A. Čepėnas, L. Rimkus, A. Varanavičius, V. Jukna, A. Dubietis, Supercontinuum generation by co-filamentation of two color femtosecond laser pulses, Sci. Rep. **9**, 9011 (2019).

Conference presentations

- [C1] **N. Garejev**, G. Tamošauskas, A. Dubietis, Keliu oktavų šviesos superkontinuumo generavimas žadinant skaidrius dielektrikus nulinės ir anomalios grupinių greičių dispersijos srityse, 42 Lietuvos nacionalinė fizikos konferencija, Vilnius, Lithuania, 2017.
- [C2] A. Marcinkevičiūtė, **N. Garejev**, R. Šuminas, G. Tamošauskas, A. Dubietis, Keleto optinių ciklų trukmės impulsų generacija ir spūda 3–4 µm spektrinėje srityje, 42 Lietuvos nacionalinė fizikos konferencija, Vilnius, Lithuania, 2017.

[C3] **N. Garejev**, G. Tamošauskas, A. Dubietis, Multioctave supercontinuum generation in bulk solid-state dielectrics in the range of near zero to anomalous group velocity dispersion, CLEO/Europe-EQEC, Munich, Germany, 2017.

[C4] **N. Garejev**, V. Jukna, G. Tamošauskas, M. Veličkė, R. Šuminas, A. Couairon, A. Dubietis, Multioctave, odd-harmonics-enhanced supercontinuum from plasma-dominated filamentation in solid state medium, Europhoton, Vienna, Austria, 2016.

[C5] **N. Garejev**, G. Tamošauskas, V. Jukna, A. Dubietis, Nelyginių harmonikų generacija kietojo kūno terpėje žadinant intensyviais infraraudonaisiais lazerio impulsais, 41-oji Lietuvos nacionalinė fizikos konferencija, Vilnius, Lithuania, 2015.

[C6] **N. Garejev**, I. Gražulevičiūtė, V. Jukna, D. Majus, G. Tamošauskas, G. Valiulis, A. Couairon, A. Dubietis, Generation of Third, Fifth and Seventh Harmonics in Bulk Solids with Intense Mid-Infrared Pulses, Naujametė Fizikos Konferencija LTϕ, Vilnius, Lithuania, 2015.

[C7] A. Dubietis, **N. Garejev**, V. Jukna, G. Tamošauskas, I. Gražulevičiūtė, D. Majus, G. Valiulis, A. Couairon, Nonlinear optical phenomena in bulk dielectric media with few optical cycle mid-IR pulses, Nonlinear Photonics, Barcelona, Spain, 2014.

[C8] A. Couairon, V. Jukna, J. Darginavicius, D. Majus, **N. Garejev**, I. Grazuleviciute, G. Valiulis, G. Tamosauskas, A. Dubietis, M. Durand, A. Jarnac, A. Houard, Y. Liu, A. Mysyrowicz, A. Lotti, D. Faccio, M. Hemmer, M. Baudisch, A. Thai, J. Biegert Near and mid-infrared pulse self-compression and light bullet formation by filamentation in transparent solids, 23rd annual International Laser Physics Workshop, Sofia, Bulgaria, 2014.

[C9] A. Couairon, V. Jukna, J. Darginavicius, D. Majus, **N. Garejev**, I. Grazuleviciute, G. Valiulis, G. Tamosauskas, A. Dubietis, D. Faccio, F. Silva, D.R. Austin, M. Hemmer, M. Baudisch, A. Thai, J. Biegert, Self-compression of near and mid-infrared pulses by filamentation in transparent solids, Photonics North, Montreal, Canada, 2014.

[C10] A. Couairon, V. Jukna, J. Darginavičius, D. Majus, **N. Garejev**, I. Gražulevičiūtė, G. Valiulis, G. Tamošauskas, A. Dubietis, F. Silva, D. R. Austin, M. Hemmer, M. Baudisch, A. Thai, J. Biegert, D. Faccio, A. Jarnac, A. Houard, Y. Liu, A. Mysyrowicz, S. Grabielle, N. Forget, A. Durecu, M. Durand, K. Lim, E. McKee, M. Baudelet, M. Richardson, Filamentation, third harmonic and supercontinuum generation, conical emission, in the anomalous dispersion region of transparent solids, Workshop on ”Mathematical Methods and Models in Laser Filamentation”, Montreal, Canada, 2014.

[C11] D. Majus, **N. Garejev**, I. Gražuleviciute, G. Tamošauskas, V. Jukna, A. Couairon, A. Dubietis, Third and fifth harmonic generation in transparent solids with few optical cycle mid-infrared pulses, Conference on Lasers and Electro-Optics, San Jose, USA, 2014.

[C12] **N. Garejev**, I. Gražulevičiūtė, V. Jukna, D. Majus, G. Tamošauskas, G. Valiulis, A. Couairon, A. Dubietis, Ultrafast nonlinear optics in bulk solids with intense few optical cycle mid-infrared pulses, ”Developments in Optics and Communications”, Riga, Latvia, 2014.

[C13] I. Gražulevičiūtė, G. Tamošauskas, **N. Garejev**, A. Lotti, D. Faccio, A. Dubietis, Three-dimensional light bullets from femtosecond filamentation in sapphire, ”Developments in Optics and Communications”, Riga, Latvia, 2014.

[C14] **N. Garejev**, I. Gražulevičiūtė, V. Jukna, D. Majus, G. Tamošauskas, G. Valiulis, A. Couairon, A. Dubietis, Superkontinumo, trečiosios ir penktosios harmonikų generavimas skaidriuose dielektrikuose žadinant dviejų optiniu ciklų trukmės impulsais, jaunųjų mokslininkų konferencija „Tarpdalykiniai tyrimai fiziniuose ir technologijos moksluose“, Vilnius, Lithuania, 2014.

[C15] A. Dubietis, J. Darginavičius, **N. Garejev**, I. Gražulevičiūtė, D. Majus, G. Valiulis, V. Jukna, A. Couairon, Nonlinear optics in the mid infrared, 2nd TLL-COLIMA-FOTONIKA Joint Workshop on manipulation of light by matter and matter by light, Vilnius, Lithuania, 2013.

[C16] **N. Garejev**, I. Gražulevičiūtė, V. Jukna, D. Majus, G. Tamošauskas, G. Valiulis, A. Couairon, A. Dubietis, Ultrabroadband supercontinuum, third and fifth harmonic generation in bulk solids with two optical-cycle pulses at 2 µm, XX-th Lithuania-Belarus seminar Lasers and Optical Nonlinearity, Vilnius, Lithuania, 2013.

[C17] Dubietis, J. Darginavičius, D. Majus, **N. Garejev**, V. Jukna, G. Valiulis, Superkontinuumo generacija plačios draustinės juostos dielektrikuose žadinant dviejų optinių ciklų trukmės infraraudonaisiais impulsais, 40-oji Lietuvos nacionalinė fizikos konferencija, Vilnius, Lithuania, 2013.

[C18] **N. Garejev**, J. Darginavičius, Generation of Odd Harmonics in Solid Media, Open Readings, Vilnius, Lithuania, 2013.

[C19] J. Darginavičius, D. Majus, V. Jukna, **N. Garejev**, T. Vasiliauskas, A. Dubietis, Ultrabroadband supercontinuum generation in bulk solids with few-opticalcycle CEP-stable pulses at 2 µm, Northern Optics, Snekkersten, Denmark, 2012.

[C20] **N. Garejev**, J. Darginavičius, Aukštųjų harmonikų generacija kietojo kūno terpėje, „Studentų mokslinė praktika 2012“, Vilnius, Lithuania, 2012.

[C21] **N. Garejev**, J. Darginavičius, Ultratrumpų šviesos impulsų generacija ir stiprinimas infraraudonojo spektro srityje, „Studentų moksliniai tyrimai 2011/2012“, Vilnius, Lithuania, 2012.

EXPERIMENTAL METHODS

This chapter describes the equipment and measurement methods used in experiments.

Laser light sources

- Ti:Sapphire laser system (Spitfire-PRO, Newport-Spectra Physics). Generates 800 nm, 130 fs pulses at up to 3 mJ energy at repetition rate up to 1 kHz. Used for pumping OPAs.
- Commercial noncollinear OPA (NOPA) (TOPAS-White, Light Conversion Ltd.). Generates 15–20 fs pulses, tunable in 530—720 nm spectral range with energy up to 30 µJ.
- Commercial OPA (TOPAS-Prime, Light Conversion Ltd.). Generates 100 fs pulses, tunable in 1100—2600 nm spectral range with energy up to 80 µJ.
- Commercial OPA (TOPAS-C, Light Conversion Ltd.). Generates 100 fs pulses, tunable in 1200—2400 nm spectral range with energy up to 50 µJ.
- Home built optical parametric amplifier [39]. Generates CEP-stable 20 fs pulses at 2 µm with energy up to 10 µJ.

Diagnostic equipment

- Home built high dynamic scanning prism spectrometer, covering 239–5857 nm wavelength range. Multiple detectors (Si, Ge, PbSe) are used to cover very broad spectral range. Used for spectral measurements shown in sections 1.2, 2.3, and chapter 3.
- Fiber spectrometer (QE65000, Ocean Optics), 16-bit dynamic range, covering 200–1000 nm wavelength range and capable of operating in single shot regime. Used for measuring harmonics spectra in fig. 2.3 and for measuring time evolution of SC spectra in fig. 3.3.
- Industrial monochromatic CCD camera (Grasshopper 2, Point Grey). Used in 3D mapping measurements in section 1.1.
- Consumer CMOS camera with Bayer color filter array (Nikon D7200, 3.92 µm pixel pitch). Used with 1.0x magnification lens for imaging luminance traces inside nonlinear material in section 1.2 and for photographing output beams in chapter 3.

Broadband high dynamic range spectral measurements

The energy (and intensity) of the input beam was varied using a neutral metal-coated gradient filter (NDL-25C-2, Thorlabs Inc.) on a motorized translation stage allowing automated measurements versus input energy.

The input beam is focused by lens placed on a translation stage, allowing to change the position of focus relative to the input face of the sample. The position of the output face of the sample is fixed and output radiation from it is imaged into the slit of the spectrometer using a pair of Al-coated parabolic concave mirrors. An aperture within the mirror system allows to select the acceptance angle up to ± 50 mrad from the beam propagation axis.

Si, Ge and PbSe detectors, operating in the 0.2–1.1 µm, 0.7–1.9 µm and 1.5–5.8 µm spectral ranges, respectively, are used to cover a broad spectral range. The measured spectra are corrected to sensitivity functions of the detectors and transmission of the internal components of the spectrometer. Finally, spectra from each detector are slightly scaled to achieve consistency in the overlap regions.

These methods were used for measurements in sections 1.2, 2.3, and chapter 3.

Harmonics generation measurements

In order to measure SC and harmonics generation dynamics versus propagation length a wedge-shaped CaF_2 sample was mounted on a motorized translation stage and was moved across the input beam, allowing precise scanning of propagation length in the 110 µm–2 mm range. Harmonic generation measurements in sections 2.1, 2.2 used CEP-stable 20 fs (three optical cycle), 1.98 µm input pulses from home built OPA [39]. Harmonic enhanced SC measurements in section 2.3 used 170 fs, 2.4 µm input pulses from OPA (TOPAS-Prime). The input beam was always focused at the input face of the crystal and its energy (and intensity) was varied using a neutral metal-coated gradient filter (NDL-25C-2, Thorlabs Inc.). Multiple different measurement setups were used to measure the properties of harmonics:

- Output radiation was collected directly into the slit of the fiber spectrometer (QE65000) using lens to measure the spectra.

- The harmonics energy measurements were performed by dispersing the harmonics beams in space using a fused silica prism with 60° apex angle. The harmonics energy was measured using automated 16-bit digitized detectors: the TH energy was measured using a silicon photodiode SFH 291 (Siemens) with a sensitivity of 0.66 pJ/count, the FH energy was measured using a silicon photodiode BPW 34 B (Osram) with a sensitivity of

1.6 fJ/count, while the SH energy was measured using a photomultiplier tube FEU-84 with a sensitivity of 40 aJ/count.

- The cross-correlation measurements were performed by means of broadband sum-frequency generation in 0.2 mm-thick beta barium borate crystal (cut for type I phase matching) by sampling the output pulses with 20 fs, 575 nm reference pulses from the NOPA (Topas-White). The cross-correlation signals of either the driving pulse at fundamental frequency or the TH pulse were discriminated by setting a proper phase matching angle of the sum-frequency-generating crystal and using a set of color glass filters.
- Broadband SC spectral measurements, described in section: Broadband high dynamic range spectral measurements.

These methods were used for the measurements in chapter 2.

Nonlinear 3D-mapping

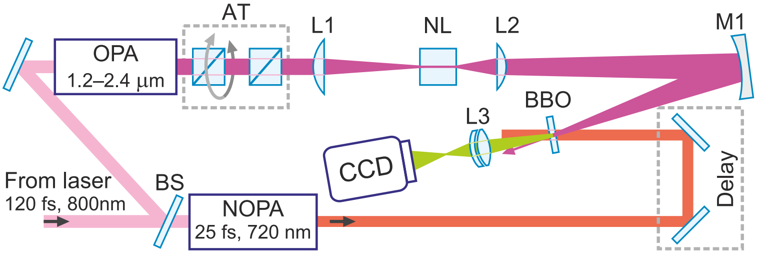

Figure 1: 3D mapping experimental setup. OPA, optical parametric amplifier; NOPA, noncollinear optical parametric amplifier; AT, variable attenuator for signal/idler pulse selection and energy control; BS, beamsplitter; NL, nonlinear medium; L1, L2, L3, lenses; M1, concave mirror; BBO, beta-barium borate crystal for broadband sum-frequency generation.

Fig. 1 shows the setup for generating filaments and analyzing their spatiotemporal structure. OPA (Topas-C) served as pump for filament generation. The OPA output was suitably attenuated by means of two Glan prisms, which served for isolation and variable attenuation of either signal or idler beams, which thereafter were spatially filtered (not shown) and focused by an $f = +100$ mm lens onto the front face of the nonlinear medium. The FWHM dimensions of the spot at the focal plane varied from 40 to 60 µm, depending on the input wavelength. The spatiotemporal intensity distribution of the emerging wave packet at the output of the nonlinear medium was measured by means of a three-dimensional imaging technique, based on recording the spatially-resolved cross-correlation function. For that purpose, the output wave-packet was imaged by a $4f$ system onto 20 µm thick beta-barium borate (BBO) crystal cut for type I phase matching, where it was gated with a short, 25 fs pulse with a central wavelength of 720 nm by means of sum-frequency generation. The short gating pulse was produced by a NOPA (Topas-White). The resulting cross-correlation signal was then imaged by a lens L3 onto the CCD camera. The entire spatio-temporal intensity (x, y, t) distribution of the resulting wave packet was reproduced by merging a series of cross-correlation images recorded by changing the time delay between the object and the gating pulses in an 8 fs step.

The self-focusing dynamics as a function of propagation distance z was captured by using a set of sapphire and fused silica samples of different lengths. In doing so, the samples of the nonlinear medium were placed in such a way that the output face was always kept at the same fixed position (as necessary for imaging), while the position of the focusing lens L1 was adjusted accordingly to ensure the location of the input focal plane on the front face of the sample.

This setup was used for the measurements in section 1.1.

1. ROLE OF GVD AND EXTERNAL FOCUSING GEOMETRY IN FEMTOSECOND FILAMENTATION

1.1. Spatiotemporal dynamics of optical filamentation in the range of anomalous GVD

Motivation

Filamentation of intense femtosecond laser pulses in transparent dielectric media is an universal phenomenon, observed in gases, solids and liquids [1]. The light filament emerges from a collective action of linear (diffraction and dispersion) and nonlinear (self-focusing, self-phase-modulation (SPM), four-wave mixing, multiphoton absorption, ionization and plasma defocusing) effects, whose dynamic interplay produces rich temporal, and more, generally, spatiotemporal dynamics, which in turn gives rise to spectral superbroadening, or supercontinuum generation.

In solid-state dielectric media, the group velocity dispersion (GVD) plays a decisive role in self-focusing and filamentation of ultrashort-pulsed laser beams [15, 40, 41]. In the regime of normal GVD, self-focusing is concurrent with pulse front steepening and formation of the optical shocks, and eventually, pulse splitting which occurs at the nonlinear focus [10, 42]. The pulse splitting results in the emergence of distinct leading and trailing sub-pulses, responsible for generation of the red-shifted and blue-shifted spectral components, respectively, which comprise the broadband supercontinuum spectrum [11]. The pulse splitting and supercontinuum generation processes are tightly connected and reemerge with every subsequent focusing cycle [43].

Although the physical effects governing filamentation in the anomalous GVD regime are basically the same, the reversal of GVD sign has a dramatic impact on the overall filamentation dynamics. In this case it is expected that the self-focusing wave packet should experience simultaneous compression in space and in time, as first suggested by an early work of Silberberg [44], who put forward the concept of spatiotemporal light bullets, which currently attract a considerable attention [45–47]. Indeed, filamentation phenomena in the regime of anomalous GVD were studied numerically [18, 48, 49] and more recently verified experimentally, leading to a discovery of a qualitatively new filamentation regime, which produces quasistationary three-dimensional light bullets that preserve a narrow beam diameter and a short pulsewidth over considerable propagation distance in a nonlinear dispersive medium [20, 21, 50]. Comprehensive characterization of the light bullets revealed that these objects are polychromatic Bessel-like beams [22] and exhibit peculiar propagation properties in free space, exceptional robustness against various perturbations [51] and maintain stable carrier-envelope phase [52].

This section is based on the research published in paper [**A1**] and presents a series of measurements, which characterize filamentation dynamics of intense ultrashort laser pulses in the space-time domain, as captured by means of three-dimensional imaging technique in sapphire and fused silica, in the wavelength range of 1.45–2.25 µm, accessing the regimes of weak, moderate and strong anomalous group velocity dispersion (GVD).

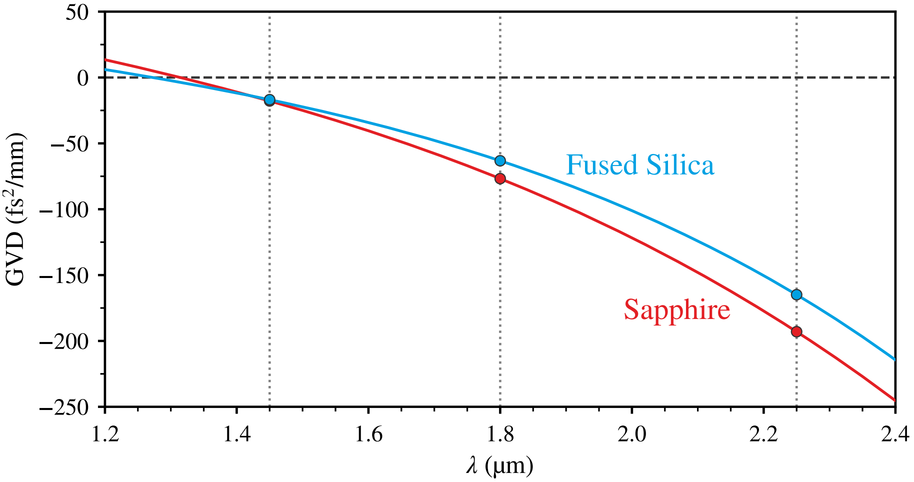

Figure 1.1: GVD of sapphire (red curve) and fused silica (blue curve) in the 1.2–2.4 µm wavelength range. Full circles denote the GVD values, under which the measurements were performed.

The self-focusing dynamics as a function of propagation distance z was captured by using a set of sapphire and fused silica samples of different lengths. In doing so, the samples of the nonlinear medium were placed in such a way that the output face was always kept at the same fixed position (as necessary for imaging), while the position of the focusing lens was adjusted accordingly to ensure the location of the input focal plane on the front face of the sample. The measurements were performed with three input pulse wavelengths: 1.45, 1.8 and 2.25 µm, which yield different GVD values, as depicted in fig. 1.1, accessing the regimes of weak (close to zero), moderate and strong anomalous GVD, respectively. The energy of the input pulse at the particular wavelength was set so as to exceed the critical power of self-focusing, P_{cr} , by 2.3–4.2 times. The critical power for self-focusing was estimated using an expression

$P_{cr} = 0.15\lambda^2/(n_0 n_2)$, where n_0 and n_2 are linear and nonlinear refractive indexes, respectively. The values of n_2 were taken as 2.9×10^{-16} cm^2/W and 2.3×10^{-16} cm^2/W for sapphire and fused silica, respectively, neglecting their wavelength dependence, which is assumed to be small in the infrared spectral range [53].

1.1.1. Weak anomalous GVD

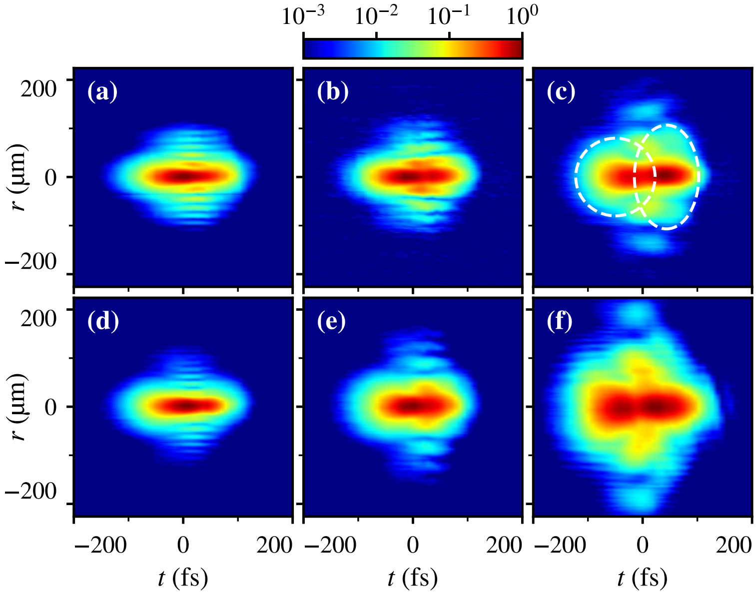

Figure 1.2: Spatiotemporal intensity profiles of the wave-packet with the center wavelength of 1.45 µm as recorded (top row) in sapphire at (a) $z = 4$ mm, (b) $z = 6$ mm, (c) $z = 15$ mm and (bottom row) in fused silica at (d) $z = 6$ mm, (e) $z = 10$ mm, (f) $z = 20$ mm.

The first series of measurements were carried out with the input pulse wavelength of 1.45 µm, which falls just slightly below the zero GVD wavelengths of fused silica (1.27 µm) and sapphire (1.31 µm), as shown in fig. 1.1, and represents the regime of weak anomalous GVD with equal GVD coefficients of -11 fs^2/mm. Here we launch the input Gaussian-shaped wave-packet with the FWHM beam diameter of $d_{in} = 40$ µm, pulsewidth of $\tau_{in} = 90$ fs and energy of 2.3 µJ, that equates to an input power of 4.1 P_{cr}. Fig. 1.2 shows the resulting spatiotemporal profiles measured in sapphire at various propagation distances z, which illustrate the spatiotemporal transformations at relevant stages of self-focusing. Here and in the following measurements the zero time point was set arbitrarily, at the center of the integrated envelope of the pulse.

The self-action of the input wave packet results in its shrinking in space and slight compression in time due to self-focusing and the interplay between SPM and anomalous GVD, respectively, that take place during the first few millimeters of propagation (not shown). Thereafter, the wave packet undergoes a dramatic transformation at the nonlinear focus, which is located approximately at $z = 4$ mm, as shown in fig. 1.2(a). Here the occurrence of the horizontal lobes in the (x, t) representation attests formation of a Bessel-like beam in the space domain, which develops due to combined action of self-focusing, multiphoton absorption and diffraction [2]. At the same time, the spatial transformation is followed by the pulse splitting in the time domain, producing distinct leading and trailing sub-pulses, which become clearly resolved at further propagation distances, $z = 6$ mm and $z = 15$ mm, as shown in fig. 1.2(b) and (c). More careful inspection of fig. 1.2(c) suggests that the individual sub-pulses acquire peculiar ring-shaped (or so-called, O-shaped) spatiotemporal intensity distributions, as overlaid by bold-dashed curves, which serve as guides for the eye. Notice the logarithmic intensity scale, which is used to highlight fine spatiotemporal features in the periphery of the resulting wave packet.

Fig. 1.2(d)–(f) show the spatiotemporal intensity distributions measured in fused silica with the input pulse energy (power) of 2.4 µJ (2.7 P_{cr}), which confirm a remarkably similar, pulse-splitting-based filamentation scenario: the occurrence of the Bessel-like spatial profile and pulse splitting at the nonlinear focus (fig. 1.2(d)), and finally, the development of characteristic O-shaped spatiotemporal intensity distributions of the individual split sub-pulses with further propagation, which overlap in the space–time domain due to proximity of the split pulses (fig. 1.2(e) and (f)).

Summarizing these observations, the temporal dynamics with prevailing pulse splitting on the propagation axis in the regime of weak anomalous GVD to some extent is similar to the temporal dynamics observed in the regime of normal GVD, see e.g. [10,42]. However, the differences occur in the space–time domain, where the individual sub-pulses develop distinct O-shaped spatiotemporal distributions, which allow to interpret them as quasistationary spatiotemporal light bullets, in contrast to the nonlinear X waves with characteristic X-shaped Spatiotemporal distributions, as reported in the regime of normal GVD [54].

1.1.2. Moderate anomalous GVD

The second series of experiments were performed with the input pulse wavelength of 1.8 µm which yields the GVD coefficients of -77 fs^2/mm in sapphire, and -63 fs^2/mm in fused silica, respectively, (see fig. 1.1) and is considered as a regime of moderate anomalous GVD.

Fig. 1.3(a)–(c) present the measured spatiotemporal intensity profiles at relevant propagation lengths in sapphire. Fig. 1.3(a) shows how the input Gaussian wave packet with FWHM beam diameter of $d_{in} = 45$ µm, pulsewidth of $\tau_{in} = 90$ fs and energy (power) of 3.1 µJ (3.6 P_{cr}) is reshaped at the nonlinear focus, where it transforms into a Bessel-like beam with a narrow and intense central core, which experiences simultaneous self-compression in time due to opposite action of SPM and the effect of anomalous GVD [20]. With further propagation, the reshaped wave packet smoothly develops a character-

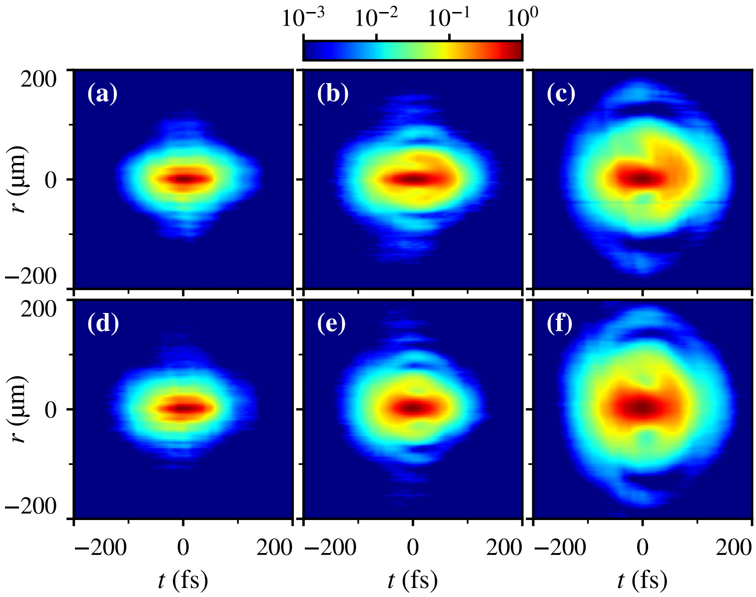

Figure 1.3: Spatiotemporal intensity profiles of the wave-packet with the center wavelength of 1.8 µm as recorded (top row) in sapphire at (a) $z = 4$ mm, (b) $z = 8$ mm, (c) $z = 15$ mm and (bottom row) in fused silica at (d) $z = 6$ mm, (e) $z = 10$ mm, (f) $z = 16$ mm.

istic ring-shaped spatiotemporal profile, as shown fig. 1.3(b) and (c), which represents the stationary solution of the nonlinear Schroedinger equation in nonlinear dissipative media in the anomalous GVD range [55] and which is a distinctive shape of the spatiotemporal light bullet in bulk Kerr medium [22]. The O-shaped spatiotemporal periphery sustains the sub-diffractive and sub-dispersive propagation of the central core, which carries the self-compressed pulse and ensures its robustness against perturbations, as verified by recent experiments reported elsewhere [22, 51, 52]. Fig. 1.3(d)–(f) present the results of measurements in fused silica with 3.3 µJ (2.3 P_{cr}) input pulses, which reveal a striking similarity of recorded spatiotemporal intensity profiles, confirming the validity of the above described transformation scenario.

1.1.3. Strong anomalous GVD

Strong anomalous GVD regime was accessed by setting the input pulse wavelength at 2.25 µm, which yields the GVD coefficients of −193 fs^2/mm in sapphire, and −165 fs^2/mm in fused silica, respectively, (see fig. 1.1).

Fig. 1.4 presents the spatiotemporal intensity profiles as measured at various propagation distances in sapphire, showing how the input Gaussian wavepacket with the FWHM beam diameter of $d_{in} = 61$ µm, pulsewidth of $\tau_{in} = 100$ fs and energy (power) of 6.3 µJ (4.2 P_{cr}) (fig. 1.4(a)) transforms into a

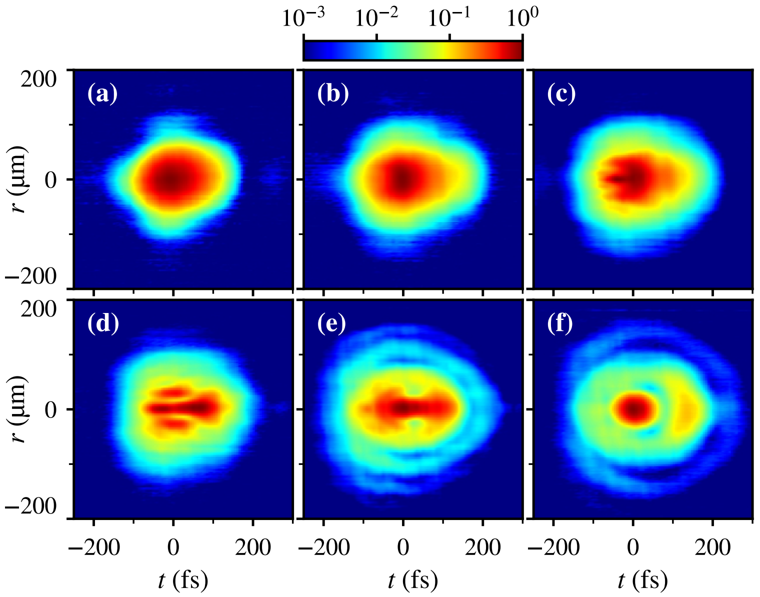

Figure 1.4: Spatiotemporal intensity profiles of the wave-packet with the center wavelength of 2.25 µm as measured at various propagation distance in sapphire at (a) $z = 0$ mm, (b) $z = 4$ mm, (c) $z = 6$ mm, (d) $z = 8$ mm, (e) $z = 12$ mm and (f) $z = 15$ mm.

spatially and temporally compressed three-dimensional light bullet. However, in present case, a peculiar transient spatiotemporal dynamics was observed. Fig. 1.4(b) shows the spatiotemporal intensity profile of the wave packet, as measured at $z = 4$ mm, which indicates a slight self-compression the pulse in time while approaching the nonlinear focus. At the nonlinear focus ($z = 6$ mm) and beyond, the wave packet experiences a dramatic spatiotemporal transformation: the redistribution of its energy in space (formation of a Bessel-like beam) and conditional pulse splitting in time, as shown in fig. 1.4(c) and (d). Eventually, the spatiotemporal transformation of the wave packet ends up with a formation of a characteristic O-shaped spatiotemporal profile at $z = 12$ mm (fig. 1.4(e)), indicating the emergence of a single self-compressed light bullet, which thereafter preserves the acquired spatiotemporal shape during the rest of its propagation, as shown in fig. 1.4(f).

Summary of the results

Experiments performed in weak, moderate and strong anomalous GVD result in similar dynamics of light bullet formation in sapphire and fused silica, despite some differences in their properties. Meanwhile, different regimes of anomalous GVD produced dramatic changes in the process of filamentation. In regime of weak anomalous GVD, pulse splitting into two ring-shaped pulses was observed with spectrally shifted carrier frequencies. However, regimes of moderate and strong anomalous GVD produce a single self-compressed spatiotemporal light bullet. Despite some differences in the initial dynamics, the final result is a characteristic spatiotemporal shape, comprised of a high intensity central core that carries nearly or almost bandwidth limited self-compressed pulse and a low-intensity ring-shaped periphery, which is an universal shape of the spatiotemporal (3D) light bullets in bulk Kerr media with anomalous GVD.

1.2. Effect of external focusing geometry on filamentation and supercontinuum generation dynamics

Motivation

A typical SC generation setup considers external focusing of the input beam in that way so as the beam waist is located on the front face of the nonlinear medium. However, other focusing geometries could be applied, although these have received much less attention so far. In that regard, several studies revealed that the SC spectral width, and the blue-shifted spectral broadening in particular, is very critical to the position of the nonlinear medium with respect to the geometric focus of an external focusing lens, as demonstrated with convergent and divergent pump beams in fused silica [41] and more recently, in water [56], in the ranges of normal and anomalous GVD, respectively. An unexpected spectral evolution versus the input pulse energy was recorded when focusing the input beam inside fused silica and YAG samples, demonstrating considerable shrinking of the entire SC spectrum while increasing the input pulse energy [57].

This section is based on the research published in paper [**A2**] and addresses the role of external focusing geometry in the dynamics of spectral broadening and supercontinuum generation in sapphire, as is produced by filamentation of 210 fs pulses with the central wavelength at 1.3 µm that matches the zero GVD point of the crystal.

1.2.1. Focusing onto the input face

Figure 1.5(a) presents the spectral evolution versus the input pulse energy in the case when the geometric focus of the input beam was located exactly at the input face of sapphire sample. An explosive spectral broadening is observed as the input pulse energy reaches a certain threshold value (2 µJ). Thereafter, as the pump energy increases, the SC spectral width remains fairly constant, extending from 470 nm to 1.8 µm (at the 10^{-5} intensity level). This case constitutes a typical dynamics of the spectral broadening, as observed in other nonlinear media and/or with other incident wavelengths, see e.g. [58, 59].

Fig. 1.5(b) illustrates the corresponding luminescence traces, as captured

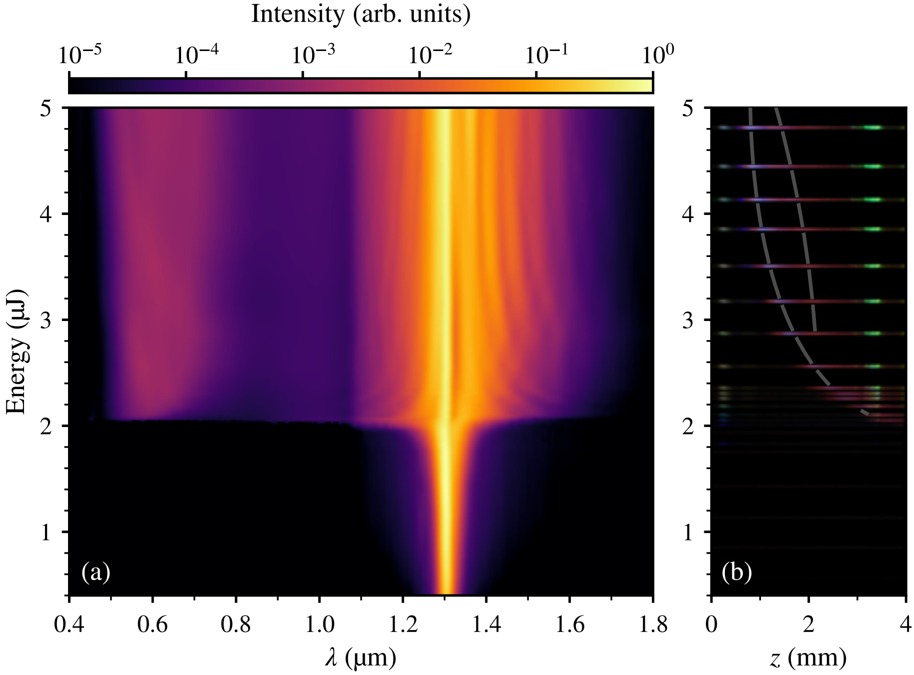

Figure 1.5: (a) Spectral evolution versus the input pulse energy as measured with 210 fs, 1.3 μm input pulses, focusing the beam onto the input face of 4 mm-long sapphire sample. (b) Composite image of the luminescence traces inside the crystal. Gray curves indicate the positions of the local luminescence maxima. z denotes the propagation distance, where $z = 0$ mm and $z = 4$ mm correspond to the input and output faces of the crystal, respectively.

from a side view of the crystal. Crystal luminescence readily serves for monitoring the filament formation dynamics in various solid state materials [60], while its spectral analysis provides information on the energy deposition to the crystal lattice, dopants and impurities [61]. In the present case, luminescence of sapphire originates from the 11 photon absorption, assuming its bandgap of 9.9 eV and photon energy of 0.95 eV. Sapphire produces a broad luminescence band which peaks at 325 nm, as verified by measuring the luminescence spectrum with a fiber spectrometer (not shown here), which is possibly attributed to the formation of F^+ centers, see e.g. [62]. Its long-wave tail extends into the visible range and is perceived by a naked eye (and the photo camera) as a distinct violet emission. The intense green spot is attributed to a parasitic reflection of the SC light that is produced by scattering at the output face of the crystal. The most intense part of the luminescence trace indicates the highest intensity and hence the position of the nonlinear focus: notice how the nonlinear focus shifts from the output face toward the input face of the crystal as the input pulse energy is increased. Interestingly, for the input pulse energies > 2.6 µJ, the luminescence trace shows a fainter but distinct secondary maximum. The gray curves in Fig. 1.5(b) highlight the positions of the main and secondary maxima of the luminescence trace, serving as guides for the eye.

1.2.2. Focusing inside the nonlinear material

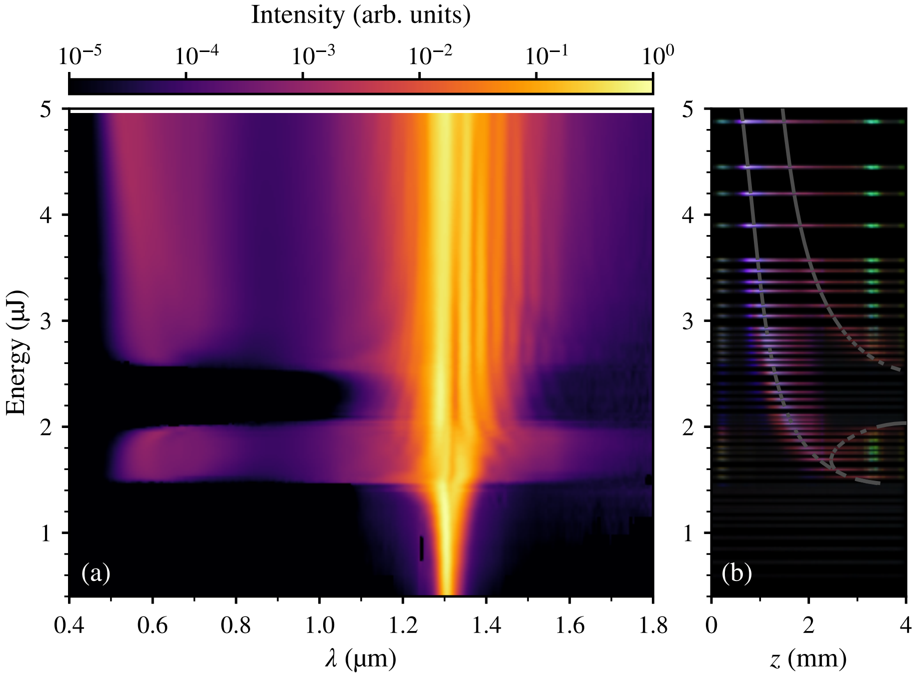

Figure 1.6: The same as in Fig. 1.5, but the input beam is focused 1 mm inside the sapphire sample.

A surprising spectral evolution, as shown in Fig. 1.6(a), was recorded in the second case, when the input beam was focused 1 mm inside the sapphire sample. First of all, the threshold energy for SC generation (1.48 µJ) was found to be lower by 25% as compared with the above case. However, with further increase of the input pulse energy, a complete suppression of SC generation is observed in the 2.0–2.5 µJ input energy interval. Thereafter, for the input pulse energies above 2.5 µJ, the SC generation is recovered and further behaves in a similar fashion as described in the case illustrated in Fig. 1.5(a). Notice an abrupt character of the switching from SC generation to its suppression and from the suppression to its recovery in terms of the input pulse energy. More detailed spectra associated with SC generation, suppression and recovery are presented in Fig. 1.7.

Interestingly, in the input pulse energy range where SC generation is suppressed, the nonlinear focus is still inside the crystal, as indicated by the posi-

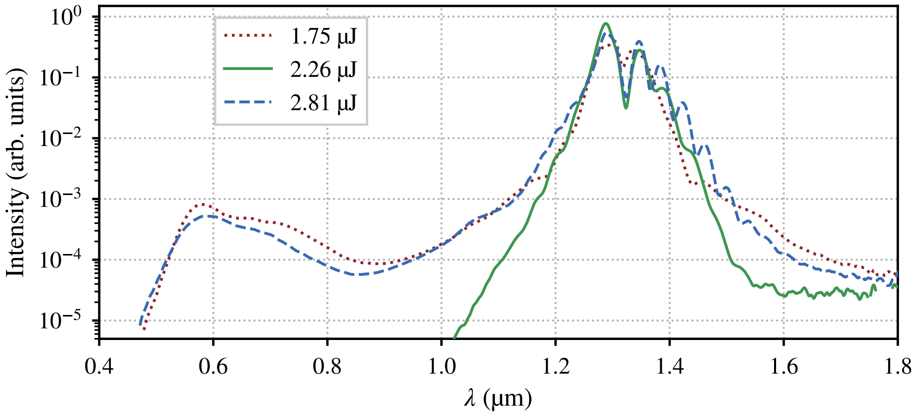

Figure 1.7: Comparison of the SC spectra generated with different input pulse energies in the case when the input beam was focused inside the sapphire sample.

tion of the main luminescence maximum, which continuously shifts toward the input face of the crystal with increasing the energy, as illustrated in Fig. 1.6(b). Notice that the absence of the SC is also apparently indicated by the absence of the parasitic green light due to scattering from the output face of the crystal. However, the trajectory of the secondary (fainter) luminescence maximum suggests a remarkably different dynamics versus the input pulse energy. First of all, just above the threshold energy for SC generation, the position of the secondary luminescence maximum continuously shifts toward the output face of the crystal, as the input pulse energy is increased, and eventually disappears. Thereafter, with further increase of the input pulse energy, the secondary maximum reappears at the output face and then moves toward the input face of the crystal. A comparison of Figs. 1.6(a) and 1.6(b) is very illustrative: the disappearance of the secondary maximum coincides with the suppression, while its reappearance coincides with the recovery of SC generation, suggesting rather unusual scenario of SC generation.

Summary of the results

Studies of SC generation in sapphire pumped by 210 fs, 1.3 µm pulses near its zero GVD point with varying focusing conditions have shown some interesting dynamics. We found that external focusing of the input beam either onto the input face or inside the crystal sample produces a surprisingly different dynamics of the spectral broadening. In the configuration where the geometrical focus of the input beam is located inside the crystal, the energy threshold for SC generation is reduced by 25%, however the SC spectral width experiences a dramatic variation on the input pulse energy. In particular, after the SC is generated, further increase of the input energy leads to an almost complete suppression and afterwards a recovery of the SC generation. That switching on and off the SC generation has an almost abrupt character in terms of the input pulse energy. The experimental observations were backed-up by the numerical simulations, which reproduced in detail the spectral evolutions in both cases of external focusing. Relatively long femtosecond pulses undergo strong reshaping of the wave packet due to defocusing and absorption of free electron plasma, subsequent replenishment of the pulse on the propagation axis and its splitting, which produces SC. It can be assumed that the uncovered SC generation scenario is universal and holds for filamentation of the pulses whose durations are in the range from few-100 fs to sub-picosecond and whose carrier wavelengths fall into the range of normal and zero GVD of the nonlinear medium.

2. GENERATION OF ODD HARMONICS VIA FEMTOSECOND FILAMENTATION

Motivation

Generation of low-order odd harmonics (third, fifth, seventh, etc.) in perturbative regime of laser-matter interaction provides a possibility of direct measurements of nonlinear optical constants of the material, such as nonlinear optical susceptibilities and optical nonlinearities. In the meantime, generation of low-order odd harmonics attracts a growing attention, since it might serve as an indicator, which enables to test the alleged role of high-order Kerr effect and saturating nonlinearities in gaseous [36, 37] and in solid state media [38] in particular.

Third harmonic generation is a frequently observed nonlinear optical effect, which accompanies filamentation of near-infrared laser pulses in air, with [63] and without [64] the onset of supercontinuum generation, see also [65] and references therein for more details. Using mid-infrared driving pulses, the wavelengths of low-order odd harmonics are shifted towards visible and near-infrared, into the transparency range of the nonlinear dielectric media, where they could be readily detected by simple means. To this end, generation of third, fifth [26–28] and seventh [29] harmonics by filamentation of mid-infrared laser pulses in air was recently experimentally observed. Generation of low-order odd harmonics was also reported under various experimental settings in semiconductors [30], and in liquid [31, 32] and solid state [33–35] dielectric media. More recently, filamentation of intense femtosecond laser pulses with central wavelength of 3.9 µm in air demonstrated a notable enhancement of the SC spectrum by odd-harmonics generation [66–68].

This chapter is based on the research published in papers **[A3, A4, A5]** and presents detailed experimental and numerical investigations of third- (TH), fifth- (FH) and seventh- (SH) harmonic generation in a CaF_2 sample of variable thickness, unveiling their contribution to spectral broadening and supercontinuum generation in the absence of optical damage of the nonlinear medium.

2.1. Third-harmonic generation

In isotropic dielectric media, TH generation is regarded as a simple nonlinear process mediated by the cubic (Kerr) nonlinearity. For efficient TH generation, phase matching condition $k(3\omega) = k(\omega) + k(\omega) + k(\omega)$ has to be fulfilled, where $k(\omega) = \omega n(\omega)/c$, ω is frequency and $n(\omega)$ is frequency-dependent refractive index. However, owing to high dispersion in the transparency range of condensed media, TH generation is never phase matched in a collinear propagation geometry, and wave vector mismatch, defined as $\Delta k = k(3\omega) - 3k(\omega)$, is always very large. This in turn imposes that the coherent buildup length, or simply, the coherence length, defined as $L_{\mathrm{coh}} = 2\pi/\Delta k$ is of the order of few tens of microns and the energy conversion efficiency typically does not exceed several tenths of percent. On the other hand, the group velocity mismatch between the driving and TH pulses, $\nu_{13} = 1/u_1 - 1/u_3$, where u_1 and u_3 are the respective group velocities, is very large as well and becomes an equally important factor that strongly affects the dynamics of TH generation.

More specifically, in $\mathrm{CaF_2}$ with 1.98 µm driving pulses the calculated $L_{\mathrm{coh}} = 78.5$ µm and $\nu_{13} = 32.4$ fs/mm. The latter converts to a walk-off length of $l_{13} = t_p/|\nu_{13}| = 620$ µm, as calculated for $t_p = 20$ fs input-pulse duration. The combination of large phase and group velocity mismatches defines rather specific condition for TH generation, which, in analogy with phase and group velocity-mismatched second harmonic generation [69–72], leads to the occurrence of a double-peaked TH pulse, consisting of so-called free and driven components. Free and driven TH pulses are generated at the boundary between the vacuum and nonlinear medium and represent solutions of the homogenous and the inhomogenous wave equations, respectively [71]. Free and driven TH pulses propagate with different group velocities: free TH pulse propagates with the group velocity u_3 set by the material dispersion, while driven TH pulse propagates with the group velocity u_1 of the fundamental frequency (driving) pulse, which induces the nonlinear polarization. With propagation, the temporal separation between free and driven pulses increases as $\tau = |\nu_{13}|z$, where z is the propagation length, producing evolving interference pattern in the TH spectrum, which was recently experimentally observed in fused silica, sapphire, YAG and $\mathrm{CaF_2}$ [34].

Figure 2.1 shows the cross-correlation functions of driving and TH pulses and respective TH spectra, as recorded at $z = 0.34$ mm and $z = 1.93$ mm of propagation. At a shorter propagation distance, $z = 0.34$ mm, free and driven TH pulses still overlap and are temporally indistinguishable [Fig. 2.1(a)], resulting in smooth and featureless TH spectrum, as shown in Fig. 2.1(c). After $z = 1.93$ mm of propagation, free and driven pulses are separated due to the group velocity mismatch [Fig. 2.1(b)]. Note that the driven TH pulse stays under the envelope of the fundamental frequency (driving) pulse, while free TH pulse is clearly delayed; the measured temporal separation between their peaks is 59 fs, which is fairly close to calculated value of 63 fs. A double-peaked structure of the TH pulse results in distinct interference pattern as seen in TH spectrum [Fig. 2.1(d)].

When measuring THG with different pump energies a clear pattern of changing oscillation period emerges that can be seen in Fig. 2.2. Here the input-pulse energy was varied in the 0.5–3.5 µJ range, so as to avoid the onset supercontinuum generation.

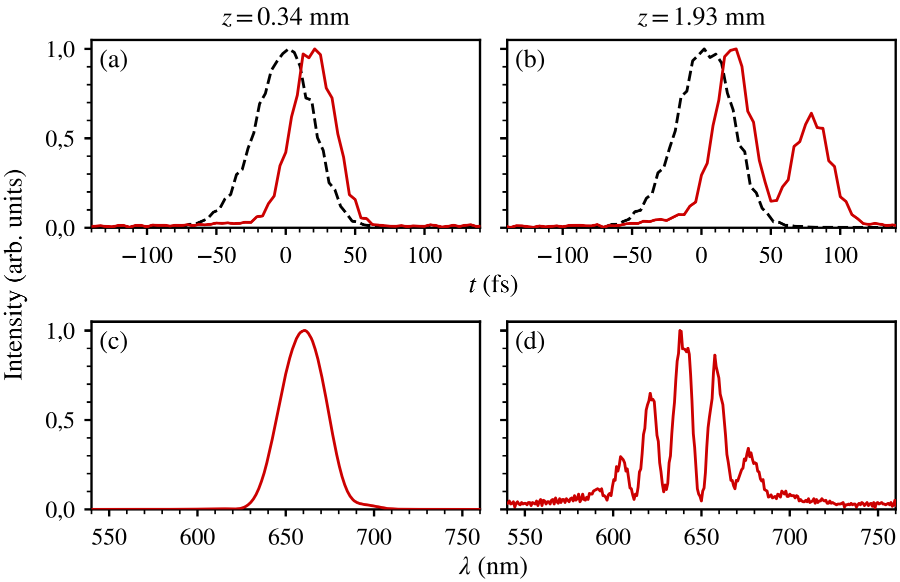

Figure 2.1: (a,b) Cross-correlation functions of the fundamental frequency (dashed curves) and TH (solid curves) pulses, as measured with 20 fs sampling pulses, and (c,d) TH spectra, measured at (a,c) $z = 0.34$ mm and (b,d) $z = 1.93$ mm of propagation in CaF_2. The input-pulse energy is 1.6 µJ. Fundamental and TH pulse intensities are not to scale.

The observed shortening of coherent buildup length could be explained in simple terms, accounting for correction of interacting wave vectors due to self- and cross-phase modulation (intensity dependent refractive index) effects:

$$\begin{aligned} k(\omega) &= \frac{\omega}{c}(n(\omega) + n_2 I), \\ k(3\omega) &= \frac{3\omega}{c}(n(3\omega) + 2n_2 I), \end{aligned} \tag{2.1}$$

where I is the input-pulse intensity and $n_2 = 1.9 \times 10^{-16}$ cm^2/W [73] is the nonlinear refractive index of CaF_2. According to Eq. (2.1), an increase of the input-pulse intensity results in unequal lengthening of interacting wave vectors, and thus in shortening of the coherence length. The calculated intensity dependence of the coherence length is in fair agreement with experimental results, as seen in Fig. 2.2.

2.2. Fifth-harmonic generation

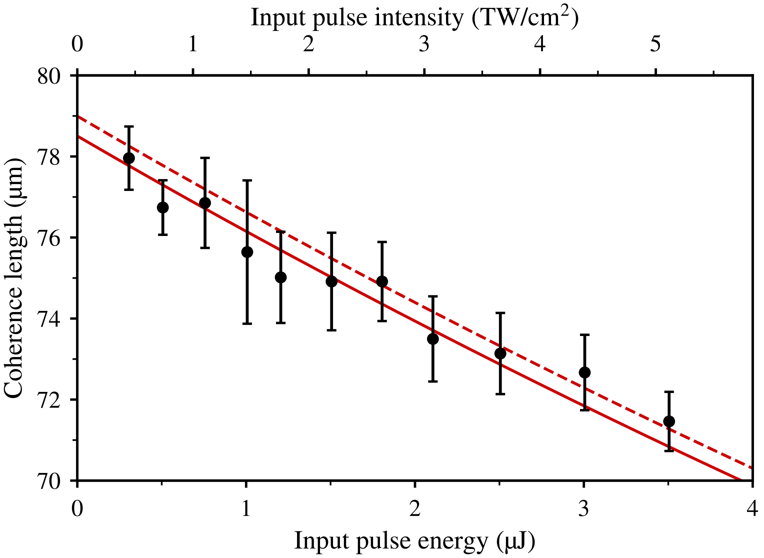

Figure 2.2: Coherent buildup length as a function of the input pulse energy and intensity. Full circles show the experimental data. Solid and dashed curves show the calculated coherent buildup length for 1.98 µm and 2.00 µm driving pulses, respectively.

Alongside TH generation fifth harmonic (FH) signal has been clearly detected at around 390 nm. Figure 2.3(a) shows TH and FH spectra, as measured with the input-pulse energy of 5 µJ at $z = 190$ µm. Respective far-field intensity profiles of FH and TH beams, as recorded with a CCD camera placed at 15 cm distance from the output face of CaF_2 sample, are shown in Figs. 2.3(b) and (c), demonstrating that FH and TH beams are generated on the propagation axis and have Gaussian intensity distribution, in contrast to cone-shaped harmonic beams observed in high numerical aperture focusing conditions [35].

Three possible scenarios of FH generation can be considered. The first is based on direct FH generation (six-wave mixing) via quintic nonlinearity $\chi^{(5)}$: $\omega+\omega+\omega+\omega+\omega = 5\omega$, with phase mismatch $\Delta k = k(5\omega)-5k(\omega)$ and estimated coherent buildup length of $L_{\text{coh}} = 21.8$ µm. The two remaining scenarios are based on four-wave mixing between fundamental frequency and its TH via cubic nonlinearity and represent two different cascaded processes [74]. The first cascaded process could be viewed as four-wave sum-frequency generation $3\omega + \omega + \omega = 5\omega$ with phase mismatch $\Delta k = k(5\omega) - k(3\omega) - 2k(\omega)$, which yields coherent buildup length of 30.2 µm. The second cascaded process could be regarded as four-wave difference-frequency generation $3\omega+3\omega-\omega = 5\omega$ with corresponding phase mismatch $\Delta k = k(5\omega)-2k(3\omega)+k(\omega)$ and $L_{\text{coh}} = 49.1$ µm.

In order to find out which processes are at play in the present case, simultaneous spectral measurements of TH and FH radiation versus propagation

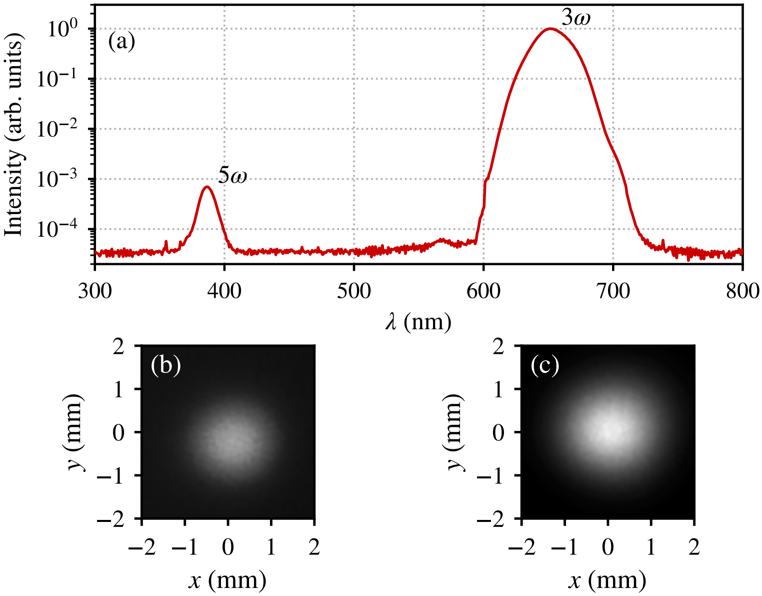

Figure 2.3: (a) TH and FH spectra as measured after $z = 190$ µm of propagation in CaF$_2$ with the input-pulse energy of 5 µJ. (b) and (c) show the far-field profiles of FH and TH beams, respectively.

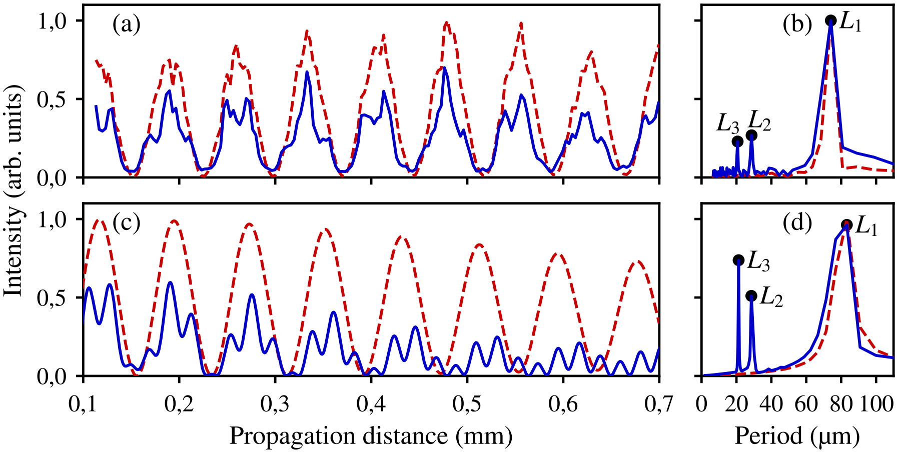

Figure 2.4: Oscillations of TH (red dashed curves) and FH (blue solid curves) spectral intensity versus the propagation distance: (a) experiment, (c) numerical simulations. TH and FH intensities are not to scale. (b) and (d) show the respective Fourier spectra of TH (red dashed curves) and FH (blue solid curves) oscillations. Black dots indicate the oscillation periods of FH.

distance were performed. Figures 2.4(a) and (c) represent detailed comparison of TH and FH spectral intensity oscillations at 650 nm and 380 nm selected from the spectral measurements. The Fourier spectra of measured and numerically simulated TH and FH oscillations are presented in Figs. 2.4(b) and (d), respectively, and show that FH intensity oscillates at three different frequencies, corresponding to oscillation periods of ~ 74 µm, ~ 28 µm and ~ 20 µm, with good agreement between experimental and numerical data. The longest (74 µm) oscillation period, L_1, coincides with the oscillation period of TH intensity (its coherence length), and the 28 µm period, L_2, corresponds to the coherence length of FH generation via cascaded four-wave mixing process $\omega + \omega + 3\omega = 5\omega$; therefore these two periods are the signatures of cascaded nature of FH generation. Note that no oscillation is detected with the period of 49 µm, which is associated with the coherence length of FH generation via cascaded process $3\omega + 3\omega - \omega = 5\omega$, whose contribution to the nonlinear polarization oscillating at FH frequency is expected to be very small. Indeed, the nonlinear polarization, oscillating at FH frequency in this case is proportional to $\chi^{(3)} E_{\mathrm{TH}}^2 E^*$, where E denotes the complex amplitude of the electric field, and is much smaller than that produced by the first cascaded process, which yields the nonlinear polarization proportional to $\chi^{(3)} E^2 E_{\mathrm{TH}}$.

Finally, in order to verify that FH generation maintains its cascaded nature over a wide input-pulse energy and intensity range, measurements and numerical simulations of harmonics energy as a function of the input-pulse energy and intensity at a fixed propagation length were carried out, as shown in Fig. 2.5. The measurements were performed over a wide input-pulse energy (intensity) range by setting the propagation length $z = 120$ µm in the nonlinear medium, which coincides with the first experimentally accessible energy conversion maximum, and whose shift due to intensity-dependent phase matching condition is very small and where propagation effects of the beam (self-focusing and filamentation) are negligible.

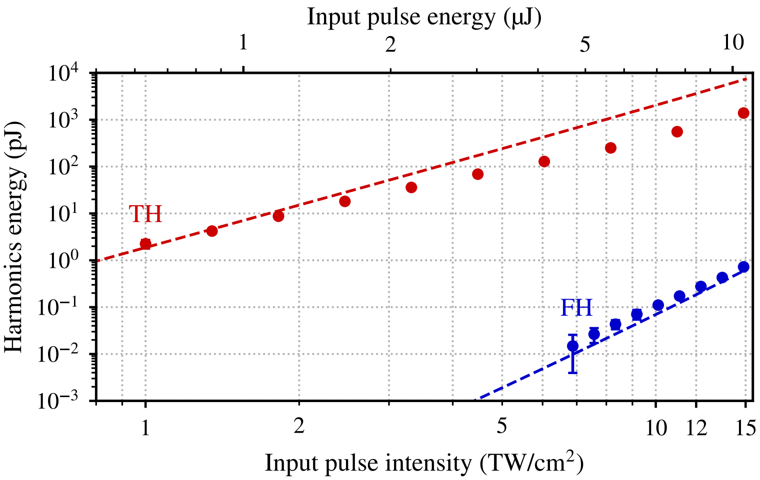

Figure 2.5: Measured (full circles) and numerically simulated (dashed lines) TH and FH energy as a function of the input-pulse energy and intensity.

The measured TH energy trend coincides with that obtained from the numerical simulations within the range of low input-pulse energies, however, at high input-pulse energies the measured TH energy values are consistently lower. On the other hand, there is almost perfect agreement between the experimental and numerical data on FH conversion. The obtained discrepancy is not essential in terms of evaluation of TH/FH conversion ratio, which might serve as an indicator of the role of higher order Kerr nonlinearities [36].

2.3. Harmonics enhanced supercontinuum

Under typical experimental settings (loose focusing condition) for filamentation in solid-state dielectric media, which refer to Kerr-dominated filamentation regime, the harmonics spectra are overlaid by much more intense supercontinuum emission, and harmonics generation is regarded as an interesting, but generally irrelevant phenomenon. However, recent theoretical and numerical studies suggest that odd harmonics generation may produce a non-negligible impact on the filament propagation dynamics and contribute to spectral broadening [75–78].

First of all, under these operating conditions, third (TH), fifth (FH) and seventh (SH) harmonics with center wavelengths of 800 nm, 480 nm and 343 nm, respectively, were experimentally detected and successive dynamics of their energy versus the propagation length z are shown in Figs. 2.6(a)–(c). Each data point in the plots represents an average of 40 laser shots, exposed to the same area of the crystal. The solid white curves mark the range of experimental parameter values (the input pulse intensity and propagation length) above which the optical damage on the output face of the crystal develops after that number of shots, as verified by monitoring an abrupt decrease of harmonics energies due to light scattering from a damage spot.

Figures 2.6(d)–(f) show the results of the numerical simulations, which reproduce the experimental data in great detail. The evolutions of TH, FH and SH energies versus the propagation distance z show a typical oscillatory behavior, as expected from strongly phase mismatched interactions. Indeed, the measured period of TH energy oscillations (85 µm) in the low intensity limit (with the input pulse intensity below 1 TW/cm^2) well coincides with the calculated double coherent build-up length $2L_{\mathrm{coh}} = 2\pi/|\Delta k| = 91$ µm, where $\Delta k = k(3\omega) - 3k(\omega) = 69.2\ \mathrm{mm}^{-1}$ is the phase mismatch for TH generation in CaF$_2$ with 2.4 µm input pulses. Interestingly, FH and SH energies oscillate with the same period as the TH energy, suggesting that FH and SH are generated by cascaded four-wave mixing processes based on the lowest, i.e. cubic nonlinearity [74]. Indeed, an extensive analysis of the FH oscillation periods performed in an earlier work [79] demonstrated that FH is generated via four-wave mixing between the TH and fundamental harmonics: $5\omega = 3\omega + \omega + \omega$.

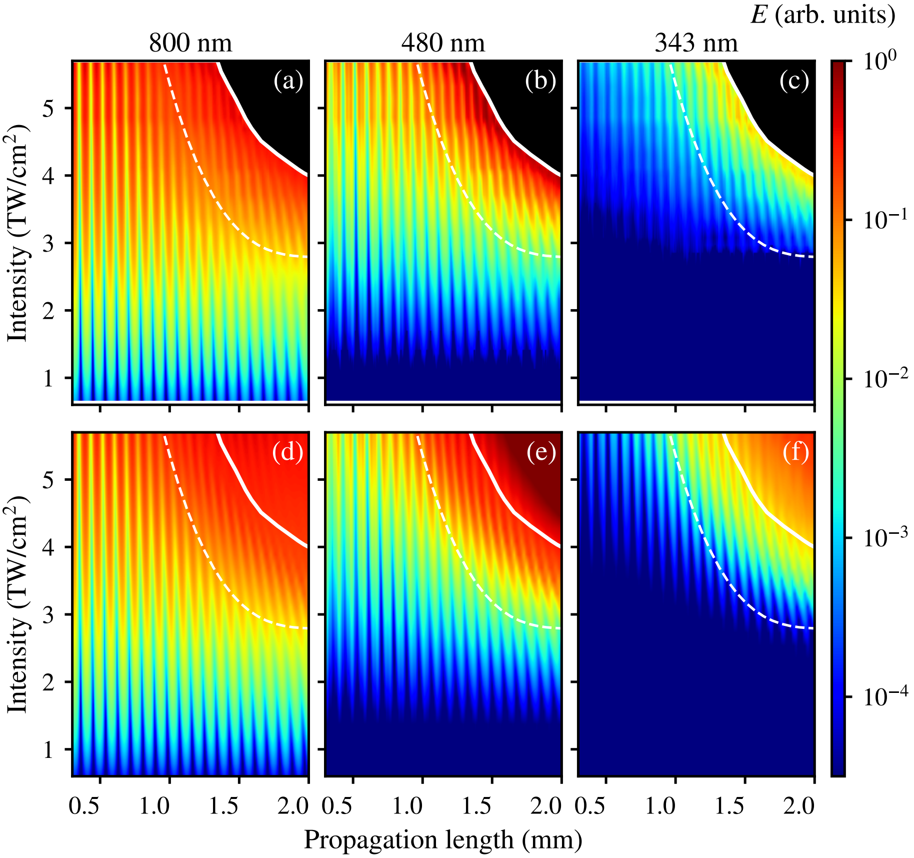

Figure 2.6: Experimentally measured (top row) and numerically simulated (bottom row) energies of (a,d) TH, (b,e) FH and (c,f) SH as functions of the driving pulse energy (intensity) and propagation length z. Dashed curves mark a virtual borderline between the Kerr-dominated and plasma-dominated filamentation regimes (see text for details). The black areas in the experimental graphs denote the region of the optical damage that occurs on the output face of the crystal, whose threshold is depicted by a solid curve.

Similar consideration applies to the seventh harmonic generation; there are two possible four-wave mixing configurations, which involve either mixing between the fundamental and TH ($7\omega = 3\omega + 3\omega + \omega$) or mixing between the fundamental and FH frequencies ($7\omega = 5\omega + \omega + \omega$). However, the relative contributions of these two processes could not be unambiguously revealed in this study.

More careful inspection of Fig. 2.6 reveals further interesting features of harmonics generation process. Firstly, TH, FH and SH energy oscillation periods are not constant; they slightly shrink with increasing the input pulse intensity, as evident from slightly tilted harmonics energy oscillation patterns with respect to the vertical axes. The reduction of the oscillation periods is attributed to self- and cross-phase modulation effects [79], which contribute to the changes in the wavevector length of the interacting waves and so the net reduction of the coherent build-up length.

Secondly, there occurs an abrupt change of the tilt angle of harmonics energy oscillation patterns, which coincides with a notable increase of the harmonics (FH and SH, in particular) energies. With increasing the input pulse intensity, a virtual borderline that marks the change of the character of harmonics energy oscillations, shifts closer to the input face of the crystal as highlighted by dashed curves in Fig. 2.6, which serve as guides for the eye.

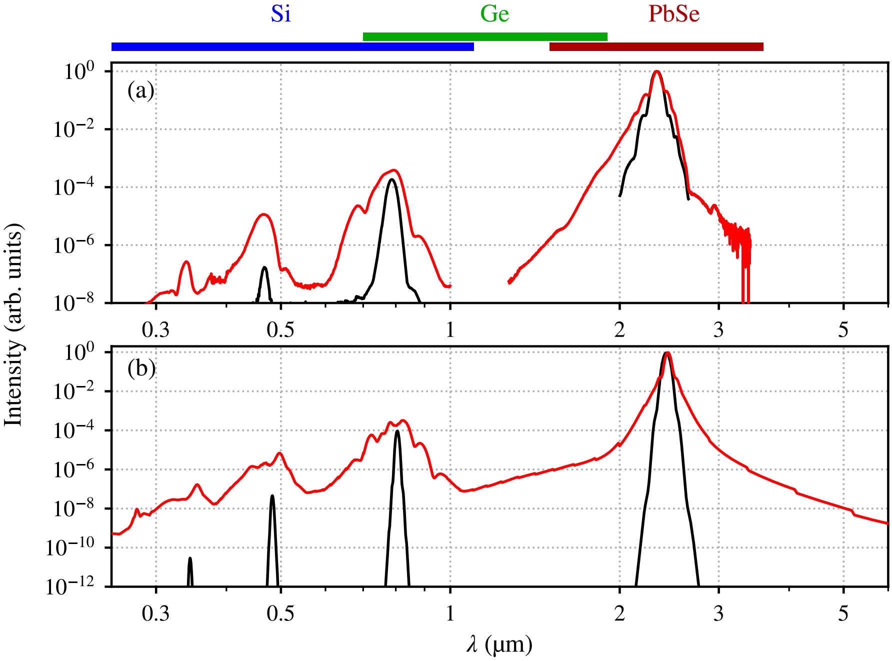

Figure 2.7: The output spectra which correspond to Kerr-dominated (black curves) and plasma-dominated (red curves) filamentation regimes: (a) experimental data; here the horizontal bars on the top indicate the spectral regions of the detectors, (b) numerical simulation.

Figure 2.7 presents the experimentally measured and numerically computed spectra highlighting the relevant spectral features associated with Kerr-dominated and plasma-dominated filamentation regimes, which were accessed for lower input pulse intensity and shorter propagation length (3.4 TW/cm^2, z = 0.48 mm) and for higher intensity and longer propagation length (4.1 TW/cm^2, $z = 1.94$ mm), respectively.

In the Kerr-dominated filamentation regime, the output spectrum consists of a series of isolated narrow-band spectral peaks corresponding to the driving pulse and its odd harmonics. In the plasma-dominated filamentation regime, the individual spectral peaks show considerable broadenings, which overlap and merge into an ultrabroadband, multi-octave supercontinuum radiation, which covers the wavelength range from 250 nm in the ultraviolet to more than 7 µm in the mid-infrared (at the 10^{-12} intensity level), approaching the infrared absorption edge of CaF_2 crystal. Note that even a broad spectral peak around the ninth harmonics at 267 nm appears in the numerical simulation, as shown in Fig. 2.7(b); however its energy was beyond the experimental detection range. A good agreement between the experimentally measured and numerically computed spectra is achieved although the experimental spectra were recorded within a reduced dynamic (10^{-8}) and wavelength (from 200 nm to 3.6 µm) ranges, as due to sensitivity limitations of our detection apparatus.

Summary of the results

Temporal and spectral measurements of odd harmonics generation in CaF_2 crystal pumped by three-optical-cycle 2 µm pulses have allowed to characterize the mechanisms of their generation. Relevant characteristics of harmonics generation process, such as harmonics spectra, energy oscillations and conversion efficiency were measured as a function of propagation length and input-pulse energy and intensity. Cross correlation measurements directly retrieved a double-peaked temporal structure of TH radiation, consisting of free and driven components. The free and driven TH propagate with different group velocities; the temporal separation between the pulses increases with propagation and produces an evolving interference pattern in TH spectrum.

Detailed measurements of TH and FH propagation in CaF_2 have shown similar oscillations. The detailed analysis of those oscillations, as well as an agreement with numerical simulation has shown that cascaded four-wave mixing is a dominant mechanism of FH generation with no apparent contribution from fifth-order nonlinearity.

The experimental and numerical investigation of odd harmonics and SC generation in CaF_2 crystal within a range of different input pulse intensities and propagation lengths allowed detailed characterization of the nonlinear processes involved. The results show that the main mechanism of higher harmonic generation is cascaded four-wave mixing. There is a clear difference between Kerr-dominated and plasma-dominated filamentation regimes being dominant at low and high intensities respectively. Plasma-induced compression of the driving pulse, which induces spectral superbroadening around the carrier wavelength as well as harmonics via XPM. In the end that results in broadband harmonics enhanced SC spectra spanning over 4 octaves.

3. MULTIOCTAVE SUPERCONTINUUM GENERATION IN WIDE BANDGAP DIELECTRICS

Motivation

Advances in the near and mid-infrared ultrashort-pulse laser sources, which are exclusively based on optical parametric frequency conversion, provided an access to experimentally investigate femtosecond filamentation and supercontinuum generation phenomena in the range of anomalous GVD of wide bandgap dielectric media. The first experiments performed in this spectral range demonstrated notable extension of the SC spectra in fused silica [16, 80]. These early findings facilitated the discovery of a qualitatively new filamentation regime, where simultaneous compression in space and time leads to formation of quasistationary self-compressed objects – spatiotemporal light bullets [19–22, 49]. Such filamentation conditions yielded multi-octave SC spectra with unprecedented wavelength coverage, as generated in wide bandgap dielectric crystalline materials, such as YAG, sapphire, CaF_2 and BaF_2 [33, 34, 81–84], in water [85], in various types of glasses: fused silica [50, 52, 86, 87], BK7 [88], fluoride (ZBLAN) [89], tellurite [90, 91] and chalcogenide glass [92], as well as in birefringent nonlinear crystals, such as DAST [93] and beta-barium borate (BBO) [94]. The numerical simulations suggest that even broader SC spectra could be obtained in sodium chloride and potassium iodide crystals [95]. By tuning the wavelength of the input pulses deeply into the mid-infrared, the ultrabroadband mid-infrared SC was generated by accessing the zero and anomalous GVD range of semiconductor media, such as GaAs [96, 97] and ZnSe [67, 98].

This chapter is based on the research published in paper [**A6**] and investigates the dynamics of mid-infrared laser pulse-induced spectral broadening and multioctave SC generation in fused silica, yttrium aluminium garnet (YAG), and lithium fluoride (LiF), whose relevant linear and nonlinear optical parameters are listed in Table 3.1. Thin samples (3 mm thickness) of these materials were used in the experiment. The wavelength of the pump pulse (2.3 µm) was chosen so as to fall into the range of anomalous GVD of all three investigated materials.

	E_g eV	T µm	n_0	λ_0 µm	g fs^2/mm	$n_2 \times 10^{-16}$ cm^2/W	P_{cr} MW
SiO$_2$	9.0	0.16 – 4.0	1.43	1.27	−180	2.3	24.1
YAG	6.5	0.21 – 5.2	1.80	1.61	−123	7.0	6.3
LiF	13.6	0.12 – 6.6	1.38	1.24	−98	1.05	54.8

Table 3.1: Linear and nonlinear parameters of UV-grade fused silica, YAG and LiF. n_0 and g are the linear refractive index the GVD coefficient at $\lambda = 2.3$ µm, respectively, E_g is the bandgap energy, λ_0 is the wavelength of zero GVD. T is the transmission range defined at 10% transmission level in 1 mm thick sample [99]. n_2 is the nonlinear refractive index taken from [20], [34] and [73], respectively, and P_{cr} is the estimated critical power for self-focusing.

3.1. Fused silica

Fused silica is a versatile material used for a variety of applications in linear and nonlinear optics, so there is no wonder that to date, a large fraction of the SC generation experiments in the range of anomalous GVD were performed in that nonlinear medium [16, 34, 50, 52, 80, 86, 87, 100, 101].

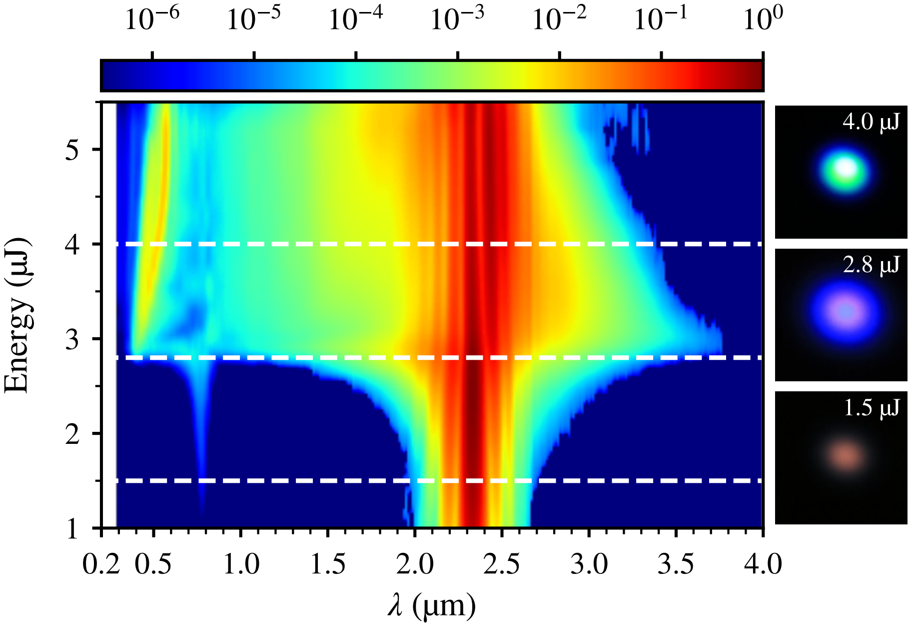

Figure 3.1: Spectral broadening in fused silica versus the input pulse energy. The insets on the right show the visual appearance of the output beam at various stages of spectral broadening.

Fig. 3.1 presents the spectral dynamics versus the input pulse energy, which captures two distinct phases of the spectral broadening, which are characterized by the occurrence of specific spectral features and which are attributed to different mechanisms of pulse compression.

In the input pulse energy range of 1.1–1.9 µJ (the power below P_{cr}), we observe a weak third harmonic (TH) peak centered at 767 nm. The TH generation is a simplest third-order nonlinear process, however, due to large phase mismatch, the TH peak is relatively weak [34,52] and hence is often overlooked in the SC generation experiments, where the dynamic range of the detection apparatus is typically limited to three-four orders of magnitude. Thereafter, in the input pulse energy range of 2.0–2.7 µJ (0.8–1.1 P_{cr}), an almost symmetric spectral broadening around the carrier wavelength along with dominant blue-shifted spectral broadening of the TH peak is observed. The TH spectrum extends into the visible spectral range and becomes detectable by the naked eye, appearing as a faint red spot, as shown in the inset of Fig. 3.1. At this stage the spectral broadening around the carrier wavelength could be attributed to plasma-induced compression of the driving pulse, where plasma generation results in a catastrophic blow-up of the trailing part of the pulse, in analogy with recent observations in $\mathrm{CaF_2}$ [102]. The blue-shifted spectral broadening of the TH peak could be explained by the differences of the group velocities of the driving and TH pulses: since the driving pulse travels with the largest group velocity, the slower TH pulse shifts toward its trailing front, as a result experiencing large spectral blue shift via cross-phase modulation. Along with spectrally broadened TH, we also capture an occurrence of a very weak spectral peak at 425 nm, which is almost unresolved in Fig. 3.1. That spectral peak corresponds to fifth harmonic, which is generated by the cascaded four wave mixing between the fundamental and TH frequencies [79,102].

An explosive spectral broadening is observed with the input pulse energy of 2.8 µJ (corresponding to 1.2 P_{cr}), which yields an ultrabroadband SC extending from the ultraviolet (310 nm, at the 10^{-6} intensity level) to the mid-infrared (3.75 µm at the 10^{-5} intensity level). The SC spectrum features the characteristic intense blue-shifted peak, which is centered at 430 nm, while the TH peak becomes quickly masked by much more intense SC emission. Such a broad spectrum is produced by formation of the light bullet, which emerges from simultanoeus compression in space due to self-focusing and in time due to opposite effects of self-phase modulation and anomalous GVD [19–22, 49], which is further referred as the regime of GVD-induced pulse compression.

3.2. YAG

YAG is an attractive nonlinear material because of its high nonlinearity, wide transparency range and high optical damage threshold. In particular, owing to high nonlinear refractive index, the SC is generated at reasonably low input pulse energies, as reported with mid-infrared laser pulses with carrier wavelengths of 2 µm [34] and 3 µm [33].

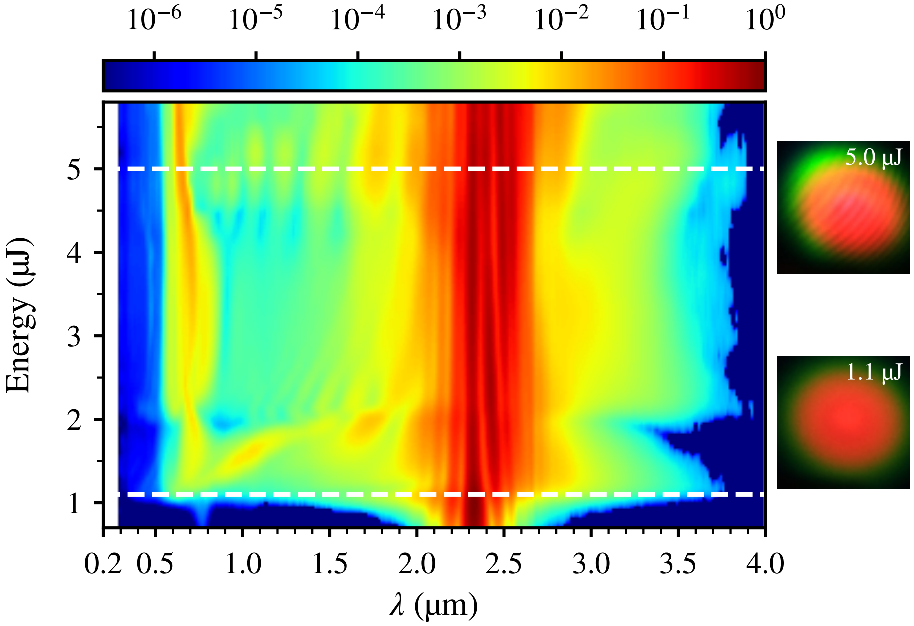

Figure 3.2: Spectral broadening in YAG versus the input pulse energy. The insets on the right show the visual appearance of the output beam at various stages of spectral broadening.

Figure 3.2 presents the dynamics of the spectral broadening in YAG versus the input pulse energy. In general, in the input pulse energy range of 0.7–2.0 μJ (1.1–3.2 P_{cr}) the spectral dynamics in YAG is qualitatively similar to those observed in fused silica and reveals the regimes of spectral broadening associated with plasma-induced and GVD-induced pulse compression.

The early phase of spectral broadening is characterized by the TH generation and spectral broadenings around the carrier wavelength and the TH peak, which overlap with the input pulse energy of 1.0 μJ. However, owing to very large phase mismatch for TH generation as due to large dispersion of the crystal, the detected TH peak is much weaker than that in fused silica and hence is not observed by visual means.

The spectral superbroadening, which is associated with GVD-induced self-compression of the driving pulse and formation of the light bullet, is observed with an input pulse energy of 1.05 μJ, corresponding to the input pulse power of 1.6 P_{cr}. The widest SC spectrum is measured with the input pulse energy of 1.1 μJ and spans from 350 nm to 3.8 μm, with the blue-shifted peak centered at 620 nm.

Although LiF has the largest bandgap among the solid-state dielectric media, formation of long-living color centers resulting from irradiation by intense laser pulses is often considered as a major drawback to its potential applications in nonlinear optics and SC generation in particular. However, recent experiments demonstrate that the color centers only weakly modify the UV portion of the SC spectrum on the long-term time scale [103]. Color centers are also shown to produce intense luminescent tracks in the sample under mid-infrared excitation, which nevertheless do not alter the filamentation process in general [104].

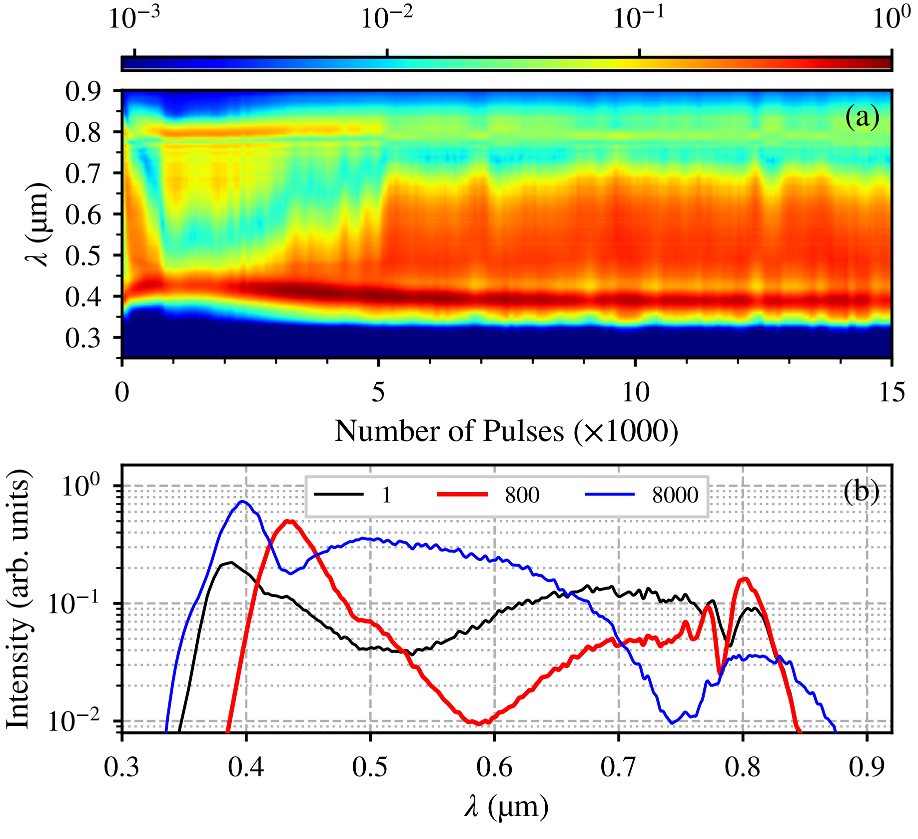

Figure 3.3: (a) Time evolution of the ultraviolet-near infrared part of the SC spectrum in LiF as recorded with the input pulse energy of 10.2 µJ. (b) Examples of the individual SC spectra after a different number of laser shots.

Therefore, we first investigated the impact of color center formation on the SC spectrum. The time evolution of the SC spectrum was recorded in the ultraviolet – near infrared spectral range (200–900 nm) using a fiber spectrometer which operated in a single shot regime. Figure 3.3 shows the modification of the SC spectrum as a function of the number of laser shots, as recorded with

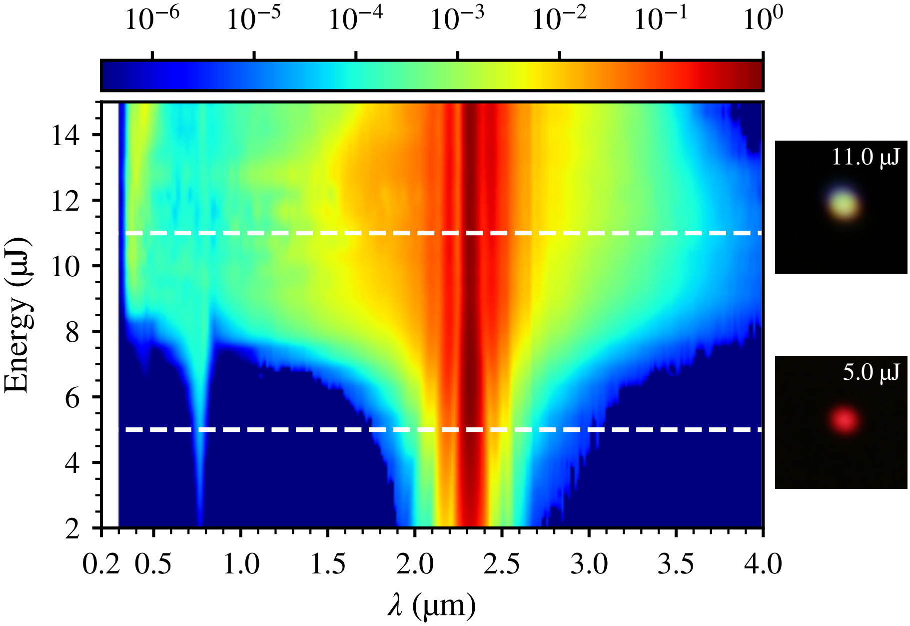

Figure 3.4: Spectral broadening in LiF versus the input pulse energy. The insets on the right show the visual appearance of the output beam at various stages of spectral broadening.

a fixed input pulse energy of 10.2 µJ.

Formation of the color centers starts almost immediately, after just a few tens of laser shots, as manifested by the changes of the SC spectrum. Eventually, after approximately 5000 laser shots, the shape of the SC spectrum eventually stabilizes and remains constant over the rest of the measurement time. Interestingly, in a modified crystal, the altered SC spectrum shows a marked increase of the spectral intensity in the visible spectral range and even broader ultraviolet extension as compared to that in an unmodified crystal, see Fig. 3.3(b).

These findings suggest that although the color center formation alters the SC spectral shape, the process of spectral broadening and SC generation in a modified volume of the crystal remains almost unaffected. This is verified by studying the dynamics of the spectral broadening in a modified crystal, which reveals the above discussed phases of the spectral broadening, associated with plasma-induced and GVD-induced pulse compression, as shown in Fig. 3.4.

An apparently intense TH peak at 767 nm is readily detected even in the range of low input pulse energies, which correspond to the input pulse power range well below the critical power of self-focusing. Thereafter the plasma-induced pulse compression produces spectral broadenings around the carrier wavelength and TH; and the blue shift of the latter makes the TH radiation easily observable by the naked eye, as illustrated in the inset of Fig. 3.4. In the input pulse energy range of 6–8 µJ, alongside the spectrally broadened TH, we capture a relatively strong peak of fifth harmonic, which experiences spectral broadening as well. Eventually, the spectral broadenings around the carrier, third and fifth harmonic frequencies overlap, yielding the so-called odd harmonics-enhanced supercontinuum [102].

With an input pulse energy of 8.5 µJ (1.5 P_{cr}) an explosive spectral superbroadening due to GVD-induced pulse compression is observed. The broadest SC spectrum, which continuously covers the wavelength range from 290 nm in the ultraviolet to 4.0 µm in the mid infrared, as estimated at the 10^{-6} intensity level, is measured within an input pulse energy range of 9–13 µJ. Since the upper wavelength limit of our spectrometer is 4.0 µm and there is still an appreciable signal of the SC, the wavelength of the mid-infrared cut-off edge of the SC could be extrapolated at 4.3–4.4 µm. The generated SC spectrum exhibits an intense blue-shifted peak, which is centered at 380 nm. With further increase of the input pulse energy, a slight red shifting of the blue peak along with a slight shrinking of the mid-infrared side of the SC spectrum is observed. However, the effect of spectral shrinking in the case of LiF are less pronounced as compared to measurements in fused silica and YAG.

Summary of the results

An investigation of the dynamics of spectral broadening and supercontinuum generation in the range of anomalous GVD in fused silica, YAG and LiF nonlinear crystal demonstrated the generation of ultrabroadband, multioctave SC, which continuously covers the wavelength range from the ultraviolet to the mid-infrared. The general dynamics of the spectral broadening versus the input pulse energy was found to be very similar in all investigated nonlinear media, despite the differences of their relevant linear and nonlinear parameters. All of them exhibit two phases of spectral broadening – plasma-induced and anomalous group velocity dispersion-induced compression of the driving pulse. While the formation of the color centers in LiF alters SC spectral shape, but generation process itself remains almost unaffected. Under given operating conditions (the input pulsewidth, the length of the nonlinear medium and the focusing condition), there exists an optimum input pulse energy, which produces the broadest SC spectrum, allowing to optimize the practical setups for SC generation with mid-infrared laser pulses.

CONCLUSIONS

1. Measurements of the spatiotemporal intensity profiles of an optical filament in the regime of weak anomalous GVD of fused silica and sapphire (at 1.45 µm) demonstrated pulse splitting into two sub-pulses which represent a pair of light bullets with spectrally shifted carrier frequencies. In contrast, in the regimes of moderate (at 1.8 µm) and strong (at 2.25 µm) anomalous GVD, formation of a single self-compressed quasistationary light bullet with an universal spatiotemporal shape comprised of an extended ring-shaped periphery and a localized intense core that carries nearly or almost bandwidth-limited self-compressed pulse was recorded.

2. Very different evolutions of the spectral broadening versus the input pulse energy when the incident beam was focused either onto the input face or inside the nonlinear medium were uncovered. In particular, when the input beam was focused inside the crystal, a surprising variation of the spectral width as a function of the input pulse energy, demonstrating supercontinuum generation, its suppression, and eventually, its recovery, was recorded. The experimental findings were reproduced by the numerical simulations in great detail, revealing a specific filamentation and supercontinuum generation scenario, which relies on strong reshaping of the wave packet due to defocusing and absorption of free electron plasma, subsequent replenishment of the pulse on the propagation axis, and its splitting.

3. Periodic modulation of the TH spectrum is a signature of a double-peaked temporal profile of TH pulse that was measured by the cross-correlation technique. This suggests that the third-harmonic pulse naturally consists of free and driven components that occur at the boundary of a vacuum and a nonlinear dielectric medium in the conditions of large group and phase velocity mismatch. The free TH component travels with the group velocity set by the material dispersion, and walks-off from the fundamental pulse, while the driven TH component travels with the velocity of the nonlinear polarization, i.e., with the velocity of the intensity peak of the fundamental pulse.

4. Evolutions of the spectra, energy oscillations, and conversion efficiencies of fifth and seventh harmonics in a solid state medium, demonstrate that these harmonics are generated solely by cascaded four-wave mixing via cubic nonlinearity of the material, without any detectable contribution of higher order nonlinearities.

5. With the input pulse intensities exceeding several TW/cm^2, the plasma-dominated filamentation regime sets in, leading to plasma-induced compression of the driving pulse, which in turn induces spectral superbroadening around the carrier wavelength, as well as facilitates large scale spectral broadening of third, fifth and seventh harmonics via cross phase modulation. This particular propagation regime results in the generation of harmonics-enhanced supercontinuum, with the spectrum spanning more than 4 octaves from the ultraviolet to the mid-infrared.

6. High dynamic range spectral measurements allowed clear distinction between different mechanisms of spectral broadening: plasma-induced and anomalous group velocity dispersion-induced compression of the driving pulse, which are characterized by the occurrence of specific spectral signatures. In particular, the Kerr-dominated filamentation regime results in the group velocity dispersion-induced pulse compression, which originates from the opposite effects of self-phase modulation and anomalous GVD, leading to formation of the light bullets. Light bullets produce an intense multioctave supercontinuum emission, whose spectrum spans from the ultraviolet to the mid-infrared with a characteristic blue peak located in the visible spectral range.

SANTRAUKA LIETUVIŲ KALBA

Įvadas

Femtosekundinės šviesos gijos skaidriuose dielektrikuose susidaro dėl ekstremalios šviesos ir medžiagos sąveikos, kuri aprėpia platų netiesinių reiškinių spektrą: šviesos pluoštų ir impulsų saviveiką, netiesinę sugertį, laisvųjų elektronų plazmos atsiradimą, erdvėlaikines transformacijas bei didelio masto dažnių spektro plitimą – superkontinuumo generaciją [1]. Šviesos gija – dinaminė struktūra su labai siaura ir intensyvia centrine smaile, o aplink ją yra žemo intensyvumo, bet didelės energijos periferinė dalis. Dėl netiesinių nuostolių, fokusavimosi ir difrakcijos smailė ir periferija yra stipriai surištos Beselio tipo pluošte [2,3]; sub-difrakcinis centrinės smailės sklidimas yra palaikomas kūginės energijos pernašos iš periferijos [4].

Matomiausia šviesos gijų formavimosi pasekmė – superkontinuumo (SK) generacija – plataus spektro, erdvėje ir laike koherentinės, mažais kampais diverguojančios spinduliuotės atsiradimas su spalvota kūgine emisija. Superkontinuumo spinduliuotė yra unikalus ir plačiai pritaikomas ypač plataus spektro spinduliuotės šaltinis su dideliu spektrinės galios tankiu ir labai geru koherentiškumu [5]. SK generacija skaidriuose kietojo kūno dielektrikuose yra labai naudingas, kompaktiškas, efektyvus ir patikimas metodas, kai reikia ypač plataus spektro spinduliuotės įvairiose optinio spektro srityse. SK spinduliuotė yra plačiai naudojama laiko skyros spektroskopijoje, ultrasparčiojoje netiesinėje optikoje ir fotonikoje [6–9].

SK generacija žadinant femtosekundiniais lazerio impulsais skirtinguose skaidriuose kietuosiuose kūnuose normaliosios grupinių greičių dispersijos (GGD) srityje yra gerai ištirta eksperimentiniai ir teoriškai, jos fizikinis mechanizmas yra gerai žinomas. Katastrofiškas fokusavimasis sustabdomas dėl impulso skilimo netiesiniame židinyje [10]. Atsiradę sub-impulsų frontai savaime statėja dėl sąveikos tarp netiesinių efektų ir medžiagos dispersijos. Dėl to laike atsiranda labai aštrūs intensyvumo gradientai (optinės smūginės bangos), kurių atsiradimas stipriai išplečia spektrą – generuojamas SK. Dažniai su raudonu poslinkiu yra generuojami dėl statėjančio priekinio sub-impulso priekinio fronto, o dažniai su mėlynu poslinkiu – dėl galinio sub-impulso galinio fronto. Dėl to abu sub-impulsai įgauna skirtingus nešančiuosius dažnius ir sklinda skirtingais grupiniais greičiais [11].

Nauji aukštos smailinės galios artimos ir vidurinės infraraudonosios srities lazerinės šviesos šaltiniai, beveik visi veikiantys optinio parametrinio stiprinimo principu [12–14] leidžia eksperimentiniai tirti šviesos gijų generaciją plataus draustinės energijos tarpo dielektrikuose jų anomalios GGD srityje. Buvo pastebėtas ypač didelis (beveik 10 kartų) gijos prailgėjimas [15] ir ypač plati

SK spinduliuotė [16] formuojant šviesos gijas lydytame kvarce femtosekundiniais 1.55 µm centrinio bangos ilgio impulsais. Neseniai buvo parodytas ir šviesos gijų generavimas žadinant žymiai ilgesnio bangos ilgio impulsais IAG kristale, kai buvo sugeneruotas daugiau nei 3 oktavų pločio SK, kurio spektras apima diapazoną nuo ultravioletinės iki vidurinės infraraudonosios srities [17].

Šie tyrimai parodė, jog sklindant intensyviems femtosekundiniams lazeriniams impulsams skaidriuose dielektrikuose jų anomalios GGD srityje, yra pasiekimas naujas netiesinės sąveikos režimas, kuriame kartu vyksta pluošto fokusavimasis ir impulso laikinė spūda dėl sąveikos tarp fazės moduliavimosi ir anomalios GGD. Šiame režime gali būti įmanoma suspausti impulsus iki kelių optinių ciklų [18, 19] ir suformuoti erdvelaikines šviesos kulkas – erdvėje ir laike lokalizuotus netiesinius darinius, kurie beveik išlaiko savo formą nusklidus daugelio difrakcinių ir dispersinių ilgių atstumus [20] arba patiriančius kelis spūdos ciklus ties didesnėmis žadinimo energijomis [21]. Detalūs matavimai parodė, jog šviesos kulkos turi daugiaspalvių Beselio pluoštų savybių ir ryškiai skiriasi nuo solitoninių darinių [22]. Ypatingai platus šviesos kulkos SK spektras [23] turi plačias taikymų galimybes ultrasparčiojoje molekulių spektroskopijoje bei šiuo metu sparčiai besivystančioje vidurinės IR netiesinės optikos srityje, generuojant keleto optinių ciklų trukmės impulsus, kuriuos būtų galima stiprinti iki ypač didelių smailinių intensyvumų [24, 25].

Taip pat, žadinant SK su vidurinės IR srities impulsais kartu yra generuojamos nelyginės harmonikos, kurių bangos ilgiai pataiko į daugelių netiesinių dielektrinių medžiagų skaidrumo diapazoną infraraudonojoje, regimojoje ir ultravioletinėje srityse, kur yra paprasčiau jas detektuoti. Žadinant vidurinės IR srities impulsais ore buvo registruota trečiosios, penktosios [26–28] ir septintosios [29] harmonikų generacija. Taip pat buvo registruojamos žemesnių eilių harmonikos: puslaidininkiuose [30], skysčiuose [31, 32] ir kietuosiuose kūnuose [33–35]. Yra moksliškai ir praktiškai labai svarbu suprasti harmonikų generacijos mechanizmus. Nelyginių žemos eilės (trečiosios, penktosios, septintosios, ir t.t.) harmonikų generacija perturbaciniame netiesinės sąveikos režime – potencialus būdas tiesiogiai išmatuoti medžiagų netiesinius optinius parametrus. Taip pat, tokiu būdu galima įvertinti aukštesnių eilių Kerro efekto ir netiesiškumo sotinimo įtaką dujinėse [36, 37] ir kietojo kūno [38] terpėse.

Darbo tikslas

Šios disertacijos tikslas – ištirti intensyviais lazeriniais impulsais žadinamų šviesos gijų formavimosi režimus skaidriuose dielektrikuose nulinės ir anomalios GGD srityse ir charakterizuoti svarbius netiesinius efektus (pvz., plazmos atsiradimą, impulsų spūdą, nelyginių žemiausios eilės harmonikų generaciją) vykstančius formuojantis šviesos gijoms ir generuojant ypač plataus spektro daugiaoktavio superkontinuumo spinduliuotę.

Sprendžiami uždaviniai

- Erdvėlaikinis šviesos gijų formavimosi dinamikos charakterizavimas safyre ir lydytame kvarce esant silpnai, vidutinei ir stipriai anomaliai grupinių greičių dispersijai.

- Išorinės fokusavimo geometrijos įtakos tyrimas spektro plitimo ir superkontinuumo generacijos dinamikai safyro kristale nulinės grupinių greičių dispersijos sąlygomis.

- Vidurinės infraraudonosios srities impulsais žadinamų šviesos gijų formavimosi ir superkontinuumo generacijos skaidriuose dielektrikuose (CaF_2) metu generuojamų nelyginių žemiausios eilės harmonikų (trečiosios, penktosios, septintosios) analizė.

- Vidurinės infraraudonosios srities impulsais sukelto spektrinio plitimo ir daugiaoktavio SK generacijos didelio draustinės energijos tarpo dielektrikuose (lydytame kvarce, IAG ir LiF) spektrinės dinamikos charakterizavimas dideliame dinaminiame diapazone.

Mokslinis darbo naujumas

- Nors lydytas kvarcas ir safyras turi skirtingus GGD koeficientus ir netiesinius lūžio rodiklius, pradinis Gauso formos bangų paketas transformavosi erdvėje ir laike labai panašiai abiejose netiesinėse terpėse. Buvo parodyta, jog vidutinės ir stiprios anomalios GGD sąlygomis, formuojasi charakteringas žiedo su smaile centre formos erdvėlaikinis intensyvumo skirstinys, kuris yra universalus šviesos kulkoms kietojo kūno terpėse su Kerro netiesiškumu. Silpnos anomalios GGD sąlygomis yra stebimas impulso skilimas, panašiai kaip ir normalios GGD sąlygomis. Tačiau skirtumai išryškėja erdvėlaikyje, kur matosi jog abu skilę sub-impulsai sudaro būdingos „O“ formos erdvėlaikinius skirstinius, kas leidžia juos traktuoti kaip kvazi-stacionarias erdvėlaikines šviesos kulkas.

- Parodyta jog yra kokybinis skirtumas spektro priklausomybėje nuo žadinančiojo impulso energijos tarp fokusavimo ant netiesinės terpės paviršiaus ir fokusavimo į vidų. Kai žadinimo impulso geometrinis židinys yra kristalo viduje, SK generacijos slenkstis sumažėja 25%, tačiau SK plotis stipriai keičiasi nuo žadinimo energijos. Po pradinės SK generacijos, didėjant žadinimo energijai pasiekiama situacija, kai SK beveik pilnai išnyksta, o po to atsiranda vėl. Tikėtina, jog šios SK generacijos savybės yra universalios ir gali būti panaudotos skirtingų SK generacijos schemų optimizavimui, kai SK yra generuojamas ilgesniais femtosekundiniais impulsais, kuriuos generuoja neseniai sukurtos Yb:KGW, Yb:KYW, Yb:šviesolaidis ir panašios lazerinės sistemos.

- Parodyta, kad esant dideliam fazinių ir grupinių greičių nederinimui, TH impulsas yra sudarytas iš dviejų skirtingais grupiniais greičiais sklindančių smailių, atitinkančių laisvąją ir priverstinę bangas, kurios yra generuojamos riboje tarp vakuumo ir netiesinės terpės. Laisvosios ir priverstinės bangos TH impulsai sklinda skirtingais grupiniais greičiais, todėl atstumas laike tarp jų ilgėja nuo sklidimo atstumo, kas sąlygoja moduliacijos TH spektre dinamiką.

- Trečiosios, penktosios ir septintosios harmonikos energijų svyravimai, spektrai ir keitimo efektyvumai buvo išmatuoti keičiant sklidimo ilgį netiesinėje terpėje, žadinančio impulso intensyvumą ir energiją. Rezultatai parodė, jog penktosios ir septintosios harmonikų generacijoje visiškai dominuojantis procesas yra pakopinis keturbangis maišymas, nulemtas trečiosios eilės netiesiškumo, o aukštesnių eilių netiesiškumų įtaka yra nestebima esant žadinimo energijoms iki 15 TW/cm^2.

- Nelyginių harmonikų generacija prisideda prie spartaus spektro išplitimo kietojo kūno dielektrikuose pereinant į plazmos sąlygojamą saviveikos režimą. Plazmos sąlygojamas impulsų trumpėjimo mechanizmas lemia spektro plitimą aplink pirmąją harmoniką. Dėl kryžminės fazinės moduliacijos įvyksta ir trečiosios, penktosios, bei septintosios harmonikų spektrų plitimas. To pasekmėje galiausiai atsiranda SK apimantis daugiau negu keturias oktavas nuo ultravioletinės iki vidurinės infraraudonosios srities. Persiklojantys harmonikų spektrai stipriai praplečia SK į ultravioletinę sritį, gerokai toliau negu tipinė „mėlynoji“ SK smailė nulemta medžiagos GGD.

- Spektrinės dinamikos priklausomybės nuo žadinančiojo impulso energijos plataus draustinės energijos tarpo kietojo kūno dielektrikuose atskleidė skirtingus spektrinio plitimo mechanizmus dėl plazmos sąlygojamo ir anomalios grupinių greičių dispersijos sąlygojamo žadinimo impulso trumpėjimo, pasižyminčius charakteringais spektriniais pėdsakais. Parodyta, kad esant apibrėžtoms eksperimento sąlygomis (žadinimo impulso trukmei, netiesinės terpės ilgiui ir fokusavimo sąlygoms) egzistuoja optimali žadinimo energija, ties kuria generuojamas plačiausias SK spektras. Tai gali padėti optimizuoti SK generacijos schemas, žadinant viduriniosios infraraudonosios srities impulsais.

Ginamieji teiginiai

- Kietųjų kūnų anomalios GGD srityje, besifokusuojantis bangų paketas transformuojasi į vieną optinę kulką, pasižyminčią universaliu „O“ formos erdvėlaikiniu intensyvumo skirstiniu, kurį sudaro žiedo formos periferija ir kompaktiškas branduolys nešantis suspaustą, beveik spektru ribotą impulsą.

- Išorinė pluošto fokusavimo geometrija, tokia kaip žadinimo pluošto sąsmaukos pozicija ties netiesinės terpės įvadiniu paviršiumi arba jos viduje, stipriai lemia spektrinio plitimo dinamiką.
- Trečiosios harmonikos impulsas, sugeneruotas kietajame kūne didelio fazinių ir grupinių greičių nederinimo sąlygomis, yra sudarytas iš dviejų skirtingais grupiniais greičiais sklindančių smailių, atitinkančių laisvąją ir priverstinę bangas.
- Pakopinis keturbangis maišymas, nulemtas trečiosios eilės netiesiškumo yra dominuojantis procesas penktosios ir septintosios harmonikų generacijoje, vykstant viduriniosios infraraudonosios srities lazerinio impulso fokusavimuisi kietojo kūno terpėse.
- Nelyginių harmonikų generacija ir jų spektrų plitimas duoda svarbų įnašą ypač plataus, daugiaoktavio SK spektro generacijai kietojo kūno terpėse.
- Sąveika tarp fazės moduliavimosi ir anomalios GGD lemia šviesos kulkų su daugiaoktaviu SC spektru atsiradimą.

Atlikti tyrimai lyginantys erdvėlaikines šviesos gijų savybes, žadinant nulinės ir anomalios grupinių greičių dispersijos sąlygomis safyro ir lydyto kvarco kristaluose. Šiuo tikslu atlikti detalūs šviesos gijų erdvėlaikinės struktūros ir jos kitimo dinamikos matavimai keičiant 100 fs trukmės žadinančiųjų impulsų bangos ilgį nuo 1.4 iki 2.2 µm [**A1**]. Nustatyta, kad kai žadinimo bangos ilgis (1.4 µm) yra artimas medžiagos grupinių greičių dispersijos nuliui (1.31 µm safyrui ir 1.27 µm lydytam kvarcui), abiem atvejais pradinis impulsas skyla į du sub-impulsus, kurie tolesnio sklidimo metu tolsta vienas nuo kito dėl skirtingų nešančiųjų dažnių ir grupinių greičių dispersijos, o sub-impulsų intensyvumai sklidimo metu keičiasi: pradžioje formuojasi intensyvus galinis sub-impulsas, o po to intensyvus priekinis sub-impulsas. Šiuo atveju šviesos kulkos nėra generuojamos, o šviesos gijos laikinė ir erdvinė dinamika yra iš esmės identiška tai, kuri buvo išmatuota normalios grupinių greičių dispersijos atveju. Esant didesnei anomaliai grupinių greičių dispersijai (žadinimo bangos ilgis 1.8 µm), lydytame kvarce ir safyre formuojamos šviesos kulkos, turinčios beveik identiškus O-formos erdvėlaikinius intensyvumo skirstinius. Dar didesnių anomalios GGD verčių atveju (žadinimo bangos ilgis 2.2 µm), šviesos kulkų formavimosi dinamika tampa sudėtinga: pradiniame etape stebimas impulso sklilimas ir energijos persiskirstymas erdvėje, tačiau tolesnio sklidimo metu galiausiai formuojasi šviesos kulka, kurios erdvėlaikinis intensyvumo skirstinys konverguoja į O-formą – intensyvią smailę, apsuptą žiedo formos periferinės dalies. Šis tyrimas įrodė, kad visos šviesos kulkos, kurios generuojamos fokusuojantis intensyviems lazerio impulsams terpėse su anomalia grupinių greičių dispersija, plačioje impulsų ir medžiagos parametrų erdvėje turi universalų charakteringos O-formos erdvėlaikinį intensyvumo skirstinį ir gali būti traktuojamos kaip netiesinės O-bangos [105].

Ištirta superkontinuumo generacija safyre jo nulinės dispersijos srityje (1.3 µm) žadinant 210 fs trukmės impulsais, keičiant energiją ir išorinę fokusavimo geometriją [**A2**]. Fokusuojant ant įvadinio kristalo paviršiaus, kai žadinimo impulso energija pasiekia 2 µJ įvyksta spartus spektro plitimas ir SK spektro plotis mažai priklauso nuo tolimesnio energijos didinimo, dengiant sritį tarp 470 nm ir 1.8 µm (10^{-5} intensyvumo lygyje). Liuminescencinių pėdsakų matavimai rodo netiesinio židinio atsiradimą ties kristalo galiniu paviršiumi kartu su SK atsiradimu ir jo artėjimą prie priekinio paviršiaus didėjant energijai. Kitokia spektro dinamika registruota fokusuojant į kristalo vidų – šiomis sąlygomis yra pasiekimas 25% žemesnis SK generacijos slenkstis (1.48 µJ), tačiau toliau didinant energiją SK generacija yra beveik pilnai slopinama 2.0–2.5 µJ energijų intervale, o nuo 2.5 µJ vėl pilnai atsistato. SK nuslopimas ir atsistatymas įvyksta labai siaurame energijų intervale. Žiūrint į liuminescencijos pėdsakus, pirmas maksimumas visada matosi ir nekeičia savo trajektorijos.

Tačiau iškart po generacijos pradžios stebimas ir antras maksimumas judantis link kristalo galinio paviršiaus ir jo dingimas sutampa su SK slopinimu. Po to, ties SK atsistatymo energija, antrasis maksimumas atsiranda ties galiniu paviršiumi ir juda link kristalo įvadinio paviršiaus. Tikėtina, kad žemesnis SK generacijos slenkstis, bei jo nuslopimas ir atsistatymas didinant žadinimo energiją yra universali SK generavimo savybė žadinant impulsais kurių trukmė yra tarp kelių šimtų femtosekundžių ir pikosekundės netiesinės terpės nulinės GGD srityje.

Atliktas išsamus trečiosios (TH) ir penktosios (PH) harmonikų generacijos tyrimas, žadinant 2 µm centrinio bangos ilgio ir 20 fs trukmės impulsais plonoje, keičiamo storio kalcio fluorido plokštelėje [**A3, A4**]. Nustatyta, kad TH impulsas yra sudarytas iš dviejų, skirtingais grupiniais greičiais sklindančių impulsų, kurie atitinka laisvąją ir priverstinę bangas. Dvismailis TH impulsas gimsta vakuumo ir netiesinio dielektriko riboje dėl didelio fazinių ir grupinių greičių nederinimo; panašus reiškinys vyksta antrosios harmonikos generacijos atveju, o matematiškai laisvosios ir priverstinės bangų impulsai atitinka vienalytės ir nevienalytės bangų lygties sprendinius [71]. Laisvosios ir priverstinės bangų egzistavimas TH generacijos atveju buvo numatytas teoriškai [69], tačiau niekada iki šiol nebuvo eksperimentiškai stebėtas. Šiame tyrime kryžminės koreliacijos metodu tiesiogiai išmatuoti laisvosios ir priverstinės TH bangų impulsai. Šie impulsai sklinda skirtingais grupiniais greičiais: priverstinis impulsas sklinda žadinančiojo (pagrindinės harmonikos) impulso, kuris kuria netiesinę poliarizaciją, grupiniu greičiu, o laisvasis impulsas sklinda grupiniu greičiu, kurį lemia medžiagos dispersija. Didėjant sklidimo ilgiui, laisvasis ir priverstinis impulsai tolsta vienas nuo kito, sąlygodami ryškėjantį interferencinį vaizdą registruojamame TH spektre. Taipogi užregistruotos TH energijos osciliacijos sklidimo metu, kurių periodas atitiko koherentinį sąveikos ilgį ir parodyta, kad didinant pradinio impulso energiją (intensyvumą), osciliacijų periodas mažėja dėl pagrindinio dažnio impulso fazės moduliavimosi ir kryžminės fazės moduliacijos tarp pagrindinio dažnio ir TH impulsų. Išmatavus trečiosios ir penktosios harmonikų spektro dinamiką keičiant sklidimo ilgį ir palyginus su skaitmeninio modeliavimo rezultatais, nustatyta, kad penktosios harmonikos spinduliuotė yra generuojama per pakopinį trečiosios eilės netiesiškumą (keturbangį maišymą tarp pagrindinio dažnio ir TH spinduliuotės) [74], o aukštesniųjų eilių netiesiškumo įtaka yra praktiškai nepastebima. Šis faktas buvo patvirtintas ir harmonikų energijų matavimais, kurie buvo atlikti kaip kokybinis testas [37], siekiant nustatyti aukštesniųjų eilių netiesiškumų įtaką vykstant netiesinei intensyvių femtosekundinių impulsų ir medžiagos sąveikai. Šia prasme, šio tyrimo rezultatai parodė, kad trečiosios ir penktosios harmonikų spinduliuotės energijos keitimo našumai visiškai atitinka standartinį sąveikos modelį, kuris remiasi medžiagos atsaku per kubinį netiesiškumą, o numanomi netiesiškumo sotinimo ir aukštesniųjų eilių netiesiškumų sąlygojami reiškiniai [38] nėra stebimi esant impulso intensyvumui iki 15 TW/cm^2.

Įvadinių impulsų intensyvumui viršijus keletą TW/cm^2, užregistruota stipri tiek žadinančiojo impulso, tiek individualių harmonikų spektrų plėtra [**A5**]. Skaitmeninio modeliavimo rezultatai detaliai atkartojo eksperimento rezultatus ir atskleidė, kad žadinančiojo impulso spektro plėtra įvyksta dėl laisvųjų elektronų plazmos sąlygojamos impulso spūdos, t.y. pasiekus vadinamąjį plazmos sąlygojamą saviveikos režimą. Tuomet ant sklidimo ašies pasiekiamas didelis laisvųjų elektronų plazmos tankis, kuris defokusuoja ir išstumia į periferiją (tolyn nuo sklidimo ašies) galinę impulso dalį, dėl ko impulsas efektyviai trumpėja, o jo galinis frontas smarkiai statėja. Kadangi TH, PH ir SH impulsai sklinda lėčiau nei žadinantysis impulsas, jie atsiduria po stačiu galiniu žadinančiojo impulso frontu, kas savo ruožtu dėl kryžminės fazės moduliacijos reiškinio lemia smarkų individualių harmonikų spektrų išplitimą į mėlynąją pusę. Pasiekus tam tikrą sklidimo atstumą (pvz. 1.4 mm, esant 4.8 TW/cm^2 įvadiniam intensyvumui) žadinančiojo impulso ir harmonikų spektrai persikloja, susiliedami į itin plataus spektro, harmonikų spinduliuote praturtintą superkontinuumo spinduliuotę, aprėpiančią daugiau nei 4 optinių oktavų bangos ilgių diapazoną nuo ultravioletinės iki vidurinės infraraudonosios spektro srities. Šie tyrimai taip pat parodė, kad plazmos sąlygojamas impulsų trumpėjimo mechanizmas yra universalus ir nepriklauso nuo medžiagos grupinių greičių dispersijos ženklo.

Atlikti daugiaoktavio superkontinuumo generacijos išsamius spektrinės dinamikos priklausomybės nuo žadinimo impulso energijos tyrimai ir kitose plačiai naudojamose dielektrinėse netiesinėse terpėse: lydytame kvarce, itrio aliuminio granate (YAG) ir ličio fluoride (LiF) [**A6**]. Užregistruotos didelio dinaminio diapazono spektrogramos parodė, kad didinant žadinančiojo impulso energiją, pasireiškia dvi skirtingos spektro plėtros fazės, kurias lemia skirtingi impulso spūdos mechanizmai. Nustatyta, kad palyginti nedidelių žadinančiojo impulso energijų intervale (kuomet impulso galia yra mažesnė ar nežymiai viršija kritinę fokusavimosi galią) spektro plėtrą lemia laisvųjų elektronų plazmos sąlygojama žadinačiojo impulso spūda, dėl kurios plinta žadinančiojo impulso ir nelyginių harmonikų spektras. Šiame etape stebima SK spinduliuotė yra palyginti žemo intensyvmo, o jos spektre gerai matomos trečiosios, o lydyto kvarco ir LiF atveju, ir penktosios harmonikų smailės. Viršijus kritinę fokusavimosi galią 1.2–1.6 karto, ima dominuoti impulsų spūda dėl anomalios grupinių greičių dispersijos ir fazinės moduliacijos, t.y. pereinama į šviesos kulkų generacijos režimą. Šiuo atveju SK spektruose išryškėja charakteringos vadinamosios „mėlynosios“ smailės regimojoje spektro srityje, o patys spektrai tampa platesni bei tolydesni. Šie spektro plėtros dėsningumai stebėti visuose trijuose tirtuose kristaluose, nepaisant to, kad jų tiesinės ir netiesinės savybės (draustinių energijų tarpas, netiesiškumas ir dispersija) smarkiai skiriasi, kas patvirtina, kad spektro plėtrą lemiantys impulsų spūdos mechanizmai yra universalūs. Taip pat surastos optimalios eksperimentinės sąlygos kuomet gaunami patys plačiausi SK spektrai: lydytame kvarce nuo 310 nm iki 3.75 µm (3.6 optinės oktavos), YAG nuo 350 nm iki 3.7 µm (3.4 optinės oktavos), o LiF nuo 290 nm iki 4.3 µm (3.9 optinės oktavos). Taip pat atlikti detalius laikinės spektrinės dinamikos tyrimai LiF kristale, kuris turi patį didžiausią draustinės juostos tarpą (13.6 eV) iš visų dielektrinių kristalų, tačiau retai naudojamas dėl efektyvios spalvinių centrų generacijos [103]. Iš tiesų, atliktuose eksperimentuose stebėtas labai spartus (kelių sekundžių bėgyje, esant 500 Hz impulsų pasikartojimo dažniui) spalvinių centrų atsiradimas, kuris modifikavo superkontinuumo spektro formą. Tačiau esant ilgesniems ekspozicijos laikams, pastebėta, kad SK spektro forma nusistovi ir toliau nebekinta, o spalvinių centrų susidarymas fizikiniams reiškiniams, lemiantiems spektro plėtrą, įtakos neturi.

Išvados

1. Šviesos gijos erdvėlaikinio intensyvumo skirstinio matavimai silpnos anomalios GGD sąlygomis lydytame kvarce ir safyre (ties 1.45 µm) rodo impulso skilimą į dų sub-impulsus atitinkančius dvi šviesos kulkas su vienas kito atžvilgiu pastumtais nešančiais bangos ilgiais. Tačiau, vidutiniškai (ties 1.8 µm) ir stipriai anomalios GGD (ties 2.25 µm) sąlygomis, formuojasi tiktai viena kvazi-stacionari šviesos kulka turinti universalų erdvėlaikinį intensyvumo skirstinį, kurį sudaro žiedo formos periferija ir intensyvus kompaktiškas branduolys nešantis suspaustą beveik spektru ribotą impulsą.

2. Žadinimo pluošto fokusavimas ant įvadinio paviršiaus arba į netiesinės terpės vidų pasižymi kokybiškai skirtingomis spektrinio plitimo dinamikomis nuo žadinimo energijos. Kai žadinimo pluoštas yra fokusuojamas viduje kristalo, stebimas neįprastas spektrinio pločio kitimas keičiant žadinimo energiją, kurio metu vyksta superkontinuumo generacija, jo slopinimas, ir galų gale – atsistatymas. Eksperimentiniai rezultatai buvo patvirtinti detaliu skaitmeniniu modeliavimu, demonstruojančiu konkretų šviesos gijų formavimosi ir superkontinuumo generacijos procesą, vykstant stipriam bangų paketo formos kitimui dėl laisvųjų elektronų plazmos nulemtų defokusavimo ir sugerties, tolesnio impulso atsistatymo ant sklidimo ašies ir jo skilimo.

3. Periodinė TH spektro moduliacija rodo jog TH laikinis skirstinys turi kelias smailės, ką patvirtino kryžminės koreliacijos matavimai. Tai reiškia, jog TH impulsas yra sudarytas iš dviejų skirtingais grupiniais greičiais sklindančių smailių, atitinkančių laisvąją ir priverstinę bangas, kurios yra generuojamos riboje tarp vakuumo ir netiesinės terpės esant dideliam fazinių ir grupinių greičių nederinimui. Laisvos bangos TH impulsas sklinda grupiniu greičiu atitinkančiu medžiagos dispersiją ir nutolsta nuo žadinančiojo impulso, o priverstinės bangos impulsas sklinda netiesinės poliarizacijos greičiu – žadinančiojo impulso intensyvumo smailės greičiu.

4. Penktosios ir septintosios harmonikų spektrų, energijų svyravimų ir keitimo efektyvumų dinamika kietojo kūno terpėje rodo, jog šios harmonikos yra generuojamos grynai per pakopinį keturbangį maišymą, nulemtą medžiagos trečiosios eilės netiesiškumu be pastebimos aukštesnių eilių netiesiškumų įtakos.

5. Kai žadinančiojo impulso intensyvumas viršija kelis TW/cm^2, pereinama į plazmos sąlygojamą saviveikos režimą, kai dėl plazmos vyksta žadinančiojo impulso spūda, kas lemia pirmosios harmonikos spektro plitimą ir per kryžminę fazinę moduliaciją nulemia didelius trečiosios, penktosios ir septintosios harmonikų spektrų plitimus. Šio sklidimo režimo pasekmė – harmonikų spinduliuote praturtinta superkontinuumo spinduliuotė, kurios spektras apima virš 4 oktavų nuo ultravioletinės iki vidurinės infraraudonosios srities.

6. Aukšto dinaminio diapazono matavimai atskleidė ryškius skirtumus tarp skirtingų spektrinio plitimų mechanizmų kuriuos sąlygoja žadinančiojo impulso spūda dėl plazmos arba dėl anomalios grupinių greičių dispersijos ir kuris pasižymi charakteringais spektriniais pėdsakais. Kai saviveikos metu vyrauja Kerro efektas vyksta grupinių greičių dispersijos nulemta impulso spūda, atsirandanti dėl priešingomis kryptimis veikiančių fazinės moduliacijos ir anomalios GGD, pereinama į šviesos kulkų generacijos režimą. Šviesos kulkos sukuria intensyvią daugiaoktavio superkontinuumo spinduliuotę, kurios spektras apima diapazoną nuo ultravioletinės iki vidurinės infraraudonosios srities su charakteringa „mėlynąją“ smaile regimojoje spektro srityje.

BIBLIOGRAPHY

[1] A. Couairon, A. Mysyrowicz, Femtosecond filamentation in transparent media, Phys. Rep. **441**, 47–189 (2007).

[2] A. Dubietis, E. Gaižauskas, G. Tamošauskas, P. Di Trapani, Light filaments without self-channeling, Phys. Rev. Lett. **92**, 253903 (2004).

[3] M. A. Porras, A. Parola, D. Faccio, A. Dubietis, P. D. Trapani, Nonlinear unbalanced bessel beams: Stationary conical waves supported by nonlinear losses, Phys. Rev. Lett. **93**, 153902 (2004).

[4] A. Lotti, A. Couairon, D. Faccio, P. D. Trapani, Energy-flux characterization of conical and space-time coupled wave packets, Phys. Rev. A **81**, 023810 (2010).

[5] A. Brodeur, S. L. Chin, Ultrafast white-light continuum generation and self-focusing in transparent condensed media, J. Opt. Soc. Am. B **16**, 637–650 (1999).

[6] U. Megerle, I. Pugliesi, C. Schriever, C. F. Sailer, E. Riedle, Sub-50 fs broadband absorption spectroscopy with tunable excitation: putting the analysis of ultrafast molecular dynamics on solid ground, Appl. Phys. B **96**, 215–231 (2009).

[7] A. L. Dobryakov, S. A. Kovalenko, A. Weigel, J. L. Pérez-Lustres, J. Lange, A. Müller, N. P. Ernsting, Femtosecond pump/supercontinuum-probe spectroscopy: Optimized setup and signal analysis for single-shot spectral referencing, Rev. Sci. Instrum. **81**, 113106 (2010).

[8] H. Fattahi, H. G. Barros, M. Gorjan, T. Nubbemeyer, B. Alsaif, C. Y. Teisset, M. Schultze, S. Prinz, M. Haefner, M. Ueffing, A. Alismail, L. Vámos, A. Schwarz, O. Pronin, J. Brons, X. T. Geng, G. Arisholm, M. Ciappina, V. S. Yakovlev, D.-E. Kim, A. M. Azzeer, N. Karpowicz, D. Sutter, Z. Major, T. Metzger, F. Krausz, Third-generation femtosecond technology, Optica **1**, 45–63 (2014).

[9] A. Zheltikov, Multioctave supercontinua and subcycle lightwave electronics, J. Opt. Soc. Am. B **36**, A168–A182 (2019).

[10] A. L. Gaeta, Catastrophic collapse of ultrashort pulses, Phys. Rev. Lett. **84**, 3582–3585 (2000).

[11] A. L. Gaeta, *Spatial and Temporal Dynamics of Collapsing Ultrashort Laser Pulses* (Springer New York, New York, NY, 2009), 399–411.

[12] D. Brida, C. Manzoni, G. Cirmi, M. Marangoni, S. Bonora, P. Villoresi, S. D. Silvestri, G. Cerullo, Few-optical-cycle pulses tunable from the visible to the mid-infrared by optical parametric amplifiers, J. Opt. **12**, 013001 (2009).

[13] G. Andriukaitis, T. Balčiūnas, S. Ališauskas, A. Pugžlys, A. Baltuška, T. Popmintchev, M.-C. Chen, M. M. Murnane, H. C. Kapteyn, 90 GW peak power few-cycle mid-infrared pulses from an optical parametric amplifier, Opt. Lett. **36**, 2755–2757 (2011).

[14] J. Biegert, P. K. Bates, O. Chalus, New mid-infrared light sources, IEEE J. Sel. Topics Quantum Electron. **18**, 531–540 (2012).

[15] K. D. Moll, A. L. Gaeta, Role of dispersion in multiple-collapse dynamics, Opt. Lett. **29**, 995–997 (2004).

[16] A. Saliminia, S. L. Chin, R. Vallée, Ultra-broad and coherent white light generation in silica glass by focused femtosecond pulses at 1.5 µm, Opt. Express **13**, 5731–5738 (2005).

[17] A. Dubietis, G. Tamošauskas, R. Šuminas, V.Jukna, A. Couairon, Ultrafast supercontinuum generation in bulk condensed media, Lith. J. Phys. **57**, 133–157 (2017).

[18] J. Liu, R. Li, Z. Xu, Few-cycle spatiotemporal soliton wave excited by filamentation of a femtosecond laser pulse in materials with anomalous dispersion, Phys. Rev. A **74**, 043801 (2006).

[19] I. Gražulevičiūtė, N. Garejev, D. Majus, V. Jukna, G. Tamošauskas, A. Dubietis, Filamentation and light bullet formation dynamics in solid-state dielectric media with weak, moderate and strong anomalous group velocity dispersion, J. Opt. **18**, 025502 (2015).

[20] M. Durand, A. Jarnac, A. Houard, Y. Liu, S. Grabielle, N. Forget, A. Durécu, A. Couairon, A. Mysyrowicz, Self-guided propagation of ultrashort laser pulses in the anomalous dispersion region of transparent solids: A new regime of filamentation, Phys. Rev. Lett. **110**, 115003 (2013).

[21] S. V. Chekalin, A. E. Dokukina, A. E. Dormidonov, V. O. Kompanets, E. O. Smetanina, V. P. Kandidov, Light bullets from a femtosecond filament, J. Phys. B: At., Mol. Opt. Phys. **48**, 094008 (2015).

[22] D. Majus, G. Tamošauskas, I. Gražulevičiūtė, N. Garejev, A. Lotti, A. Couairon, D. Faccio, A. Dubietis, Nature of spatiotemporal light bullets in bulk Kerr media, Phys. Rev. Lett. **112**, 193901 (2014).

[23] S. V. Chekalin, A. E. Dormidonov, V. O. Kompanets, E. D. Zaloznaya, V. P. Kandidov, Light bullet supercontinuum, J. Opt. Soc. Am. B **36**, A43–A53 (2019).

[24] H. Pires, M. Baudisch, D. Sanchez, M. Hemmer, J. Biegert, Ultrashort pulse generation in the mid-IR, Prog. Quantum Electron. **43**, 1–30 (2015).

[25] P. Krogen, H. Suchowski, H. Liang, N. Flemens, K.-H. Hong, F. X. Kärtner, J. Moses, Generation and multi-octave shaping of mid-infrared intense single-cycle pulses, Nat. Photonics **11**, 222 (2017).

[26] J. Ni, J. Yao, B. Zeng, W. Chu, G. Li, H. Zhang, C. Jing, S. L. Chin, Y. Cheng, Z. Xu, Comparative investigation of third- and fifth-harmonic generation in atomic and molecular gases driven by midinfrared ultrafast laser pulses, Phys. Rev. A **84**, 063846 (2011).

[27] G. O. Ariunbold, P. Polynkin, J. V. Moloney, Third and fifth harmonic generation by tightly focused femtosecond pulses at 2.2 µm wavelength in air, Opt. Express **20**, 1662–1667 (2012).

[28] D. Kartashov, S. Ališauskas, A. Pugžlys, A. A. Voronin, A. M. Zheltikov, A. Baltuška, Third- and fifth-harmonic generationby mid-infrared ultrashort pulses: beyond the fifth-order nonlinearity, Opt. Lett. **37**, 2268–2270 (2012).

[29] A. Nath, J. A. Dharmadhikari, A. K. Dharmadhikari, D. Mathur, Seventh-harmonic generation from tightly focused 2 µm ultrashort pulses in air, Opt. Lett. **38**, 2560–2562 (2013).

[30] A. H. Chin, O. G. Calderón, J. Kono, Extreme midinfrared nonlinear optics in semiconductors, Phys. Rev. Lett. **86**, 3292–3295 (2001).

[31] R. Zürl, H. Graener, High-harmonic generation of mid-IR pulses in simple liquids, Appl. Phys. B **66**, 213–216 (1998).

[32] G. Mao, Y. Wu, K. D. Singer, Third harmonic generation in self-focused filaments in liquids, Opt. Express **15**, 4857–4862 (2007).

[33] F. Silva, D. Austin, A. Thai, M. Baudisch, M. Hemmer, D. Faccio, A. Couairon, J. Biegert, Multi-octave supercontinuum generation from mid-infrared filamentation in a bulk crystal, Nat. Commun. **3**, 807 (2012).

[34] J. Darginavičius, D. Majus, V. Jukna, N. Garejev, G. Valiulis, A. Couairon, A. Dubietis, Ultrabroadband supercontinuum and third-harmonic generation in bulk solids with two optical-cycle carrier-envelope phase-stable pulses at 2 µm, Opt. Express **21**, 25210–25220 (2013).

[35] K. D. Moll, D. Homoelle, A. L. Gaeta, R. W. Boyd, Conical harmonic generation in isotropic materials, Phys. Rev. Lett. **88**, 153901 (2002).

[36] M. Kolesik, E. M. Wright, J. V. Moloney, Femtosecond filamentation in air and higher-order nonlinearities, Opt. Lett. **35**, 2550–2552 (2010).

[37] M. Kolesik, D. Mirell, J.-C. Diels, J. V. Moloney, On the higher-order Kerr effect in femtosecond filaments, Opt. Lett. **35**, 3685–3687 (2010).

[38] B. Borchers, C. Brée, S. Birkholz, A. Demircan, G. Steinmeyer, Saturation of the all-optical Kerr effect in solids, Opt. Lett. **37**, 1541–1543 (2012).

[39] J. Darginavičius, N. Garejev, A. Dubietis, Generation of carrier-envelope phase-stable two optical-cycle pulses at 2 µm from a noncollinear beta-barium borate optical parametric amplifier, Opt. Lett. **37**, 4805–4807 (2012).

[40] S. Skupin, L. Bergé, Self-guiding of femtosecond light pulses in condensed media: Plasma generation versus chromatic dispersion, Physica D **220**, 14–30 (2006).

[41] D. Faccio, A. Averchi, A. Lotti, M. Kolesik, J. V. Moloney, A. Couairon, P. Di Trapani, Generation and control of extreme blueshifted continuum peaks in optical Kerr media, Phys. Rev. A **78**, 033825 (2008).

[42] J. K. Ranka, R. W. Schirmer, A. L. Gaeta, Observation of pulse splitting in nonlinear dispersive media, Phys. Rev. Lett. **77**, 3783–3786 (1996).

[43] A. Jarnac, G. Tamosauskas, D. Majus, A. Houard, A. Mysyrowicz, A. Couairon, A. Dubietis, Whole life cycle of femtosecond ultraviolet filaments in water, Phys. Rev. A **89**, 033809 (2014).

[44] Y. Silberberg, Collapse of optical pulses, Opt. Lett. **15**, 1282–1284 (1990).

[45] B. A. Malomed, D. Mihalache, F. Wise, L. Torner, Spatiotemporal optical solitons, J. Opt. B: Quantum Semiclassical Opt. **7**, R53–R72 (2005).

[46] D. Mihalache, Linear and nonlinear light bullets: Recent theoretical and experimental studies, Rom. J. Phys. **57**, 352–371 (2012).

[47] D. Frantzeskakis, H. Leblond, D. Mihalache, Nonlinear optics of intense few-cycle pulses: An overview of recent theoretical and experimental developments, Rom. J. Phys. **59**, 767–784 (2014).

[48] L. Bergé, S. Skupin, Self-channeling of ultrashort laser pulses in materials with anomalous dispersion, Phys. Rev. E **71**, 065601 (2005).

[49] S. V. Chekalin, V. O. Kompanets, E. O. Smetanina, V. P. Kandidov, Light bullets and supercontinuum spectrum during femtosecond pulse filamentation under conditions of anomalous group-velocity dispersion in fused silicalica, Quantum Electron. **43**, 326–331 (2013).

[50] E. O. Smetanina, V. O. Kompanets, S. V. Chekalin, A. E. Dormidonov, V. P. Kandidov, Anti-stokes wing of femtosecond laser filament supercontinuum in fused silica, Opt. Lett. **38**, 16–18 (2013).

[51] I. Gražulevičiūtė, G. Tamošauskas, V. Jukna, A. Couairon, D. Faccio, A. Dubietis, Self-reconstructing spatiotemporal light bullets, Opt. Express **22**, 30613–30622 (2014).

[52] I. Gražulevičiūtė, R. Šuminas, G. Tamošauskas, A. Couairon, A. Dubietis, Carrier-envelope phase-stable spatiotemporal light bullets, Opt. Lett. **40**, 3719–3722 (2015).

[53] A. Major, F. Yoshino, I. Nikolakakos, J. S. Aitchison, P. W. E. Smith, Dispersion of the nonlinear refractive index in sapphire, Opt. Lett. **29**, 602–604 (2004).

[54] D. Faccio, M. A. Porras, A. Dubietis, F. Bragheri, A. Couairon, P. Di Trapani, Conical emission, pulse splitting, and X-wave parametric amplification in nonlinear dynamics of ultrashort light pulses, Phys. Rev. Lett. **96**, 193901 (2006).

[55] M. A. Porras, A. Parola, P. D. Trapani, Nonlinear unbalanced O waves: nonsolitary, conical light bullets in nonlinear dissipative media, J. Opt. Soc. Am. B **22**, 1406–1413 (2005).

[56] F. V. Potemkin, E. I. Mareev, E. O. Smetanina, Influence of wave-front curvature on supercontinuum energy during filamentation of femtosecond laser pulses in water, Phys. Rev. A **97**, 033801 (2018).

[57] N. Garejev, G. Tamošauskas, A. Dubietis, Comparative study of multi-octave supercontinuum generation in fused silica, YAG, and LiF in the range of anomalous group velocity dispersion, J. Opt. Soc. Am. B **34**, 88–94 (2017).

[58] D. Majus, V. Jukna, E. Pileckis, G. Valiulis, A. Dubietis, Rogue-wave-like statistics in ultrafast white-light continuum generation in sapphire, Opt. Express **19**, 16317–16323 (2011).

[59] L. Zhang, T. Xi, Z. Hao, J. Lin, Supercontinuum accumulation along a single femtosecond filament in fused silica, J. Phys. D: Appl. Phys. **49**, 115201 (2016).

[60] A. K. Dharmadhikari, J. A. Dharmadhikari, D. Mathur, Visualization of focusing–refocusing cycles during filamentation in $\mathrm{BaF_2}$, Appl. Phys. B **94**, 259 (2008).

[61] D. Kudarauskas, G. Tamošauskas, M. Vengris, A. Dubietis, Filament-induced luminescence and supercontinuum generation in undoped, Yb-doped, and Nd-doped YAG crystals, Appl. Phys. Lett. **112**, 041103 (2018).

[62] A. Moroño, E. Hodgson, On the origin of the f+ centre radioluminescence in sapphire, J. Nucl. Mater. **249**, 128–132 (1997).

[63] M. Kolesik, E. Wright, A. Becker, J. Moloney, Simulation of third-harmonic and supercontinuum generation for femtosecond pulses in air, Appl. Phys. B **85**, 531–538 (2006).

[64] N. Aközbek, A. Iwasaki, A. Becker, M. Scalora, S. L. Chin, C. M. Bowden, Third-harmonic generation and self-channeling in air using high-power femtosecond laser pulses, Phys. Rev. Lett. **89**, 143901 (2002).

[65] Y. Liu, M. Durand, A. Houard, B. Forestier, A. Couairon, A. Mysyrowicz, Efficient generation of third harmonic radiation in air filaments: A revisit, Opt. Commun. **284**, 4706–4713 (2011).

[66] A. V. Mitrofanov, A. A. Voronin, S. I. Mitryukovskiy, D. A. Sidorov-Biryukov, A. Pugžlys, G. Andriukaitis, T. Flöry, E. A. Stepanov, A. B. Fedotov, A. Baltuška, A. M. Zheltikov, Mid-infrared-to-mid-ultraviolet supercontinuum enhanced by third-to-fifteenth odd harmonics, Opt. Lett. **40**, 2068–2071 (2015).

[67] R. Šuminas, G. Tamošauskas, G. Valiulis, V. Jukna, A. Couairon, A. Dubietis, Multi-octave spanning nonlinear interactions induced by femtosecond filamentation in polycrystalline ZnSe, Appl. Phys. Lett. **110**, 241106 (2017).

[68] R. Šuminas, A. Marcinkevičiūtė, G. Tamošauskas, A. Dubietis, Even and odd harmonics-enhanced supercontinuum generation in zinc-blende semiconductors, J. Opt. Soc. Am. B **36**, A22–A27 (2019).

[69] V. Roppo, M. Centini, C. Sibilia, M. Bertolotti, D. de Ceglia, M. Scalora, N. Akozbek, M. J. Bloemer, J. W. Haus, O. G. Kosareva, V. P. Kandidov, Role of phase matching in pulsed second-harmonic generation: Walk-off and phase-locked twin pulses in negative-index media, Phys. Rev. A **76**, 033829 (2007).

[70] E. Fazio, F. Pettazzi, M. Centini, M. Chauvet, A. Belardini, M. Alonzo, C. Sibilia, M. Bertolotti, M. Scalora, Complete spatial and temporal locking in phase-mismatched second-harmonic generation, Opt. Express **17**, 3141–3147 (2009).

[71] M. Mlejnek, E. M. Wright, J. V. Moloney, N. Bloembergen, Second harmonic generation of femtosecond pulses at the boundary of a nonlinear dielectric, Phys. Rev. Lett. **83**, 2934–2937 (1999).

[72] G. Valiulis, V. Jukna, O. Jedrkiewicz, M. Clerici, E. Rubino, P. DiTrapani, Propagation dynamics and X-pulse formation in phase-mismatched second-harmonic generation, Phys. Rev. A **83** (2011).

[73] D. Milam, M. J. Weber, A. J. Glass, Nonlinear refractive index of fluoride crystals, Appl. Phys. Lett. **31**, 822–825 (1977).

[74] M. Bache, F. Eilenberger, S. Minardi, Higher-order Kerr effect and harmonic cascading in gases, Opt. Lett. **37**, 4612–4614 (2012).

[75] P. Panagiotopoulos, P. Whalen, M. Kolesik, J. V. Moloney, Super high power mid-infrared femtosecond light bullet, Nat. Photonics **9**, 543–548 (2015).

[76] P. Béjot, G. Karras, F. Billard, E. Hertz, B. Lavorel, E. Cormier, O. Faucher, Harmonic generation and nonlinear propagation: When secondary radiations have primary consequences, Phys. Rev. Lett. **112**, 203902 (2014).

[77] C. R. Loures, A. Armaroli, F. Biancalana, Contribution of third-harmonic and negative-frequency polarization fields to self-phase modulation in nonlinear media, Opt. Lett. **40**, 613–616 (2015).

[78] J. Doussot, P. Béjot, O. Faucher, Impact of third-harmonic generation on the filamentation process, Phys. Rev. A **93**, 033857 (2016).

[79] N. Garejev, I. Gražulevičiūtė, D. Majus, G. Tamošauskas, V. Jukna, A. Couairon, A. Dubietis, Third- and fifth-harmonic generation in transparent solids with few-optical-cycle midinfrared pulses, Phys. Rev. A **89**, 033846 (2014).

[80] M. L. Naudeau, R. J. Law, T. S. Luk, T. R. Nelson, S. M. Cameron, J. V. Rudd, Observation of nonlinear optical phenomena in air and fused silica using a 100 GW, 1.54 µm source, Opt. Express **14**, 6194–6200 (2006).

[81] J. A. Dharmadhikari, R. A. Deshpande, A. Nath, K. Dota, D. Mathur, A. K. Dharmadhikari, Effect of group velocity dispersion on supercontinuum generation and filamentation in transparent solids, Appl. Phys. B **117**, 471–479 (2014).

[82] H. Liang, P. Krogen, R. Grynko, O. Novak, C.-L. Chang, G. J. Stein, D. Weerawarne, B. Shim, F. X. Kärtner, K.-H. Hong, Three-octave-spanning supercontinuum generation and sub-two-cycle self-compression of mid-infrared filaments in dielectrics, Opt. Lett. **40**, 1069–1072 (2015).

[83] A. Dormidonov, V. Kompanets, S. Chekalin, V. Kandidov, Gigantically blue-shifted visible light in femtosecond mid-IR filament in fluorides, Opt. Express **23**, 29202–29210 (2015).

[84] V. Shumakova, P. Malevich, S. Ališauskas, A. Voronin, A. M. Zheltikov, D. Faccio, D. Kartashov, A. Baltuška, A. Pugžlys, Multi-millijoule few-cycle mid-infrared pulses through nonlinear self-compression in bulk, Nat. Commun. **7**, 12877 (2016).

[85] P. Vasa, J. A. Dharmadhikari, A. K. Dharmadhikari, R. Sharma, M. Singh, D. Mathur, Supercontinuum generation in water by intense, femtosecond laser pulses under anomalous chromatic dispersion, Phys. Rev. A **89**, 043834 (2014).

[86] M. Durand, K. Lim, V. Jukna, E. McKee, M. Baudelet, A. Houard, M. Richardson, A. Mysyrowicz, A. Couairon, Blueshifted continuum peaks from filamentation in the anomalous dispersion regime, Phys. Rev. A **87**, 043820 (2013).

[87] S. V. Chekalin, V. O. Kompanets, A. E. Dokukina, A. E. Dormidonov, E. O. Smetanina, V. P. Kandidov, Visible supercontinuum radiation of light bullets in the femtosecond filamentation of IR pulses in fused silica, Quantum Electron. **45**, 401–407 (2015).

[88] J. Jiang, Y. Zhong, Y. Zheng, Z. Zeng, X. Ge, R. Li, Broadening of white-light continuum by filamentation in BK7 glass at its zero-dispersion point, Phys. Lett. A **379**, 1929–1933 (2015).

[89] M. Liao, W. Gao, T. Cheng, X. Xue, Z. Duan, D. Deng, H. Kawashima, T. Suzuki, Y. Ohishi, Five-octave-spanning supercontinuum generation in fluoride glass, Appl. Phys Express **6**, 032503 (2013).

[90] M. Liao, W. Gao, T. Cheng, Z. Duan, X. Xue, H. Kawashima, T. Suzuki, Y. Ohishi, Ultrabroad supercontinuum generation through filamentation in tellurite glass, Laser Phys. Lett. **10**, 036002 (2013).

[91] P. Béjot, F. Billard, C. Peureux, T. Diard, J. Picot-Clémente, C. Strutynski, P. Mathey, O. Mouawad, O. Faucher, K. Nagasaka, Y. Ohishi,

F. Smektala, Filamentation-induced spectral broadening and pulse shortening of infrared pulses in tellurite glass, Opt. Commun. **380**, 245–249 (2016).

[92] O. Mouawad, P. Béjot, F. Billard, P. Mathey, B. Kibler, F. Désévédavy, G. Gadret, J.-C. Jules, O. Faucher, F. Smektala, Mid-infrared filamentation-induced supercontinuum in As–S and an As-free Ge–S counterpart chalcogenide glasses, Appl. Phys. B **121**, 433–438 (2015).

[93] C. Vicario, B. Monoszlai, G. Arisholm, C. P. Hauri, Generation of 1.5-octave intense infrared pulses by nonlinear interactions in DAST crystal, J. Opt. **17**, 094005 (2015).

[94] R. Šuminas, G. Tamošauskas, G. Valiulis, A. Dubietis, Spatiotemporal light bullets and supercontinuum generation in β-BBO crystal with competing quadratic and cubic nonlinearities, Opt. Lett. **41**, 2097–2100 (2016).

[95] S. A. Frolov, V. I. Trunov, V. E. Leshchenko, E. V. Pestryakov, Multioctave supercontinuum generation with ir radiation filamentation in transparent solid-state media, Appl. Phys. B **122**, 124 (2016).

[96] A. A. Lanin, A. A. Voronin, E. A. Stepanov, A. B. Fedotov, A. M. Zheltikov, Multioctave, 3–18 µm sub-two-cycle supercontinua from self-compressing, self-focusing soliton transients in a solid, Opt. Lett. **40**, 974–977 (2015).

[97] E. A. Stepanov, A. A. Lanin, A. A. Voronin, A. B. Fedotov, A. M. Zheltikov, Solid-state source of subcycle pulses in the midinfrared, Phys. Rev. Lett. **117**, 043901 (2016).

[98] O. Mouawad, P. Béjot, F. Billard, P. Mathey, B. Kibler, F. Désévédavy, G. Gadret, J.-C. Jules, O. Faucher, F. Smektala, Filament-induced visible-to-mid-IR supercontinuum in a ZnSe crystal: Towards multi-octave supercontinuum absorption spectroscopy, Opt. Mater. **60**, 355–358 (2016).

[99] M. J. Weber, *Handbook of Optical Materials* (CRC Press, NY, 2003).

[100] D. Faccio, A. Averchi, A. Couairon, A. Dubietis, R. Piskarskas, A. Matijosius, F. Bragheri, M. A. Porras, A. Piskarskas, P. Di Trapani, Competition between phase-matching and stationarity in Kerr-driven optical pulse filamentation, Phys. Rev. E **74**, 047603 (2006).

[101] M. A. Porras, A. Dubietis, A. Matijošius, R. Piskarskas, F. Bragheri, A. Averchi, P. D. Trapani, Characterization of conical emission of light filaments in media with anomalous dispersion, J. Opt. Soc. Am. B **24**, 581–584 (2007).

[102] N. Garejev, V. Jukna, G. Tamošauskas, M. Veličkė, R. Šuminas, A. Couairon, A. Dubietis, Odd harmonics-enhanced supercontinuum in bulk solid-state dielectric medium, Opt. Express **24**, 17060–17068 (2016).

[103] J. Kohl-Landgraf, J.-E. Nimsch, J. Wachtveitl, LiF, an underestimated supercontinuum source in femtosecond transient absorption spectroscopy, Opt. Express **21**, 17060–17065 (2013).

[104] A. V. Kuznetsov, V. O. Kompanets, A. E. Dormidonov, S. V. Chekalin, S. A. Shlenov, V. P. Kandidov, Periodic colour-centre structure formed under filamentation of mid-IR femtosecond laser radiation in a LiF crystal, Quantum Electron. **46**, 379–386 (2016).

[105] M. A. Porras, A. Dubietis, E. Kučinskas, F. Bragheri, V. Degiorgio, A. Couairon, D. Faccio, P. D. Trapani, From X- to O-shaped spatiotemporal spectra of light filaments in water, Opt. Lett. **30**, 3398–3400 (2005).

CURRICULUM VITAE

Name: Nail
Surname: Garejev
Date of birth: 1991-01-05
Place of birth: Leningrad, USSR
E-mail: nail.garejev@gmail.com

Education:

1997–1998	"Lukiškių" secondary school, Vilnius.
1998–2009	"Naujamiesčio" secondary school, Vilnius.
2009–2013	Vilniaus University, Faculty of Physics *Bachelor degree, Cum Laude.*
2013–2015	Vilnius University, Faculty of Physics *Master degree, Magna Cum Laude.*
2015–2019	Vilnius University, Faculty of Physics, Laser Research Center *Ph.D. studies.*

Summer schools:

2014	Laserlab Training School, Riga, Latvia.
2014	International School of Physics "Enrico Fermi", Course 190 – Frontiers in Modern Optics, Varena, Italy.
2016	Frontiers of Solid State Light Sources, Vienna, Austria.

Work experience:

2013–2015	Lab assistant, engineer at Vilnius University Laser Research Center.
2015–2019	Junior researcher at Vilnius University Laser Research Center.

TRUMPOS ŽINIOS APIE AUTORIŲ

Vardas: Nail
Pavardė: Garejev
Gimimo data: 1991-01-05
Gimimo vieta: Leningrad, TSRS
El. paštas: nail.garejev@gmail.com

Išsilavinimas:

1997–1998	Vilniaus Lukiškių vidurinė mokykla.
1998–2009	Vilniaus Naujamiesčio vidurinė mokykla.
2009–2013	Vilniaus universitetas, Fizikos fakultetas *Bakalauro kvalifikacinis laipsnis, Cum Laude.*
2013–2015	Vilniaus universitetas, Fizikos fakultetas *Magistro kvalifikacinis laipsnis, Magna Cum Laude.*
2015–2019	Vilniaus universitetas, Fizikos fakultetas, Lazerinių tyrimų centras *Doktorantūra.*

Vasaros mokyklos:

2014	Laserlab Training School, Ryga, Latvija.
2014	International School of Physics "Enrico Fermi", Course 190 – Frontiers in Modern Optics, Varena, Italija.
2016	Frontiers of Solid State Light Sources, Viena, Austrija.

Profesinė veikla:

2013–2015	Laborantas, inžinierius, Vilniaus universitetas, Lazerinių tyrimų centras.
2015–2019	Jaunesnysis mokslo darbuotojas, Vilniaus universitetas, Lazerinių tyrimų centras.

COPIES OF PUBLICATIONS

A1

FILAMENTATION AND LIGHT BULLET FORMATION DYNAMICS IN SOLID-STATE DIELECTRIC MEDIA WITH WEAK, MODERATE AND STRONG ANOMALOUS GROUP VELOCITY DISPERSION

I. Gražulevičiūtė, **N. Garejev**, D. Majus, V. Jukna,
G. Tamošauskas, A. Dubietis

J. Opt. **18**, 025502 (2015)

Reprinted with permission from IOP Publishing

IOP Publishing Journal of Optics
J. Opt. 18 (2016) 025502 (7pp) doi:10.1088/2040-8978/18/2/025502

Filamentation and light bullet formation dynamics in solid-state dielectric media with weak, moderate and strong anomalous group velocity dispersion

I Gražulevičiūtė[1], **N Garejev**[1], **D Majus**[1], **V Jukna**[2], **G Tamošauskas**[1] and **A Dubietis**[1]

[1] Department of Quantum Electronics, Vilnius University, Saulėtekio Avenue 9, Building 3, LT-10222 Vilnius, Lithuania
[2] LOA, ENSTA ParisTech, CNRS, Ecole polytechnique, Université Paris-Saclay, 828 bd des Maréchaux, F-91762 Palaiseau cedex, France

E-mail: audrius.dubietis@ff.vu.lt

Received 3 November 2015, revised 30 November 2015
Accepted for publication 1 December 2015
Published 21 December 2015

Abstract

We present a series of measurements, which characterize filamentation dynamics of intense ultrashort laser pulses in the space–time domain, as captured by means of three-dimensional imaging technique in sapphire and fused silica, in the wavelength range of 1.45–2.25 μm, accessing the regimes of weak, moderate and strong anomalous group velocity dispersion (GVD). In the regime of weak anomalous GVD (at 1.45 μm), pulse splitting into two sub-pulses producing a pair of light bullets with spectrally shifted carrier frequencies in both nonlinear media is observed. In contrast, in the regimes of moderate (at 1.8 μm) and strong (at 2.25 μm) anomalous GVD we observe notably different transient dynamics, which however lead to the formation of a single self-compressed quasistationary light bullet with an universal spatiotemporal shape comprised of an extended ring-shaped periphery and a localized intense core that carries the self-compressed pulse.

Keywords: light bullets, filamentation, anomalous GVD

(Some figures may appear in colour only in the online journal)

1. Introduction

Filamentation of intense femtosecond laser pulses in transparent dielectric media is an universal phenomenon, observed in gases, solids and liquids [1]. The light filament emerges from a collective action of linear (diffraction and dispersion) and nonlinear (self-focusing, self-phase-modulation (SPM), four-wave mixing, multiphoton absorption, ionization and plasma defocusing) effects, whose dynamic interplay produces rich temporal, and more, generally, spatiotemporal dynamics, which in turn gives rise to spectral superbroadening, or supercontinuum generation.

In solid-state dielectric media, the group velocity dispersion (GVD) plays a decisive role in self-focusing and filamentation of ultrashort-pulsed laser beams [2–4]. In the regime of normal GVD, self-focusing is concurrent with pulse front steepening and formation of the optical shocks, and eventually, pulse splitting which occurs at the nonlinear focus [5, 6]. The pulse splitting results in the emergence of distinct leading and trailing sub-pulses, responsible for generation of the red-shifted and blue-shifted spectral components, respectively, which comprise the broadband supercontinuum spectrum [7]. Supercontinuum generation is accompanied by colored conical emission which takes a characteristic X shape in the spectral-angular representation, and in the full spatio-temporal domain the split pulses are interpreted in terms of a pair of spectrally shifted X waves propagating at different group velocities [8]. The pulse splitting and supercontinuum

2040-8978/16/025502+07$33.00

generation processes are tightly connected and reemerge with every subsequent focusing cycle [9].

Although the physical effects governing filamentation in the anomalous GVD regime are basically the same, the reversal of GVD sign has a dramatic impact on the overall filamentation dynamics. In this case it is expected that the self-focusing wave packet should experience simultaneous compression in space and in time, as first suggested by an early work of Silberberg [10], who put forward the concept of spatiotemporal light bullets, which currently attract a considerable attention [11–13]. Indeed, filamentation phenomena in the regime of anomalous GVD were studied numerically [14–16] and more recently verified experimentally, leading to a discovery of a qualitatively new filamentation regime, which produces quasistationary three-dimensional light bullets that preserve a narrow beam diameter and a short pulsewidth over considerable propagation distance in a nonlinear dispersive medium [17–19]. Comprehensive characterization of the light bullets revealed that these objects are polychromatic Bessel-like beams [20] and exhibit peculiar propagation properties in free space, exceptional robustness against various perturbations [21] and maintain stable carrier-envelope phase [22].

Formation of the self-compressed spatiotemporal light bullets facilitates the generation of ultrabroadband supercontinuum whose spectrum spans from the visible to the mid-infrared [23–27]. It is also of great practical importance that the pulse compression down to few optical cycles is achieved under very simple operating conditions, as experimentally demonstrated in various dielectric solid-state media, such as fused silica, sapphire, YAG, CaF_2, and BaF_2 [17, 18, 20, 26, 28], see also [29] for an overview of physical phenomena in the anomalous GVD range. The numerical simulations suggest that such compression method may potentially deliver single optical cycle pulses in the 2–3 μm spectral range [23] and may be scalable to even longer wavelengths and terawatt peak powers [30].

In this paper, we performed an experimental investigation of filamentation dynamics of intense femtosecond laser pulses with center wavelengths of 1.45, 1.8 and 2.25 μm in sapphire and fused silica, which uncovers a remarkably different formation dynamics of spatiotemporal light bullets as a function of the amount of anomalous GVD.

2. Experimental setup

The experiment was performed using broadly tunable (in the 1.2–2.4 μm range) 90–100 fs Gaussian pulses with an energy up to 50 μJ from an optical parametric amplifier (Topas-C, Light Conversion Ltd.), OPA, which was pumped by a fraction of fundamental harmonics of the amplified Ti:sapphire laser system (Spitfire-PRO, Newport-Spectra Physics). A sketch of the experimental setup is depicted in figure 1. The OPA output was suitably attenuated by means of two Glan prisms, which served for isolation and variable attenuation of either signal or idler beams, which thereafter were spatially filtered (not shown) and focused by an $f = +100$ mm lens L1 onto the front face of the nonlinear medium NL. The FWHM dimensions of the spot at the focal plane varied from 40 to 60 μm, depending on the input wavelength.

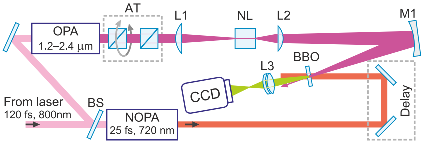

Figure 1. Experimental setup. OPA, optical parametric amplifier; NOPA, noncollinear optical parametric amplifier; AT, variable attenuator for signal/idler pulse selection and energy control; BS, beamsplitter; NL, nonlinear medium; L1, L2, L3, lenses; M1, concave mirror; BBO, beta-barium borate crystal for broadband sum-frequency generation.

The spatiotemporal intensity distribution of the emerging wave packet at the output of the nonlinear medium was measured by means of a three-dimensional imaging technique, based on recording the spatially-resolved cross-correlation function. For that purpose, the output wave-packet was imaged by a 4*f* system (consisting of a lens L2 and a concave mirror M1) onto 20 μm thick beta-barium borate (BBO) crystal cut for type I phase matching, where it was gated with a short, 25 fs pulse with a central wavelength of 720 nm by means of sum-frequency generation, see e.g. [20, 21] for more details. The short gating pulse was produced by a noncollinear optical parametric amplifier (Topas-White, Light Conversion Ltd.), NOPA, which was pumped by the second harmonic of Ti:sapphire laser system. The resulting cross-correlation signal was then imaged by a lens L3 onto the CCD camera (Grasshopper 2, Point Gray). The entire spatiotemporal intensity (x, y, t) distribution of the resulting wave packet was reproduced by merging a series of cross-correlation images recorded by changing the time delay between the object and the gating pulses in an 8 fs step.

The self-focusing dynamics as a function of propagation distance z was captured by using a set of sapphire and fused silica samples of different lengths. In doing so, the samples of the nonlinear medium were placed in such a way that the output face was always kept at the same fixed position (as necessary for imaging), while the position of the focusing lens L1 was adjusted accordingly to ensure the location of the input focal plane on the front face of the sample.

The measurements were performed with three input pulse wavelengths: 1.45, 1.8 and 2.25 μm, which yield different GVD values, as depicted in figure 2, accessing the regimes of weak (close to zero), moderate and strong anomalous GVD, respectively. The energy of the input pulse at the particular wavelength was set so as to exceed the critical power of self-focusing, P_{cr}, by 2.3–4.2 times. The critical power for self-focusing was estimated using an expression $P_{\mathrm{cr}} = 0.15\lambda^2/(n_0 n_2)$, where n_0 and n_2 are linear and nonlinear refractive indexes, respectively. The values of n_2 were taken as 2.9×10^{-16} cm^2 W^{-1} and 2.3×10^{-16} cm^2 W^{-1} for sapphire and fused silica, respectively, neglecting their wavelength dependence, which is assumed to be small in the

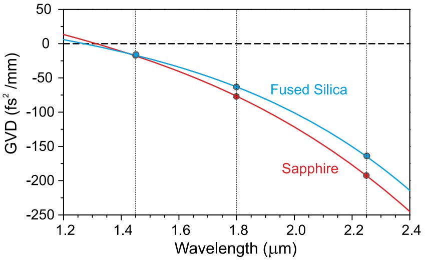

Figure 2. GVD of sapphire (red curve) and fused silica (blue curve) in the 1.2–2.4 μm wavelength range. Full circles denote the GVD values, under which the measurements were performed.

infrared spectral range [31]. The chosen range of the input pulse power guaranteed the position of the nonlinear focus located within few millimeters from the input face of the nonlinear medium and generation of a single filament without additional refocusing cycles. Since the refocusing cycles are generally connected with recurrent pulse splitting events [9, 22], the absence of refocusing cycles was verified by direct measurements of the spatiotemporal intensity profiles, which were performed by changing the propagation length in 2–3 mm step and which do not show any additional pulse splitting events after the light bullet is formed. These observations were also confirmed by the absence of characteristic pulse splitting-induced spectral signatures (intensified blue shift and characteristic modulation) in the visible spectral range [22].

3. Results and discussion

3.1. Weak anomalous GVD regime

The first series of measurements were carried out with the input pulse wavelength of 1.45 μm, which falls just slightly below the zero GVD wavelengths of fused silica (1.27 μm) and sapphire (1.31 μm), as shown in figure 2, and represents the regime of weak anomalous GVD with equal GVD coefficients of -11 fs^2 mm^{-1}. Here we launch the input Gaussian-shaped wave-packet with the FWHM beam diameter of $d_{\text{in}} = 40\ \mu$m, pulsewidth of $\tau_{\text{in}} = 90$ fs and energy of 2.3 μJ, that equates to an input power of 4.1 P_{cr}. Figure 3 shows the resulting spatiotemporal profiles measured in sapphire at various propagation distances z, which illustrate the spatiotemporal transformations at relevant stages of self-focusing. Here and in the following measurements the zero time point was set arbitrarily, at the center of the integrated envelope of the pulse.

The self-action of the input wave packet results in its shrinking in space and slight compression in time due to self-focusing and the interplay between SPM and anomalous GVD, respectively, that take place during the first few millimeters of propagation (not shown). Thereafter, the wave packet undergoes a dramatic transformation at the nonlinear focus, which is located approximately at $z = 4$ mm, as shown in figure 3(a). Here the occurrence of the horizontal lobes in the (x, t) representation attests formation of a Bessel-like beam in the space domain, which develops due to combined action of self-focusing, multiphoton absorption and diffraction [33]. At the same time, the spatial transformation is followed by the pulse splitting in the time domain, producing distinct leading and trailing sub-pulses, which become clearly resolved at further propagation distances, $z = 6$ mm and $z = 15$ mm, as shown in figures 3(b) and (c). More careful inspection of figure 3(c) suggests that the individual sub-pulses acquire peculiar ring-shaped (or so-called, O-shaped) spatiotemporal intensity distributions, as overlaid by bold-dashed curves, which serve as guides for the eye. Notice the logarithmic intensity scale, which is used to highlight fine spatiotemporal features in the periphery of the resulting wave packet.

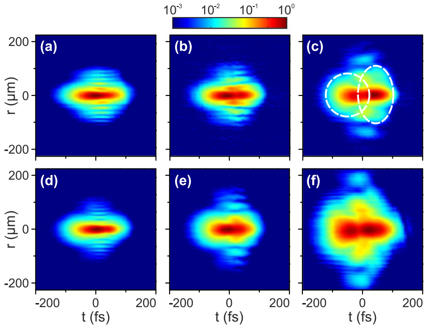

Figure 3. Spatiotemporal intensity profiles of the wave-packet with the center wavelength of 1.45 μm as recorded (top row) in sapphire at (a) $z = 4$ mm, (b) $z = 6$ mm, (c) $z = 15$ and (bottom row) in fused silica at (d) $z = 6$ mm, (e) $z = 10$ mm, (f) $z = 20$ mm.

Figures 3(d)–(f) show the spatiotemporal intensity distributions measured in fused silica with the input pulse energy (power) of 2.4 μJ (2.7 P_{cr}), which confirm a remarkably similar, pulse-splitting-based filamentation scenario: the occurrence of the Bessel-like spatial profile and pulse splitting at the nonlinear focus (figure 3(d)), and finally, the development of characteristic O-shaped spatiotemporal intensity distributions of the individual split sub-pulses with further propagation, which overlap in the space–time domain due to proximity of the split pulses (figures 3(e) and (f)).

The results of the pulse splitting are further presented in figure 4, which shows the cross-correlation functions of the split pulses and the corresponding spectra as measured on the propagation axis at $z = 15$ mm in sapphire and at $z = 20$ mm in fused silica. In both nonlinear media the estimated FWHM durations of the split sub-pulses are the range of 50–60 fs as extracted from deconvolution of the Gaussian fits shown in figures 4 (a) and (c). The corresponding spectra are presented

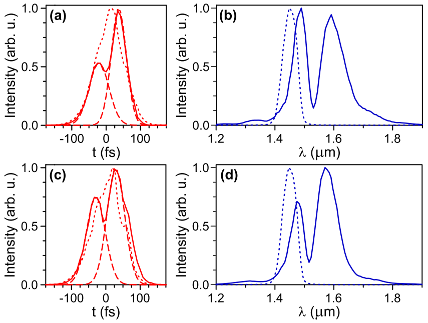

Figure 4. (a), (c) Cross-correlation functions and (b), (d) spectra as recorded after a propagation distance of $z = 15$ mm in sapphire (a), (b) and $z = 20$ mm in fused silica (c), (d). The input pulse and its spectrum are shown by dotted curves; the dashed curves in (a), (c) show the Gaussian fits for the individual sub-pulses.

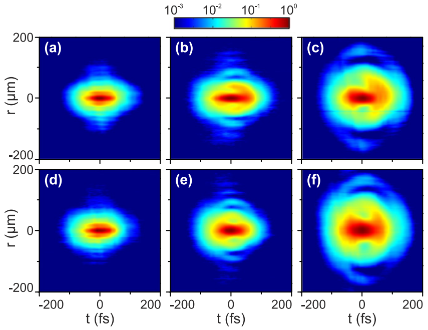

Figure 5. Spatiotemporal intensity profiles of the wave packet with the center wavelength of 1.8 μm as measured (top row) in sapphire at (a) $z = 4$ mm, (b) $z = 8$ mm, (c) $z = 15$ mm and (bottom row) in fused silica at (d) $z = 6$ mm, (e) $z = 10$ mm, (f) $z = 16$ mm.

in figures 4 (b) and (d) and consist of two distinct spectral peaks, which are both red-shifted with respect to the carrier wavelength of the input pulse. The presence of temporally shifted sub-pulses and characteristic double-peaked spectra suggest that the leading and trailing sub-pulses could be associated with the less and more red-shifted spectral peaks, respectively, with account for anomalous GVD. Although direct estimation of the group velocities of the light bullets was not possible with present experimental setup, the apparent red shift of the spectrum may indicate that the light bullets (or, more precisely, their envelope peaks) propagate with subluminal group velocities as compared to the group velocity of the input Gaussian-shaped wave packet. Indeed, subluminal propagation is a distinctive feature of spatiotemporal light bullets in bulk dielectric media with anomalous GVD, as suggested by ample numerical simulations [3, 17, 18], as well as schematically illustrated in [20]. Similar considerations apply also to the results presented in the following sections.

Summarizing these observations, the temporal dynamics with prevailing pulse splitting on the propagation axis in the regime of weak anomalous GVD to some extent is similar to the temporal dynamics observed in the regime of normal GVD, see e.g. [5, 6]. However, the differences occur in the space–time domain, where the individual sub-pulses develop distinct O-shaped spatiotemporal distributions, which allow to interpret them as quasistationary spatiotemporal light bullets, in contrast to the nonlinear X waves with characteristic X-shaped spatiotemporal distributions, as reported in the regime of normal GVD [8].

3.2. Moderate anomalous GVD regime

The second series of experiments were performed with the input pulse wavelength of 1.8 μm which yields the GVD coefficients of -77 fs^2 mm^{-1} in sapphire, and -63 fs^2 mm^{-1} in fused silica, respectively, (see figure 2) and is considered as a regime of moderate anomalous GVD.

Figures 5(a)–(c) present the measured spatiotemporal intensity profiles at relevant propagation lengths in sapphire. Figure 5(a) shows how the input Gaussian wave packet with FWHM beam diameter of $d_{\text{in}} = 45\,\mu$m, pulsewidth of $\tau_{\text{in}} = 90$ fs and energy (power) of 3.1 μJ (3.6 P_{cr}) is reshaped at the nonlinear focus, where it transforms into a Bessel-like beam with a narrow and intense central core, which experiences simultaneous self-compression in time due to opposite action of SPM and the effect of anomalous GVD [17]. With further propagation, the reshaped wave packet smoothly develops a characteristic ring-shaped spatiotemporal profile, as shown figures 5(b) and (c), which represents the stationary solution of the nonlinear Schroedinger equation in nonlinear dissipative media in the anomalous GVD range [32] and which is a distinctive shape of the spatiotemporal light bullet in bulk Kerr medium [20]. The O-shaped spatiotemporal periphery sustains the sub-diffractive and sub-dispersive propagation of the central core, which carries the self-compressed pulse and ensures its robustness against perturbations, as verified by recent experiments reported elsewhere [20–22]. Figures 5(d)–(f) present the results of measurements in fused silica with 3.3 μJ (2.3 P_{cr}) input pulses, which reveal a striking similarity of recorded spatiotemporal intensity profiles, confirming the validity of the above described transformation scenario.

Figure 6 shows the results of pulse self-compression in more detail, by presenting the axial cross-correlation functions as measured in sapphire (at $z = 4$ mm) and in fused silica (at $z = 6$ mm) and their respective spectra. The deconvolution of the cross-correlation functions yields the FWHM durations of the light bullets of 43 and 46 fs in sapphire and fused silica, respectively, indicating twofold compression of the input pulses, as illustrated in figures 6 (a) and (b). On the other hand, the zero-phase Fourier transform

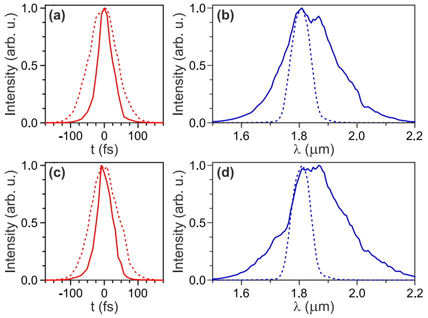

Figure 6. (a), (c) Cross-correlation functions and (b), (d) spectra of the light bullets as recorded at $z = 4$ mm in sapphire (a), (b) and $z = 6$ mm in fused silica (c), (d). Dotted curves show the cross-correlation functions and spectra of the input pulses.

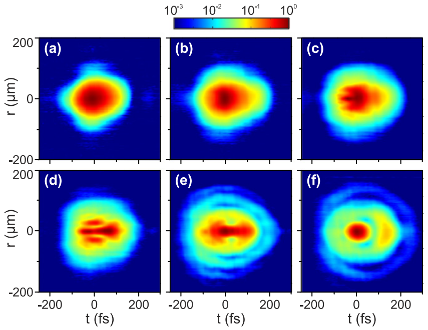

Figure 7. Spatiotemporal intensity profiles of the wave packet with the center wavelength of 2.25 μm as measured at various propagation distances in sapphire: (a) the input Gaussian wave packet at $z = 0$ mm, (b) $z = 4$ mm, (c) $z = 6$ mm, (d) $z = 8$ mm, (e) $z = 12$ and (f) $z = 15$ mm.

of the spectra presented in figures 6 (b) and (d) suggests that the light bullets may be potentially self-compressed down to 20 fs (3.5 optical cycle) duration in both nonlinear media.

3.3. Strong anomalous GVD regime

Strong anomalous GVD regime was accessed by setting the input pulse wavelength at 2.25 μm, which yields the GVD coefficients of $-193\ \mathrm{fs}^2\ \mathrm{mm}^{-1}$ in sapphire and $-165\ \mathrm{fs}^2\ \mathrm{mm}^{-1}$ in fused silica, respectively, see figure 2.

Figure 7 presents the spatiotemporal intensity profiles as measured at various propagation distances in sapphire, showing how the input Gaussian wave-packet with the FWHM beam diameter of $d_{\mathrm{in}} = 61\ \mu$m, pulsewidth of τ_{in}=100 fs and energy (power) of 6.3 μJ (4.2 P_{cr}) (figure 7(a)) transforms into a spatially and temporally compressed three-dimensional light bullet. However, in present case, a peculiar transient spatiotemporal dynamics was observed. Figure 7(b) shows the spatiotemporal intensity profile of the wave packet, as measured at $z = 4$ mm, which indicates a slight self-compression the pulse in time while approaching the nonlinear focus. At the nonlinear focus ($z = 6$ mm) and beyond, the wave packet experiences a dramatic spatiotemporal transformation: the redistribution of its energy in space (formation of a Bessel-like beam) and conditional pulse splitting in time, as shown in figures 7(c) and (d). Eventually, the spatiotemporal transformation of the wave packet ends up with a formation of a characteristic O-shaped spatiotemporal profile at $z = 12$ mm (figure 7(e)), indicating the emergence of a single self-compressed light bullet, which thereafter preserves the acquired spatiotemporal shape during the rest of its propagation, as shown in figure 7(f).

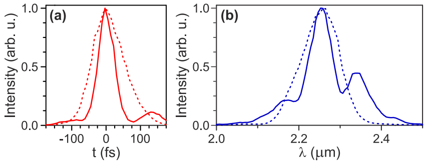

Figure 8. (a) Cross-correlation function and (b) spectrum of the light bullet as recorded after a propagation distance of $z = 15$ mm in sapphire. Dotted curves show the cross-correlation function and spectrum of the input pulse.

Figure 8 presents the axial cross-correlation function and spectrum of the resulting light bullet as recorded at $z = 15$ mm. The measured pulse duration of 48 fs is in good agreement with the transform-limited pulse duration of 45 fs and converts to 6 optical cycles for the input wavelength of 2.25 μm.

The above scenario, which involves conditional pulse splitting, is confirmed by the measurements in fused silica (not shown), suggesting that despite the peculiar transient dynamics the wave packet converges to a single light bullet with an universal O-shaped spatiotemporal intensity profile consisting of an extended ring-shaped periphery and a localized core that carries self-compressed, nearly transform-limited pulse.

4. Conclusions

In conclusion, we carried out an extensive experimental investigation of self-focusing and filamentation of broadly tunable infrared femtosecond light pulses in sapphire and fused silica. The experiments were performed with the input pulse wavelengths of 1.45, 1.8 and 2.25 μm, accessing the regimes of weak, moderate and strong anomalous GVD, respectively. Despite some slight differences in GVD coefficients and nonlinear refractive indexes of sapphire and fused silica, we observed very similar spatiotemporal transformations of the input Gaussian wave-packet in both nonlinear media, while different regimes of anomalous GVD resulted in remarkable differences of the measured spatiotemporal dynamics, whose relevant features are summarized as follows. In the regime of weak anomalous GVD, pulse splitting into two sub-pulses with spectrally-shifted carrier frequencies was observed, while in the space–time domain the individual sub-pulses develop peculiar ring-shaped (or O-shaped) intensity distributions, which allow to interpret them as a pair of three-dimensional light bullets. In contrast, in the regimes of moderate and strong anomalous GVD, we observe formation of a single self-compressed spatiotemporal light bullet. In particular, our measurements uncover that in the regime of moderate anomalous GVD the input Gaussian wave packet smoothly reshapes into a light bullet, whereas strong anomalous GVD results in complex transient spatiotemporal dynamics, which involves conditional pulse splitting beyond the nonlinear focus. Nevertheless, the spatiotemporal intensity distribution of the wave packet eventually converges to a characteristic spatiotemporal shape, comprised of a high intensity central core that carries nearly or almost bandwidth-limited self-compressed pulse and a low-intensity ring-shaped periphery, which is an universal shape of the spatiotemporal (three-dimensional) light bullets in bulk Kerr media with anomalous GVD.

References

[1] Couairon A and Mysyrowicz A 2007 Femtosecond filamentation in transparent media *Phys. Rep.* **441** 47–189

[2] Moll K D and Gaeta A 2004 Role of dispersion in multiple collapse dynamics *Opt. Lett.* **29** 995–7

[3] Skupin S and Bergé L 2006 Self-guiding of femtosecond light pulses in condensed media: plasma generation versus chromatic dispersion *Physica* D **220** 14–30

[4] Faccio D *et al* 2008 Few-cycle laser-pulse collapse in Kerr media: the role of group-velocity dispersion and X-wave formation *Phys. Rev.* A **78** 033826

[5] Ranka J K, Schirmer R W and Gaeta A L 1996 Observation of pulse splitting in nonlinear dispersive media *Phys. Rev. Lett.* **77** 3783–6

[6] Gaeta A L 2000 Catastrophic collapse of ultrashort pulses *Phys. Rev. Lett.* **84** 3582–5

[7] Gaeta A L 2009 Spatial and temporal dynamics of collapsing ultrashort laser pulses *Top. Appl. Phys.* **114** 399–411

[8] Faccio D, Porras M A, Dubietis A, Bragheri F, Couairon A and Di Trapani P 2006 Conical emission, pulse splitting, and X-wave parametric amplification in nonlinear dynamics of ultrashort light pulses *Phys. Rev. Lett.* **96** 193901

[9] Jarnac A, Tamošauskas G, Majus D, Houard A, Mysyrowicz A, Couairon A and Dubietis A 2014 Whole life cycle of femtosecond ultraviolet filaments in water *Phys. Rev.* A **89** 033809

[10] Silberberg Y 1990 Collapse of optical pulses *Opt. Lett.* **15** 1282–4

[11] Malomed B A, Mihalache D, Wise F and Torner L 2005 Spatiotemporal optical solitons *J. Opt.* B **7** R53–72

[12] Mihalache D 2012 Linear and nonlinear light bullets: recent theoretical and experimental studies *Rom. J. Phys.* **57** 352–71

[13] Frantzeskakis D J, Leblond H and Mihalache D 2014 Nonlinear optics of intense few-cycle pulses: an overview of recent theoretical and experimental developments *Rom. J. Phys.* **59** 767–84

[14] Bergé L and Skupin S 2005 Self-channeling of ultrashort laser pulses in materials with anomalous dispersion *Phys. Rev.* E **71** 065601R

[15] Liu J, Li R and Xu Z 2006 Few-cycle spatiotemporal soliton wave excited by filamentation of a femtosecond laser pulse in materials with anomalous dispersion *Phys. Rev.* A **74** 043801

[16] Chekalin S V, Kompanets V O, Smetanina E O and Kandidov V P 2013 Light bullets and supercontinuum spectrum during femtosecond pulse filamentation under conditions of anomalous group-velocity dispersion in fused silica *Quantum Electron.* **43** 326–31

[17] Durand M, Jarnac A, Houard A, Liu Y, Grabielle S, Forget N, Durécu A, Couairon A and Mysyrowicz A 2013 Self-guided propagation of ultrashort laser pulses in the anomalous dispersion region of transparent solids: a new regime of filamentation *Phys. Rev. Lett.* **110** 115003

[18] Smetanina E O, Kompanets V O, Dormidonov A E, Chekalin S V and Kandidov V P 2013 Light bullets from near-IR filament in fused silica *Laser Phys. Lett.* **10** 105401

[19] Chekalin S V, Dokukina A E, Dormidonov A E, Kompanets V O, Smetanina E O and Kandidov V P 2015 Light bullets from a femtosecond filament *J. Phys. B: At. Mol. Opt. Phys.* **48** 094008

[20] Majus D, Tamošauskas G, Gražulevičiūtė I, Garejev N, Lotti A, Couairon A, Faccio D and Dubietis A 2014 Nature of spatiotemporal light bullets in bulk Kerr media *Phys. Rev. Lett.* **112** 193901

[21] Gražulevičiūtė I, Tamošauskas G, Jukna V, Couairon A, Faccio D and Dubietis A 2014 Self-reconstructing spatiotemporal light bullets *Opt. Express* **22** 30613–22

[22] Gražulevičiūtė I, Šuminas R, Tamošauskas G, Couairon A and Dubietis A 2015 Carrier-envelope phase-stable spatiotemporal light bullets *Opt. Lett.* **40** 3719–22

[23] Silva F, Austin D R, Thai A, Baudisch M, Hemmer M, Faccio D, Couairon A and Biegert J 2012 Multi-octave supercontinuum generation from mid-infrared filamentation in a bulk crystal *Nat. Commun.* **3** 807

[24] Darginavičius J, Majus D, Jukna V, Garejev N, Valiulis G, Couairon A and Dubietis A 2013 Ultrabroadband supercontinuum and third-harmonic generation in bulk solids with two optical-cycle carrier-envelope phase-stable pulses at 2 μm *Opt. Express* **21** 25210–20

[25] Dharmadhikari J A, Deshpande R A, Nath A, Dota K, Mathur D and Dharmadhikari A K 2014 Effect of group velocity dispersion on supercontinuum generation and filamentation in transparent solids *Appl. Phys.* B **117** 471–9

[26] Liang H, Krogen P, Grynko R, Novak O, Chang C-L, Stein G J, Weerawarne D, Shim B, Kärtner F X and Hong K-H 2015 Three-octave-spanning supercontinuum generation and sub-two-cycle self-compression of mid-infrared filaments in dielectrics *Opt. Lett.* **40** 1069–72

[27] Chekalin S V, Kompanets V O, Dokukina A E, Dormidonov A E, Smetanina E O and Kandidov V P 2015 Visible supercontinuum radiation of light bullets in the femtosecond filamentation of IR pulses in fused silica *Quantum Electron.* **45** 401–7

[28] Hemmer M, Baudisch M, Thai A, Couairon A and Biegert J 2013 Self-compression to sub-3-cycle duration of mid-infrared optical pulses in dielectrics *Opt. Express* **21** 28095–102

[29] Couairon A *et al* 2016 Filamentation and pulse self-compression in the anomalous dispersion region of glasses *Laser Filamentation* (*CRM Series in Mathematical Physics*) ed A D Bandrauk *et al* (Berlin: Springer) pp 147–165

[30] Bravy B G, Gordienko V M and Platonenko V T 2015 Kerr effect-assisted self-compression in dielectric to single-cycle pulse width and to terawatt power level in mid-IR *Opt. Commun.* **344** 7–11

[31] Major A, Yoshino F, Nikolakakos I, Aitchison J S and Smith P W E 2004 Dispersion of the nonlinear refractive index in sapphire *Opt. Lett.* **29** 602–4

[32] Porras M A, Parola A and Di Trapani P 2005 Nonlinear unbalanced O waves: nonsolitary, conical light bullets in nonlinear dissipative media *J. Opt. Soc. Am.* B **22** 1406–13

[33] Dubietis A, Gaižauskas E, Tamošauskas G and Di Trapani P 2004 Light filaments without self-channeling *Phys. Rev. Lett.* **92** 253903

A2

ROLE OF EXTERNAL FOCUSING GEOMETRY IN SUPERCONTINUUM GENERATION IN BULK SOLID-STATE MEDIA

V. Jukna, **N. Garejev**, G. Tamošauskas, A. Dubietis

J. Opt. Soc. Am. B **36**, A54–A60 (2019)

Preprint version reprinted

The role of external focusing geometry in supercontinuum generation in bulk solid-state media

VYTAUTAS JUKNA,[*] NAIL GAREJEV, GINTARAS TAMOŠAUSKAS AND AUDRIUS DUBIETIS

Laser Research Center, Vilnius University, Saulėtekio Avenue 10, LT-10223 Vilnius, Lithuania
[*]*vytautas.jukna@ff.vu.lt*

Abstract: We present a detailed experimental and numerical study of supercontinuum generation in sapphire crystal at the vicinity of its zero group velocity dispersion point (1.3 μm) when pumped by relatively long (210 fs) femtosecond pulses. We uncover very different evolutions of the spectral broadening versus the input pulse energy when the incident beam is focused either onto the input face or inside 4 mm-thick sapphire sample. In particular, when the input beam was focused inside the crystal, we captured a surprising variation of the spectral width as a function of the input pulse energy, demonstrating supercontinuum generation, its suppression and eventually, its recovery. The experimental findings were nicely reproduced by the numerical simulations, revealing a specific supercontinuum generation scenario, which relies on strong reshaping of the wave packet due to defocusing and absorption of free electron plasma, subsequent replenishment of the pulse on the propagation axis and its splitting. We also demonstrate that this particular supercontinuum generation scenario takes place regardless of the external focusing geometry.

1. Introduction

Supercontinuum (SC) generation with femtosecond laser pulses in bulk dielectric media represents a compact, efficient and robust technique for the generation of coherent broadband radiation at various parts of the optical spectrum, finding diverse applications in the fields of time-resolved spectroscopy, ultrafast nonlinear optics and photonics [1]. Extensive studies on the subject in the past revealed that the ratio of the incident photon energy and the material bandgap [2, 3], and the chromatic dispersion [4] are the key physical factors that define the spectral extent of the SC and hence the choice of feasible nonlinear materials. In addition to these, the universal practical issues, such as proper selection of the numerical aperture avoiding the optical damage of the medium [5, 6] and accessing the largest red-shifted spectral broadening [7, 8] have been experimentally established since.

SC generation in transparent bulk medium stems from the nonlinear propagation of intense ultrashort laser pulse that is governed by an interplay between linear (dispersion and diffraction) and nonlinear (self-focusing, self-phase modulation, multiphoton absorption /ionization, generation of free electron plasma, etc.) effects that become coupled in spatial and temporal domains. This leads to a complex physical picture that is fairly well understood in the framework of femtosecond filamentation [9]. Temporal filamentation scenarios are defined by the sign of the group velocity dispersion (GVD) of the nonlinear material: pulse splitting in the range of normal and around zero GVD, and pulse self-compression in the range of anomalous GVD, which produce spectral broadenings of quite different scales. To this end, considerably broader SC spectra were produced in various nonlinear media pumping at the vicinity of their zero GVD [10–12], as compared to SC spectra generated in the range of normal GVD, see [1] for a review. Eventually, ultrabroadband, multi-octave SC spectra were generated with ultrashort mid-infrared pulses, whose wavelengths fall into the range of anomalous GVD of transparent materials [13–19].

A typical SC generation setup considers external focusing of the input beam in that way so as the beam waist is located on the front face of the nonlinear medium. However, other focusing geometries could be applied, although these have received much less attention so far. In that regard, several studies revealed that the SC spectral width, and the blue-shifted spectral broadening in particular, is very critical to the position of the nonlinear medium with respect to the geometric focus of an external focusing lens, as demonstrated with convergent and divergent pump beams in fused silica [20] and more recently, in water [21], in the ranges of normal and anomalous GVD, respectively. An unexpected spectral evolution versus the input pulse energy was recorded when focusing the input beam inside fused silica and YAG samples, demonstrating considerable shrinking of the entire SC spectrum while increasing the input pulse energy [17].

In this paper we address the role of external focusing geometry in the dynamics of spectral broadening and supercontinuum generation in sapphire, as is produced by filamentation of 210 fs pulses with the central wavelength at 1.3 μm that matches the zero GVD point of the crystal. The experimental results demonstrate that focusing of the pump beam either on the input face or inside the crystal results in remarkably different spectral evolutions as functions of the input pulse energy. The experimental data were nicely reproduced by the numerical simulations, which revealed that filamentation dynamics of these relatively long femtosecond pulses is governed by the effects of free electron plasma, sharing many common features with filamentation of picosecond pulses.

2. Experimental results

The experiment was performed using a commercial optical parametric amplifier (Topas-Prime, Light Conversion Ltd., OPA), pumped by an amplified Ti:sapphire laser system (Spitfire-PRO, Newport-Spectra Physics). The signal pulse from OPA with a central wavelength of 1.3 μm was suitably attenuated and transmitted through an interference filter (9 nm bandwidth) so as to intentionally increase its duration from 100 fs to 210 fs without chirping and preserving its initial time-bandwidth product as verified by measuring the autocorrelation function. The stretched pulse had an energy up to 6 μJ and served to produce a single filament in a 4 mm-thick sapphire crystal. In doing so, the pump beam was focused by a $f = +100$ mm lens, yielding FWHM spot size of 23 μm at the focal plane. The measurements were performed in two different external focusing geometries. In the first one, the input face of the sapphire sample was located exactly at the focal plane of the focusing lens; in the second one, the sapphire sample was moved closer to the focusing lens, so the geometric focus being located 1 mm inside the crystal.

The input pulse energy was varied using a neutral metal-coated gradient filter (NDL-25C-2, Thorlabs Inc.). High dynamic range spectral measurements were performed with a home-built scanning spectrometer with Si and Ge detectors, operating in the $0.2 - 1.1$ μm and $0.4 - 1.8$ μm spectral ranges, respectively. The SC spectra were collected into the slit of the spectrometer using a pair of Al-coated concave mirrors. The estimated angular acceptance of the spectrometer was ± 50 mrad from the beam propagation axis, so capturing the on-axis part of the SC and only a fraction of the conical emission. The measured spectra were corrected to sensitivity functions of the detectors and transmission of the bandpass optical filters used to attenuate the most intense part of the spectrum around the pump wavelength. The spectra measured with each detector were slightly scaled to achieve consistency in the overlap region. In addition to spectral measurements, we monitored the luminescence tracks in the crystal volume, which indicated filament formation and the position of the nonlinear focus. The luminescence tracks were photographed using a digital camera with a Bayer filter (Nikon D7200, 3.92 μm pixel pitch).

Figure 1(a) presents the spectral evolution versus the input pulse energy in the case when the geometric focus of the input beam was located exactly at the input face of sapphire sample. An explosive spectral broadening is observed as the input pulse energy reaches a certain threshold value (2 μJ). Thereafter, as the pump energy increases, the SC spectral width remains fairly

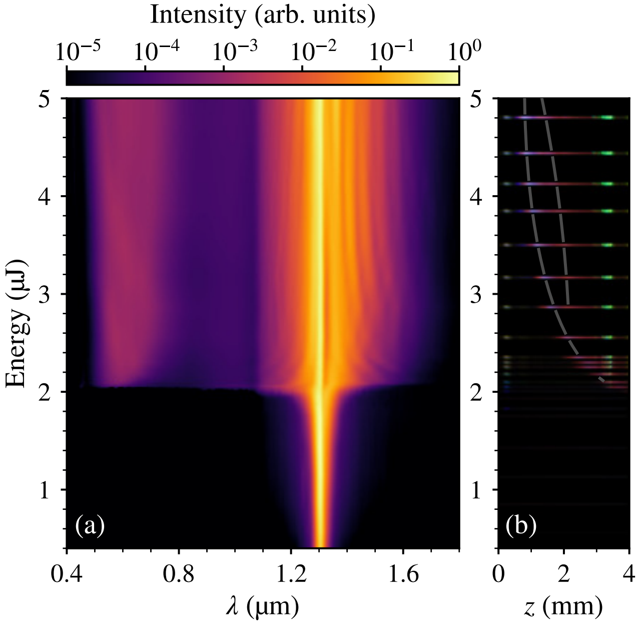

Fig. 1. (a) Spectral evolution versus the input pulse energy as measured with 210 fs, 1.3 μm input pulses, focusing the beam onto the input face of 4 mm-long sapphire sample. (b) Composite image of the luminescence traces inside the crystal. Gray curves indicate the positions of the local luminescence maxima. z denotes the propagation distance, where $z = 0$ mm and $z = 4$ mm correspond to the input and output faces of the crystal, respectively.

constant, extending from 470 nm to 1.8 μm (at the 10^{-5} intensity level). This case constitutes a typical dynamics of the spectral broadening, as observed in other nonlinear media and/or with other incident wavelengths, see e.g. [22, 23].

Fig. 1(b) illustrates the corresponding luminescence traces, as captured from a side view of the crystal. Crystal luminescence readily serves for monitoring the filament formation dynamics in various solid state materials [24], while its spectral analysis provides information on the energy deposition to the crystal lattice, dopants and impurities [25]. In the present case, luminescence of sapphire originates from the 11 photon absorption, assuming its bandgap of 9.9 eV and photon energy of 0.95 eV. Sapphire produces a broad luminescence band which peaks at 325 nm, as verified by measuring the luminescence spectrum with a fiber spectrometer (not shown here), which is possibly attributed to the formation of F^+ centers, see e.g. [26]. Its long-wave tail extends into the visible range and is perceived by a naked eye (and the photocamera) as a distinct violet emission. The intense green spot is attributed to a parasitic reflection of the SC light that is produced by scattering at the output face of the crystal. The most intense part of the luminescence trace indicates the highest intensity and hence the position of the nonlinear focus: notice how the nonlinear focus shifts from the output face toward the input face of the crystal as the input pulse energy is increased. Interestingly, for the input pulse energies > 2.6 μJ, the luminescence trace shows a fainter but distinct secondary maximum. The gray curves in Fig. 1(b) highlight the positions of the main and secondary maxima of the luminescence trace, serving as guides for the eye.

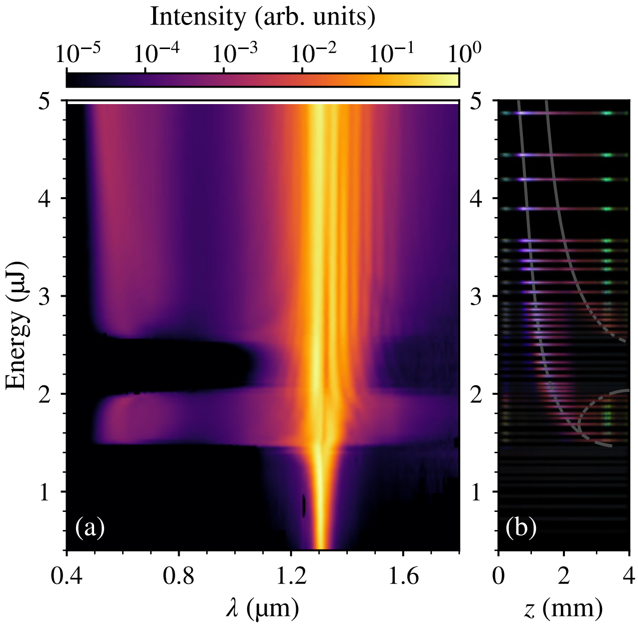

Fig. 2. The same as in Fig. 1, but the input beam is focused 1 mm inside the sapphire sample.

A surprising spectral evolution, as shown in Fig. 2(a), was recorded in the second case, when the input beam was focused 1 mm inside the sapphire sample. First of all, the threshold energy for SC generation (1.48 μJ) was found to be lower by 25% as compared with the above case. However, with further increase of the input pulse energy, a complete suppression of SC generation is observed in the $2.0 - 2.5$ μJ input energy interval. Thereafter, for the input pulse energies above 2.5 μJ, the SC generation is recovered and further behaves in a similar fashion as described in the case illustrated in Fig. 1(a). Notice an abrupt character of the switching from SC generation to its suppression and from the suppression to its recovery in terms of the input pulse energy. More detailed spectra associated with SC generation, suppression and recovery are presented in Fig. 3.

Interestingly, in the input pulse energy range where SC generation is suppressed, the nonlinear focus is still inside the crystal, as indicated by the position of the main luminescence maximum, which continuously shifts toward the input face of the crystal with increasing the energy, as illustrated in Fig. 2(b). Notice that the absence of the SC is also apparently indicated by the absence of the parasitic green light due to scattering from the output face of the crystal. However, the trajectory of the secondary (fainter) luminescence maximum suggests a remarkably different dynamics versus the input pulse energy. First of all, just above the threshold energy for SC generation, the position of the secondary luminescence maximum continuously shifts toward the output face of the crystal, as the input pulse energy is increased, and eventually disappears. Thereafter, with further increase of the input pulse energy, the secondary maximum reappears at the output face and then moves toward the input face of the crystal. A comparison of Figs. 2(a) and 2(b) is very illustrative: the disappearance of the secondary maximum coincides with the suppression, while its reappearance coincides with the recovery of SC generation, suggesting rather unusual scenario of SC generation.

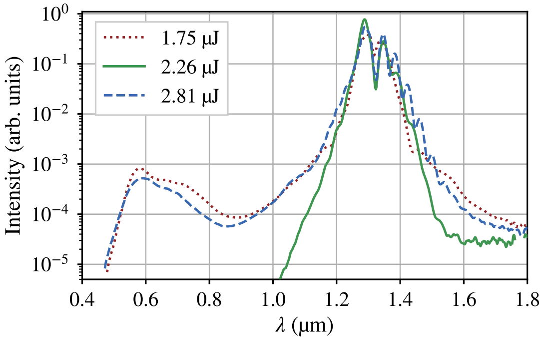

Fig. 3. Comparison of the SC spectra generated with different input pulse energies in the case when the input beam was focused inside the sapphire sample.

3. Numerical simulations

In order to get further insights into these surprising experimental findings, we performed the numerical simulations by solving unidirectional nonparaxial propagation equation for the pulse envelope $\hat{E}(\omega, k_\perp, z)$ [27]:

$$\frac{\partial \hat{E}}{\partial z} = i\left(\sqrt{k^2(\omega) - k_\perp^2} - k_0 - k_0'\omega\right)\hat{E} + \tag{1}$$

$$i\frac{\omega}{2n(\omega)c}\epsilon_0^{-1}\left(\hat{P} + i\frac{\hat{J}}{\omega}\right), \tag{2}$$

where c is the speed of light in a vacuum, ϵ_0 is the vacuum permittivity, $k(\omega)$ denotes the dispersion relation of the medium, $k_\perp$ is the transverse wave vector, $n(\omega)$ is the refractive index of the medium calculated from a Sellmeier equation [28], from which $k_0 \equiv k(\omega_0)$ and $k_0' \equiv dk/d\omega|_{\omega_0}$ were evaluated at the central laser frequency ω_0. The nonlinear polarization $P(t, r, z)$ and current source $J(t, r, z)$ terms were computed in the space-time domain, assuming revolution symmetry:

$$\epsilon_0^{-1}P = 2n_0 n_2 |E|^2 E, \tag{3}$$

$$\epsilon_0^{-1}J = n_0 c\left[\sigma(1 + i\omega_0\tau_c)\rho + \frac{WU_g}{|E|^2}\left(1 - \frac{\rho}{\rho_{nt}}\right)\right]E, \tag{4}$$

where $n_0 = 1.75$ and $n_2 = 3.1 \times 10^{-16}$ cm^2/W [29] are the linear and nonlinear refractive indexes of sapphire, respectively, $\sigma = 1.9 \times 10^{-21}$ m^2 is the cross section for inverse Bremsstrahlung, $\tau_c = 1$ fs is the effective electron collision time, $\rho_{nt} = 2.35 \times 10^{22}$ cm^{-3} is the density of neutral molecules, and ρ is the density of free electrons in the conduction band. The intensity dependent photoionization rate W was calculated from Keldysh's theory with electron-hole mass ratio $m^* = 1$ and assuming band gap of sapphire $U_g = 9.9$ eV [28]. Free electron generation was simulated using a rate equation describing the evolution of the density of electrons in the conduction band:

$$\frac{\partial \rho}{\partial t} = W(1 - \frac{\rho}{\rho_{nt}}) + \frac{\sigma}{U_g}|E|^2\rho(1 - \frac{\rho}{\rho_{nt}}) - \frac{\rho}{\tau_{rec}}, \tag{5}$$

where the terms on the right hand side stand for photoionization, avalanche ionization and recombination, respectively, where τ_{rec} = 100 ps [30] is the free electron recombination time.

The simulations were performed using the input pulse duration of 210 fs and FWHM diameter of the input Gaussian beam of 30 μm, assuming a flat phase front which is produced at the beam waist (focal plane of the external focusing lens). In the case of focusing inside the sample, the diameter and wave front curvature of the input beam was adjusted accordingly, by simulating back propagation of the beam from its focal plane in the air.

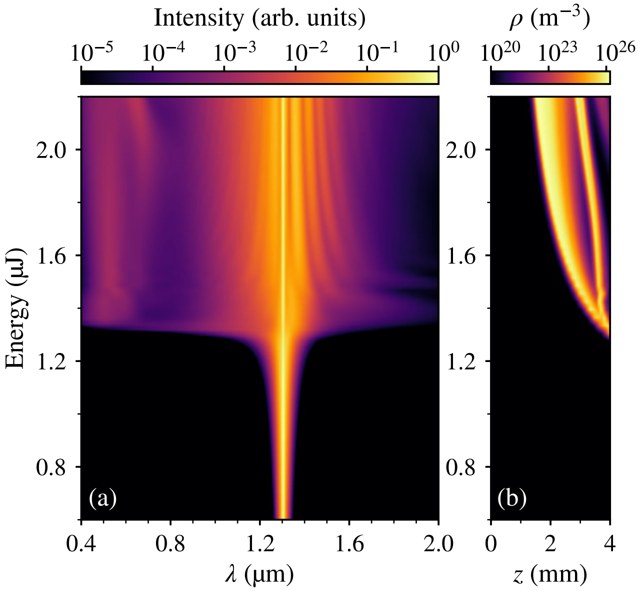

Fig. 4. (a) Numerically simulated spectral evolution versus the input pulse energy, in the case when the input beam is focused onto the input face of the sapphire sample. (b) Evolution of free electron plasma density inside the crystal.

Figures 4 and 5 show the numerically simulated evolutions of the spectrum and free electron plasma density in both cases of external focusing. The numerical results nicely reproduce the essential features of the experimentally measured dynamics of the spectral broadening and free electron plasma densities inside the sample, which are proportional to the filament-induced luminescence intensities. Remarkably, the evolutions of the secondary peaks of free electron plasma densities inside the sample reproduce the experimentally recorded variations of the luminescence traces in great detail. A slight difference in the numerical and experimental threshold energies for SC generation could be explained by the fact that relevant material parameters are known with a limited accuracy and in part due to non-ideality of the experimental pulse and beam shapes.

4. Discussion

In order to unveil the physical mechanism which lies behind the suppression and recovery of SC generation, in Fig. 6 we present the numerically simulated evolutions of the input Gaussian wave packet in the spatial, temporal and spectral domains. The numerical input pulse energies of 1.18 μJ (left column), 1.39 μJ (middle column) and 1.73 μJ (right column) were chosen to

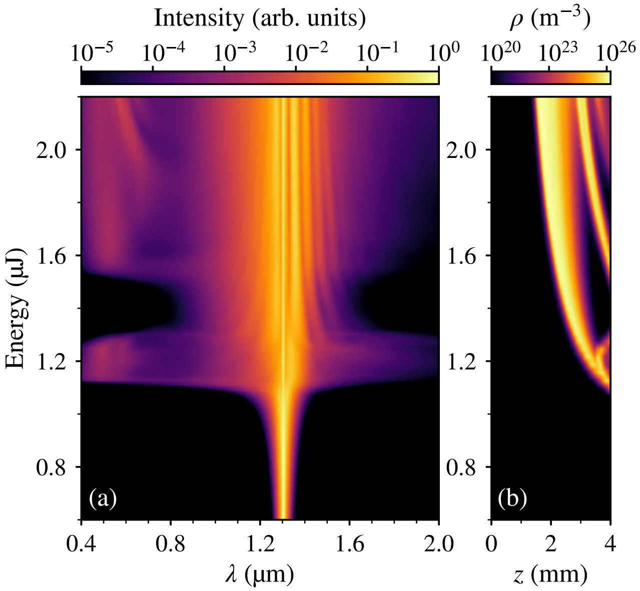

Fig. 5. The same as in Fig. 4, but the input beam is focused 1 mm inside the sapphire sample.

represent the particular cases of SC generation, suppression and recovery, respectively. The top row in Fig. 6 shows the dynamics of the beam versus the propagation distance, where dashed curves show the evolutions of the beam HWHM (half-width at half-maximum) radius. The middle row represents the dynamics of the pulse intensity profile in the center of the beam (on the propagation axis), where dashed curves indicate the positions of the maximum intensity. The bottom row shows the corresponding evolutions of the spectra.

The case of the input pulse energy of 1.18 μJ (left column of Fig. 6) to the simplest approximation represents a *nearly* typical scenario of the SC generation: an explosive spectral broadening [SC generation, Fig. 6(g)] is produced at the position of the nonlinear focus ($z \approx 3.5$ mm, Fig. 6(a)), where the pulse splitting occurs [Fig. 6(d)].

The middle column of Fig. 6 (the input pulse energy 1.39 μJ) represents the case of SC suppression. Although the beam dynamics shown in Fig. 6(b) looks quite similar to the previous case, just with the nonlinear focus being slightly shifted toward the input face of the sample, the temporal evolution of the pulse appears quite different, as illustrated in Fig. 6(e). No pulse splitting is observed at the position of the nonlinear focus. In contrast, the pulse on the propagation axis experiences a considerable reduction of its width due to absorption and defocusing of free electron plasma, whose collective effect pushes a large fraction of the pulse energy out of the propagation axis and so gradually shifts the intensity peak to the front of the pulse. Such pulse shortening produces only a moderate spectral broadening at the nonlinear focus, but no SC generation, as illustrated in the middle row of Fig. 6

The right column of Fig. 6 demonstrates the spatial, temporal and spectral dynamics as produced by the input pulse with an energy 1.73 μJ, which refer to the case of recovery of SC generation. The recovery of SC generation is clearly linked with the replenishment of the pulse on the propagation axis, its refocusing and eventually, splitting. The reoccurrence of the pulse on the propagation axis results from inward energy flow of the defocused portion of the wave

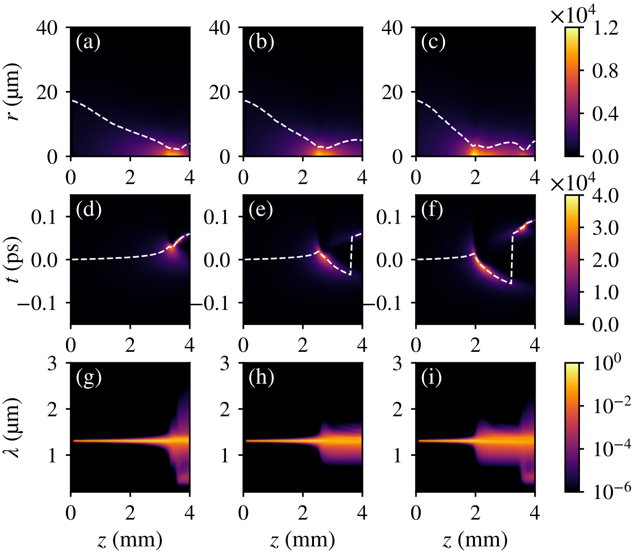

Fig. 6. Numerically simulated dynamics of the beam fluence (top row), pulse on the propagation axis (middle row) and spectrum (bottom row), which represent the cases of SC generation, suppression and recovery, from left to right, respectively, in the case when the input beam is focused inside the sapphire sample. The dashed curves in the top row show the evolution of the beam HWHM radius, while these in the middle row show the temporal location of the local intensity maximum.

packet, in accordance with the scenario of the so-called dynamic spatial replenishment [31]. The spatial, temporal and spectral dynamics, especially those depicted in the middle and right columns of Fig. 6, suggest that SC generation scenario with relatively long femtosecond pulses is markedly different from a typical SC generation scenario with 100 fs and shorter pulses in the range of normal and zero GVD, which relies on the pulse splitting at the nonlinear focus, where SC is produced via pulse front steepening of the split pulses [32]. Moreover, according to this scenario, filament refocusing produces yet another pulse splitting event at the secondary nonlinear focus, yielding another boost of SC generation and resulting in periodic modulation of the SC spectrum due to interference between the primary and the secondary split pulses. Such SC generation scenario is universal, and applies to virtually any nonlinear medium with 100 fs and shorter pump pulses in the range of normal and zero GVD, see e.g. [1,8,33]. In contrast, the uncovered sequence of spatiotemporal transformations in the present case is fairly reminiscent to filamentation dynamics of picosecond laser pulses, where the initial stage of the self-focusing is governed by free electron plasma [34]. A remarkable feature of this filamentation regime is plasma-driven self-shortening of the pulse via absorption and defocusing of its trailing part at the (first) nonlinear focus, which results only in a moderate spectral broadening but not SC generation. The SC is produced only later on, at the secondary nonlinear focus by the splitting of the replenished pulse.

The latter scenario is justified in Fig. 7, which compares the dynamics of relevant parameters on the propagation axis: beam radius, peak intensity and density of free electron plasma and brings additional instructive details on filamentation and SC generation with 210 fs input pulses. In all three cases of interest, the first intensity peak occurs at the position of the nonlinear

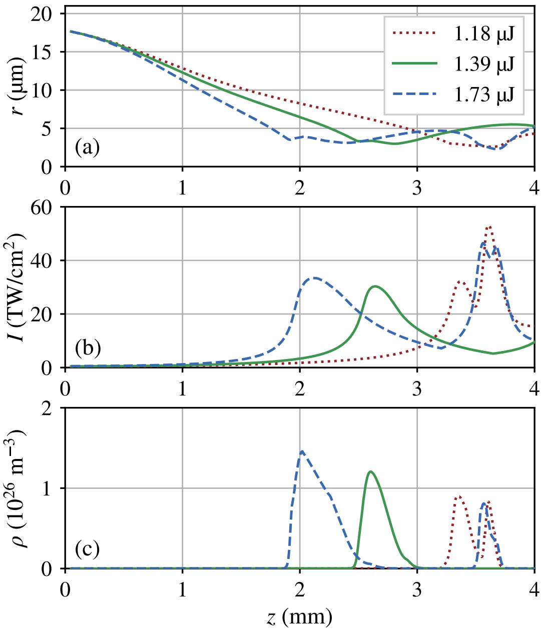

Fig. 7. Comparison of the numerically simulated evolutions of (a) beam FWHM radius, (b) peak intensity, (c) density of free electron plasma.

focus, which is manifested by the smallest beam radius, and produces the largest density of free electron plasma, which is associated with the first luminescence maximum that is observed in the experiment. The occurrence of the secondary intensity peak originates from refocusing of the replenished pulse, which produces a secondary plasma peak and so the secondary fainter maximum of luminescence. The position of the refocusing is defined by the input pulse energy and peak density of the generated plasma: the increase of the input pulse energy not only shifts the position of the first nonlinear focus closer to the input face of the sample, but also yields higher density of free electron plasma, which defines the length scale where pulse replenishment, refocusing and eventually, pulse splitting occurs. In the case of the lowest input pulse energy (1.18 μJ), the pulse is replenished and refocused very quickly, as manifested by close positions of the main and secondary intensity and plasma density peaks. In the case of the highest input pulse energy (1.73 μJ), the separation of pulse reshaping, replenishment and refocusing phases is much larger. In the case of the input pulse energy (1.39 μJ), which corresponds to a peculiar case of the SC suppression, the pulse replenishment and refocusing take place virtually outside the crystal, as the crystal is too short.

A very similar filamentation and SC generation scenario applies also to the case when the input beam is focused onto the input face of the sample, where the phases of pulse reshaping, replenishment and splitting are separated by a smaller propagation distance and thus are brought to a more compact length scale. Hence the refocusing and splitting of the replenished pulse always takes place inside the crystal, as indicated by the presence of distinct secondary maxima in the experimentally recorded luminescence traces, as shown in Fig. 1(b) and by secondary peaks of plasma density in the numerical simulations, as shown in Fig. 4(b). Therefore in the case of relatively long femtosecond pulses, the SC generation scenario is rather specific: SC is *always* generated by refocusing and subsequent splitting of the replenished pulse. The external focusing geometry and the input pulse energy are the parameters which define only the propagation length after which the replenished pulse is able to refocus.

5. Conclusions

In conclusion, we experimentally and numerically studied spectral evolutions of SC generation versus the input pulse energy, as induced by filamentation of 210 fs, 1.3 μm pulses in sapphire, at its zero GVD point. We found that external focusing of the input beam either onto the input face or inside the crystal sample produces a surprisingly different dynamics of the spectral broadening. In the configuration where the geometrical focus of the input beam is located inside the crystal, the energy threshold for SC generation is reduced by 25%, however the SC spectral width experiences a dramatic variation on the input pulse energy. In particular, after the SC is generated, further increase of the input energy leads to an almost complete suppression and afterwards a recovery of the SC generation. That switching on and off the SC generation has an almost abrupt character in terms of the input pulse energy.

The experimental observations were backed-up by the numerical simulations, which reproduced in detail the spectral evolutions in both cases of external focusing. The interpretation of the numerical data uncovers the SC generation scenario, which is markedly different from that of short (~100 fs and shorter) pulses and shares the basic features of filamentation scenario with picosecond laser pulses. More specifically, we demonstrate that relatively long femtosecond pulses undergo strong reshaping of the wave packet due to defocusing and absorption of free electron plasma, subsequent replenishment of the pulse on the propagation axis and its splitting, which produces SC. We assume that the uncovered SC generation scenario is universal and holds for filamentation of the pulses whose durations are in the range from few-100 fs to sub-picosecond and whose carrier wavelengths fall into the range of normal and zero GVD of the nonlinear medium. We believe that these findings are important from a practical viewpoint, and could be considered for optimization of various SC generation schemes, where SC is produced by relatively long femtosecond pulses delivered by recently developed Yb:KGW, Yb:KYW, Yb:fiber and similar laser systems.

References

1. A. Dubietis, G. Tamošauskas, R. Šuminas, V. Jukna, and A. Couairon, “Ultrafast supercontinuum generation in bulk condensed media,” Lith. J. Phys. **57**, 113–157 (2017).
2. A. Brodeur and S. L. Chin, “Band-gap dependence of the ultrafast white-light continuum,” Phys. Rev. Lett. **80**, 4406–4409 (1998).
3. A. Brodeur and S. L. Chin, “Ultrafast white-light continuum generation and self-focusing in transparent condensed media,” J. Opt. Soc. Am. B **16**, 637–650 (1999).
4. M. Kolesik, G. Katona, J. V. Moloney, and E. M. Wright, “Physical factors limiting the spectral extent and band gap dependence of supercontinuum generation,” Phys. Rev. Lett. **91**, 043905 (2003).
5. N. T. Nguyen, A. Saliminia, W. Liu, S. L. Chin, and R. Valée, “Optical breakdown versus filamentation in fused silica by use of femtosecond infrared laser pulses,” Opt. Lett. **28**, 1591–1593 (2003).
6. J. B. Ashcom, R. R. Gattass, C. B. Schaffer, and E. Mazur, “Numerical aperture dependence of damage and supercontinuum generation from femtosecond laser pulses in bulk fused silica,” J. Opt. Soc. Am. B **23**, 2317–2322 (2006).
7. M. Bradler, P. Baum, and E. Riedle, “Femtosecond continuum generation in bulk laser host materials with sub-μJ pump pulses,” Appl. Phys. B **97**, 561–574 (2009).
8. V. Jukna, J. Galinis, G. Tamošauskas, D. Majus, and A. Dubietis, “Infrared extension of femtosecond supercontinuum generated by filamentation in solid-state media,” Appl. Phys. B **116**, 477–483 (2014).
9. A. Couairon and A. Mysyrowicz, “Femtosecond filamentation in transparent media,” Phys. Rep. **441**, 47–190 (2007).
10. A. Saliminia, S. L. Chin, and R. Vallée, “Ultra-broad and coherent white light generation in silica glass by focused femtosecond pulses at 1.5 μm,” Opt. Express **13**, 5731–5738 (2005).
11. J. Jiang, Y. Zhong, Y. Zheng, Z. Zeng, X. Ge, and R. Li, “Broadening of white-light continuum by filamentation in BK7 glass at its zero-dispersion point,” Phys. Lett. A **379**, 1929–1933 (2015).

12. R. Budriūnas, D. Kučinskas, and A. Varanavičius, “High-energy continuum generation in an array of thin plates pumped by tunable femtosecond IR pulses,” Appl. Phys. B **123**, 212 (2017).
13. F. Silva, D. R. Austin, A. Thai, M. Baudisch, M. Hemmer, D. Faccio, A. Couairon, and J. Biegert, “Multi-octave supercontinuum generation from mid-infrared filamentation in a bulk crystal,” Nature Commun. **3**, 807 (2012).
14. J. Darginavičius, D. Majus, V. Jukna, N. Garejev, G. Valiulis, A. Couairon, and A. Dubietis, “Ultrabroadband supercontinuum and third-harmonic generation in bulk solids with two optical-cycle carrier-envelope phase-stable pulses at 2 μm,” Opt. Express **21**, 25210–25220 (2013).
15. J. A. Dharmadhikari, R. A. Deshpande, A. Nath, K. Dota, D. Mathur, and A. K. Dharmadhikari, “Effect of group velocity dispersion on supercontinuum generation and filamentation in transparent solids,” Appl. Phys. B **117**, 471–479 (2014).
16. H. Liang, P. Krogen, R. Grynko, O. Novak, C.-L. Chang, G. J. Stein, D. Weerawarne, B. Shim, F. X. Kärtner, and K.-H. Hong, “Three-octave-spanning supercontinuum generation and sub-two-cycle self-compression of mid-infrared filaments in dielectrics,” Opt. Lett. **40**, 1069-1072 (2015).
17. N. Garejev, G. Tamošauskas, and A. Dubietis, “Comparative study of multioctave supercontinuum generation in fused silica, YAG, and LiF in the range of anomalous group velocity dispersion,” J. Opt. Soc. Am. B **34**, 88–94 (2017).
18. S. V. Chekalin, V. O. Kompanets, A. E. Dormidonov, E. D. Zaloznaya, and V. P. Kandidov, “Supercontinuum spectrum upon filamentation of laser pulses under conditions of strong and weak anomalous group velocity dispersion in transparent dielectrics,” Quantum Electron. **47**, 252–258 (2017).
19. A. Marcinkevičiūtė, N. Garejev, R. Šuminas, G. Tamošauskas, and A. Dubietis, “A compact, self-compression-based sub-3 optical cycle source in the $3-4\,\mu$m spectral range,” J. Opt. **19**, 105505 (2017).
20. D. Faccio, A. Averchi, A. Lotti, M. Kolesik, J. V. Moloney, A. Couairon, and P. Di Trapani, “Generation and control of extreme blueshifted continuum peaks in optical Kerr media,” Phys. Rev. A **78**, 033825 (2008).
21. F. V. Potemkin, E. I. Mareev, and E. O. Smetanina, “Influence of wavefront curvature on supercontinuum energy during filamentation of femtosecond laser pulses in water,” Phys. Rev. A **97**, 033801 (2018).
22. D. Majus, V. Jukna, E. Pileckis, G. Valiulis, and A. Dubietis, “Rogue-wave-like statistics in ultrafast white-light continuum generation in sapphire,” Opt. Express **19**, 16317–16323 (2011).
23. L. Zhang, T. Xi, Z. Hao, and J. Lin, “Supercontinuum accumulation along a single femtosecond filament in fused silica,” J. Phys. D **49**, 115201 (2016).
24. A. K. Dharmadhikari, J. A. Dharmadhikari, and D. Mathur, ”Visualization of focusing-refocusing cycles during filamentation in BaF_2,” Appl. Phys. B **94**, 259–263 (2009).
25. D. Kudarauskas, G. Tamošauskas, M. Vengris, and A. Dubietis, “Filament-induced luminescence and supercontinuum generation in undoped, Yb-doped, and Nd-doped YAG crystals,” Appl. Phys. Lett. **112**, 041103 (2018).
26. A. Moroño and E. Hodgson, ”On the origin of the F^+ centre radioluminescence in sapphire,“ J. Nucl. Mater. **249**, 128–132 (1997).
27. A. Couairon, E. Brambilla, T. Corti, D. Majus, O. de J. Ramírez-Góngora, and M. Kolesik, “Practitioner‘s guide to laser pulse propagation models and simulation,” Eur. Phys. J. Spec. Top. **199**, 5–76 (2011).
28. M. J. Weber, *Handbook of optical materials* (CRC press, 2002).
29. A. Major, F. Yoshino, I. Nikolakakos, J.S. Aitchison, and P.W.E. Smith, “Dispersion of the nonlinear refractive index in sapphire,” Opt. Lett. **29**,602–604 (2004).
30. S. Guizard, P. Martin, Ph Daguzan, G. Petite, P. Audebert, J. P. Geindre, A. Dos Santos and A. Antonnetti, “Contrasted Behaviour of an Electron Gas in MgO, Al2O3 and SiO2,” EPL **29**, 401 (1995).
31. M. Mlejnek, E. M. Wright, and J. V. Moloney, “Dynamic spatial replenishment of femtosecond pulses propagating in air,” Opt. Lett. **23**, 382–384 (1998).
32. A.L. Gaeta, “Catastrophic collapse of ultrashort pulses,” Phys. Rev. Lett. **84**, 3582–3585 (2000).
33. A. Jarnac, G. Tamošauskas, D. Majus, A. Houard, A. Mysyrowicz, A. Couairon, and A. Dubietis,“Whole life cycle of femtosecond ultraviolet filaments in water,” Phys. Rev. A **89**, 033809 (2014).
34. J. Galinis, G. Tamošauskas, I. Gražulevičiūtė, E. Keblytė, V. Jukna, and A. Dubietis, “Filamentation and supercontinuum generation in solid-state dielectric media with picosecond laser pulses,” Phys. Rev. A **92**, 033857 (2015).

A3

FILAMENTATION AND PULSE SELF-COMPRESSION IN THE ANOMALOUS DISPERSION REGION OF GLASSES

A. Couairon, V. Jukna, J. Darginavičius, D. Majus, **N. Garejev**,
I. Gražulevičiūtė, G. Valiulis, G. Tamošauskas, A. Dubietis,
F. Silva, D. R. Austin, M. Hemmer, M. Baudisch, A. Thai,
J. Biegert, D. Faccio, A. Jarnac, A. Houard, Y. Liu,
A. Mysyrowicz, S. Grabielle, N. Forget, A. Durécu, M. Durand,
K. Lim, E. McKee, M. Baudelet, M. Richardson

in Laser Filamentation Mathematical Methods and Models,
eds. A. D. Bandrauk, E. Lorin, J. V. Moloney,
(Springer, 2016) pp. 147–165.

Filamentation and Pulse Self-compression in the Anomalous Dispersion Region of Glasses

A. Couairon, V. Jukna, J. Darginavičius, D. Majus, N. Garejev, I. Gražulevičiūtė, G. Valiulis, G. Tamošauskas, A. Dubietis, F. Silva, D.R. Austin, M. Hemmer, M. Baudisch, A. Thai, J. Biegert, D. Faccio, A. Jarnac, A. Houard, Y. Liu, A. Mysyrowicz, S. Grabielle, N. Forget, A. Durécu, M. Durand, K. Lim, E. McKee, M. Baudelet, and M. Richardson

---

A. Couairon (✉) • V. Jukna
Centre de Physique Théorique, CNRS, Ecole Polytechnique, 91128 Palaiseau, France
e-mail: couairon@cpht.polytechnique.fr

J. Darginavičius • D. Majus • N. Garejev • I. Graz̧ulevičiūtė • G. Valiulis • G. Tamošauskas
A. Dubietis
Department of Quantum Electronics, Vilnius University, Saulėtekio Avenue 9, Building 3, 10222
Vilnius, Lithuania

F. Silva • D.R. Austin • M. Hemmer • M. Baudisch • A. Thai
ICFO—Institut de Ciències Fotòniques, Mediterranean Technology Park, 08860 Castelldefels,
Barcelona, Spain

J. Biegert
ICFO—Institut de Ciències Fotòniques, Mediterranean Technology Park, 08860 Castelldefels,
Barcelona, Spain

ICREA—Institució Catalana de Recerca i Estudis Avançats, 08010 Barcelona, Spain

D. Faccio
School of Engineering and Physical Sciences, Heriot-Watt University, Edinburgh EH14-4AS, UK

A. Jarnac • A. Houard • Y. Liu • A. Mysyrowicz
Laboratoire d'Optique Appliquée, ENSTA ParisTech, Ecole Polytechnique, CNRS, 91762
Palaiseau, France

S. Grabielle • N. Forget
FASTLITE, Centre Scientifique d'Orsay, Plateau du Moulon, 91401 Orsay, France

A. Durécu,
Onera-The French Aerospace Lab, BP 80100, 91123 Palaiseau Cedex, France

M. Durand
Laboratoire d'Optique Appliquée, ENSTA ParisTech, Ecole Polytechnique, CNRS, 91762
Palaiseau, France

Towns Laser Institute, CREOL-The College of Optics and Photonics, University of Central
Florida, Orlando, FL 32816, USA

K. Lim • E. McKee • M. Baudelet • M. Richardson
Townes Laser Institute, CREOL-The College of Optics and Photonics, University of Central
Florida, Orlando, FL 32816, USA

A.D. Bandrauk et al. (eds.), *Laser Filamentation*, CRM Series in Mathematical
Physics, DOI 10.1007/978-3-319-23084-9_6

Abstract The propagation of near-infrared ultra-short laser pulses in the regime of anomalous dispersion of transparent solids is associated with a host of self-induced effects including a significant spectral broadening extending from the ultraviolet into the infrared region, pulse self-compression down to few-cycle pulse durations, free and driven third harmonic generation, conical emission and the formation of stable filaments over several cm showing the emergence of conical light bullets. We review measurements performed in different experimental conditions and results of numerical simulations of unidirectional propagation models showing that the interpretation of all these phenomena proceeds from the formation of non-spreading conical light bullets during filamentation.

1 Introduction

Laser pulses with central wavelengths in the near and mid-infrared region are available in many laboratories. All sources are exclusively based on optical parametric amplifiers since there are no femtosecond lasers operating in this range. As shown in Fig. 1, which illustrates the variation of the second order dispersion coefficient k_0'' as a function of wavelength for different materials, near- and mid-infrared laser sources operating at 2 or 3 µm lie within the region of anomalous dispersion for fused silica, calcium fluoride, and YAG.

This opens up new possibilities for filament based applications [1]: for instance, nonlinear pulse propagation in this regime leads to pulse compression rather than pulse splitting and the possibility for ultrabroadband generation from supercontinuum generation. The generation of odd harmonics in the lowest orders falls into the visible region providing a direct probing of higher order nonlinearities. The development of near and mid-infrared laser sources also led to new investigations on the fundamentals of filamentation in transparent solids. Several publications in this area during the last 2 years [2–9] uncovered filamentation physics specific to the anomalous dispersion regime and clarified the links between pioneering results [10–12].

Fig. 1 Group velocity dispersion of fused silica, CaF_2 [13] and YAG [14]. For each material, the *gray area* indicates the anomalous dispersion region

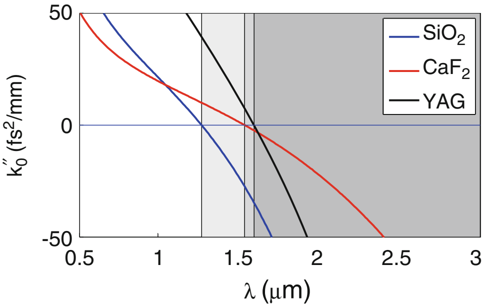

In 2003, Moll and Gaeta investigated the role of dispersion in *multiple collapse dynamics* [10]. On the basis of experiments and numerical simulations, they have shown that the filamentation length is extended in the anomalous dispersion regime: collapse events can occur at locations in the medium many diffraction lengths beyond the initial collapse point, in contrast with the normal dispersion regime in which multiple collapse occurs within a diffraction length.

In 2005, Kolesik, Wright, and Moloney proposed an interpretation of conical emission of femtosecond laser pulses propagating in bulk media [11], valid in the normal as well as in the anomalous dispersion regime. They have shown that the input pulse with initially localized spectrally resolved far-field is scattered off a *material wave*, which is nothing but the self-generated nonlinear polarization wave associated with nonlinear propagation of the pulse. This results in preferential locations for populating the far-field, which can be predicted by an effective three wave mixing model and phase matching arguments.

The same year, Porras et al. have discovered a new type of spatiotemporal light bullet, which is nonsolitary and exhibits a conical nature [12]. Concretely, they have found a stationary solution to an extended nonlinear Schrödinger equation describing propagation in a Kerr medium, in the regime of anomalous dispersion, and in the presence of nonlinear losses. This solution represents a nonlinear and stable statiotemporal wavepacket that does not spread in space or time and withstands nonlinear losses. For this reason, it differs from a soliton or a light bullet as defined by Silberberg [15]. Figure 2 shows a typical profile for this solution, which takes the form of a nonlinear Bessel function along a reduced coordinate $R \equiv \sqrt{r^2 + t^2/k_0 k_0''}$ combining the transverse spacial coordinate r and the pulse local time t, where k_0 and k_0'' denote the wavenumber and the second order dispersion coefficient in the medium at the central wavelength of the pulse. These solutions have a ring shaped spectrum indicating that wavenumbers are distributed along the

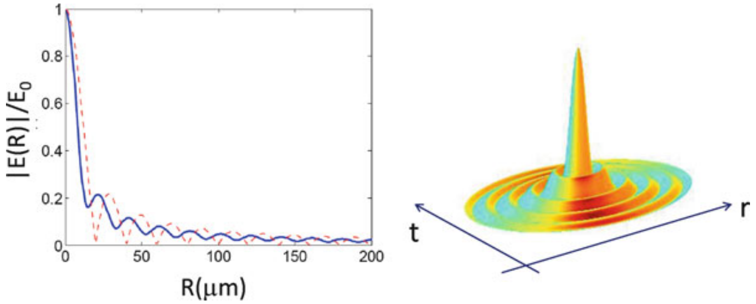

Fig. 2 (**a**) Amplitude profile for conical light bullets (nonlinear O-waves from the theory in[12]) supported by anomalous dispersion with normalized intensity. Solutions exist as a continuous family parametrized by the maximum amplitude. In this example, the *dashed red curve* corresponds to a linear solution. The continuous *blue curve* is typical for nonlinear solutions and corresponds to the a peak intensity of 9×10^{12} W/cm^2. (**b**) Space-time representation of the amplitude of conical light bullets

Fig. 3 Side view photography of the blue fluorescence of fused silica induced by a near infrared laser pulse at 1.9 µm with 8 µJ energy. The laser pulse is focused on a 70 µm spot (FWHM) at the entrance surface of the 3 cm thick sample. *Vertical dash-dotted lines* indicate the positions of the entrance and exit surfaces of the sample. Adapted from [5]

surface of a cone. This is typical for Bessel-like profiles. This solution can therefore be viewed as a nonlinear polychromatic Bessel beam, i.e., a light bullet with a conical nature.

The goal of this chapter is to show the links between these three results in light of recent experimental results which led us to discover a new filamentation regime, featured by pulse self-compression, stationarity, and the formation of similar light bullets as those predicted by Porras et al. [12]. Figure 3 illustrates this new filamentation regime, obtained by recording with a CCD camera the side image of the blue luminescence after focusing the beam of a 40 fs, 8 µJ laser pulse at wavelength of 1.9 µm on the entrance surface of a 3 cm-thick block of fused silica. The measurement reveals a thin and regular filamentary track extending over a large part of the sample in the anomalous dispersion regime, whereas a significantly shorter filament with multiple refocusing cycles is obtained in the regime of normal dispersion [5].

The outline of this chapter is the following. Section 2 briefly presents the model used in this work for numerical simulations of nonlinear pulse propagation and filamentation. Section 3 deals with investigations on ultrabroadband supercontinuum generation. Section 4 shows that these spectra are a signature of efficient pulse self-compression. Section 5 shows that a visible spectral peak appears in the ultrabroadband spectra, corresponding to the axial part of conical emission. Section 6 deals with free and driven third harmonic generation, and finally Sect. 7 shows measurements and simulations on a new filamentation regime where dissipative spatiotemporal light bullets emerge.

2 Numerical Simulation Model

For interpreting the measurements, numerical simulations were performed on the basis of unidirectional propagation equations [16, 17]. The Maxwell Wave Equation (MWE) describes the evolution of the pulse electric field along z, the propagation axis.

$$\begin{aligned}\frac{\partial \hat{E}(z,\omega,r)}{\partial z} &= \mathrm{i}(k(\omega) - k_0'\omega)\hat{E} \\ &\quad + \frac{\mathrm{i}}{2k(\omega)}\nabla_\perp^2 \hat{E} + \frac{1}{2\epsilon_0 c n(\omega)}[\mathrm{i}\omega \hat{P}(z,\omega,r) - \hat{J}(z,\omega,r)], \qquad (1)\end{aligned}$$

where $\hat{E}(z,\omega,r) = \mathcal{F}[E(z,t,r)]$ denotes the frequency components (Fourier transform $t \to \omega$) of the laser electric field $E(z,t,r)$ and the transverse coordinate r indicates that revolution symmetry is assumed. The effects accounted for include material dispersion via a Sellmeier dispersion relation for the medium $k(\omega)$, diffraction, and the nonlinear response of the medium described by the nonlinear polarization

$$P(z,t,r) \equiv \epsilon_0 \chi^{(3)} E^3(z,t,r) \tag{2}$$

and current $J(z,t,r)$ source terms. These terms in turn represent the main effects playing a role in filamentation: the optical Kerr effect with nonlinear index coefficient n_2, ($\chi^{(3)} \equiv (4/3)\epsilon_0 c n_0^2 n_2$), plasma effects including ionization, plasma defocusing and absorption and nonlinear absorption governed by the system of Eqs. (3)–(5)

$$\frac{\partial J_e}{\partial t} + \frac{J_e}{\tau_c} = \frac{q_e^2}{m_e}\rho E(z,t,r) \tag{3}$$

$$\frac{\partial \rho}{\partial t} = W(E)(1-\rho/\rho_b) + \frac{\sigma}{U_i}\rho E^2 \tag{4}$$

$$J(z,t,r) = J_e + \epsilon_0 c n_0 \frac{W(E)}{E^2} U_i (1-\rho/\rho_b) E, \tag{5}$$

where q_e and m_e denote the electron charge and mass, τ_c the effective collision time, σ the cross section for inverse Bremsstrahlung, U_i the bandgap of the material, and ρ_b the background neutral atom density. Optical field ionization rates $W(E)$ are described by the Keldysh formulation. The model is valid for describing the propagation of few-cycle pulses with broad spectra. A formally analogous formulation based on an envelope propagation equation will be also used when explicitly specified. In the latter case, ionization rates and nonlinearity depend on intensity rather than on the field squared.

3 Supercontinuum Generation

3.1 Supercontinuum Generation in Glasses at 2 μm

Figure 4 shows a series of measurements for the supercontinuum spectra obtained by propagation of 15 fs (2.3 optical-cycle), CEP-stable pulses with central wavelength of 2 μm in different solid media, fused silica, CaF_2 and YAG. The corresponding conical emission is shown as a cross section of the emerging beam taken at 15 cm distance from the output face of the nonlinear medium.

Different features are observed: (1) generation of supercontinuum spectra; (2) presence of a spectral peak in the visible region; (3) emergence of a third harmonic

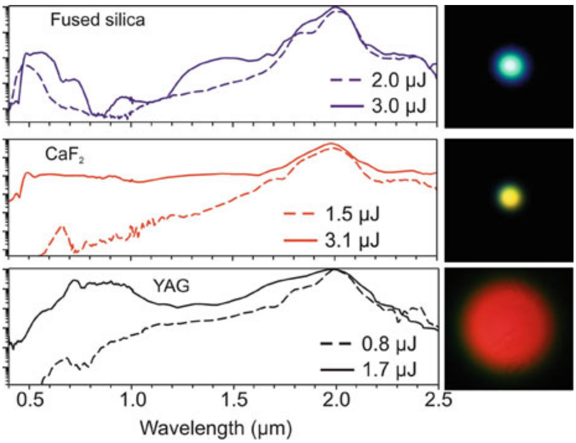

Fig. 4 Supercontinuum spectra generated in (**a**) fused silica, (**b**) CaF_2, (**c**) YAG. The *dashed* and *solid curves* represent supercontinuum spectra in the transient and saturation regimes of the spectral broadening, respectively. Curve labels stand for the input-pulse energy. Images on the *right side* show the corresponding far-field patterns of the conical emission in the visible range, recorded in the saturated regime of the spectral broadening. Adapted from [4]

peak for moderate pulse energy, and (4) conical emission in the form of angular spreading of visible light. These features are quite generic and reproducible in different media, at other pulse wavelengths and durations.

In fused silica, the supercontinuum spectrum has a deep extended minimum around 1 μm and a distinct intense peak in the visible (blue peak), which shows red-shifted broadening with increase of the input-pulse energy. CaF_2 exhibits lower dispersion than fused silica: a broad and flat supercontinuum spectrum from 450 nm to more than 2.5 μm was generated. In YAG which has higher nonlinearity, a smooth supercontinuum spectrum with elevated spectral intensity in the visible near-infrared 600–1000 nm range was generated using low input-pulse energy. The differences in conical emission bear upon the characteristic coloring and angular divergence of the supercontinuum radiation in the saturated regime of the spectral broadening, corresponding to higher values of the input-pulse energy. Among the tested materials YAG has the highest nonlinear index of refraction, leading to a strong laser–matter interaction, and the largest dispersion, therefore visible extension of supercontinuum in YAG has the largest angular spread. This feature will be further commented in Sect. 5.

In all cases, prior to supercontinuum generation, a characteristic third harmonic peak centered at 660 nm was observed. Its nature is discussed in Sect. 6. It is best visible in CaF_2 and YAG. In fused silica, it becomes rapidly masked by the strong and broad visible peak when energy is increased, which is distinct from the third harmonic as will be thoroughly explained in Sect. 5.

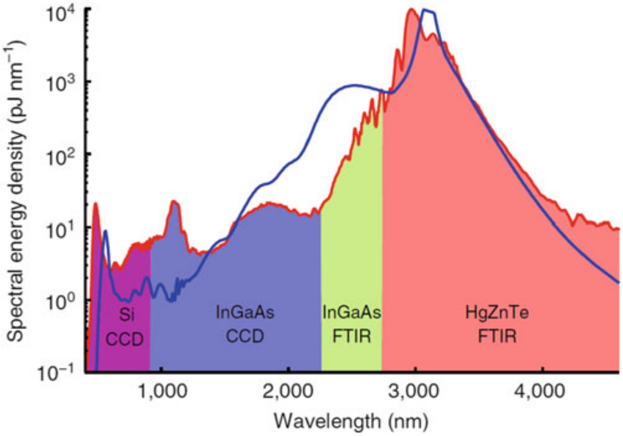

Fig. 5 Supercontinuum generated by 3100 nm, 2.6 μJ pulses in YAG (*red*). The ranges of each spectrometer/detector are indicated and superimposed is the angle-integrated spectrum from our simulation (*blue*). Two different detectors (InGaAs and HgCdZnTe) were used to cover the long wavelength region. FTIR, Fourier Transform Infrared Spectrometer. Adapted from [2]

3.2 Supercontinuum Generation in YAG at 3 μm

Recent experimental results have shown ultrabroadband supercontinuum generation in a YAG crystal from mid-IR laser pulses with central wavelength of 3 μm [2]. Pulses of 7 μJ energy were focused in a 2 mm-thick YAG plate placed in the focal region. It produced a clearly visible filament. After the exit plane of the YAG plate, we recorded spectra by imaging the supercontinuum into four spectrometer fibers. Each fiber delivered light to four different spectrometers working in different spectral regions, as indicated by the colored regions in Fig. 5. Intensity calibrations were applied for ensuring consistency in their regions of overlap (925, 2300 and 2700 nm) and with the measured pulse energy.

The result is shown in Fig. 5, along with a corresponding numerical simulation. The spectrum shows that the long wavelength edge decays smoothly, reaching the noise level at 4.5 μm. The short wavelengths extend down to 450 nm. The highest spectral energy density is found around the mid-infrared pump wavelength. The smallest energy content is observed in the 750–1000 nm range at a few picojoules per nanometer.

We observed two spectral peaks at 600 and 1100 nm seemingly close to the third and fifth harmonics. The blue curve corresponds to the result of a numerical simulation. It does reproduce well the peak in the visible region but not the third harmonic which merges in the supercontinuum. Another simulation with an envelope formulation, which does not account for harmonic generation, produced the same features in the supercontinuum spectrum, in particular a prominent visible peak, suggesting that this peak at 600 nm is not related to fifth harmonic generation.

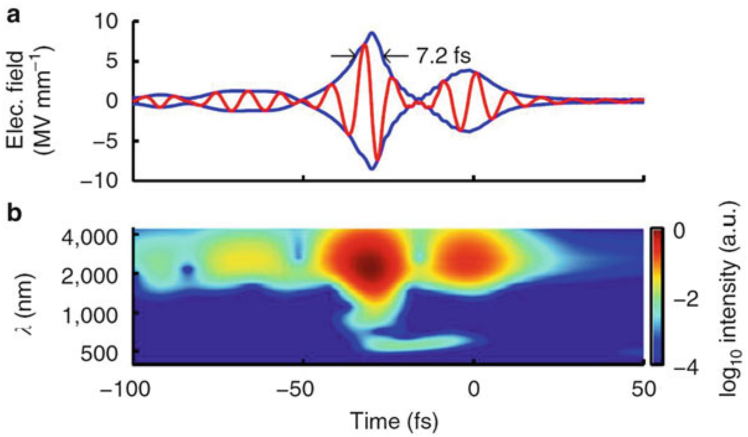

Fig. 6 Temporal profile and spectrogram of the output pulse after filamentation in YAG at 3 μm. (**a**) Temporal envelope (*blue*) and field oscillations (*red*) and (**b**) spectrogram of the on-axis simulated pulse emerging from the YAG plate; note the logarithmic intensity colour scale in the spectrogram. Adapted from [2]

Simulations with the MWE (1) and (3)–(5) detailed how the spectrally resolved far-field is populated along propagation [2]. The visible peak appeared in the last 400 μm of the YAG plate and is not affected by harmonic generation. Its generation is due to a scattering process explained in Sect. 5. It coincides with the loci of phase-matched angle and wavelength lying in the visible region of the spectrum, i.e., this peak is nothing but the axial part of conical emission. The presence of this spectral peak is also a strong signature of the partial reshaping of the pulse into O- or fishlike waves in media with anomalous dispersion [18–20].

We used the numerics to examine the potential of our setup for pulse compression. Figure 6a shows a typical output temporal on-axis profile obtained by numerical simulation. We found that the pulse duration has been reduced by a factor of 10 (the satellite peaks are 50 % lower in peak intensity), and the main peak has near-single-cycle duration. A more complete picture of the output pulse is given by the spectrogram shown in Fig. 6b. The short wavelength components, below 1500 nm, emerge from the output face nearly simultaneously with the main peak. The overall time-frequency distribution is simple, containing only a few distinct peaks. Therefore, the numerics indicate the possibility of achieving in an extremely simple setting, near-single-cycle and carrier-envelope phase stable pulses using mid-infrared pump lasers.

4 Pulse Self-compression in the Regime of Anomalous Dispersion in Glasses

We used the simple experimental setup sketched in Fig. 7a to investigate direct pulse self-compression. The parameters of this setup consist of a 10 cm focal length CaF_2 lens and a 3-mm thick, Yttrium Aluminum garnet (YAG) plate which was moved 6 mm across the focal plane in steps of 0.5 mm to initiate nonlinear propagation inside the plate at different peak intensities. The emerging beam was collimated with a silver-coated mirror and the pulse was characterized with frequency-resolved optical gating (FROG). The FROG device was specifically designed to handle ultrabroad bandwidths in the mid-IR region [21]. Mid-IR spectra were also measured using a Fourier transform infrared spectrometer.

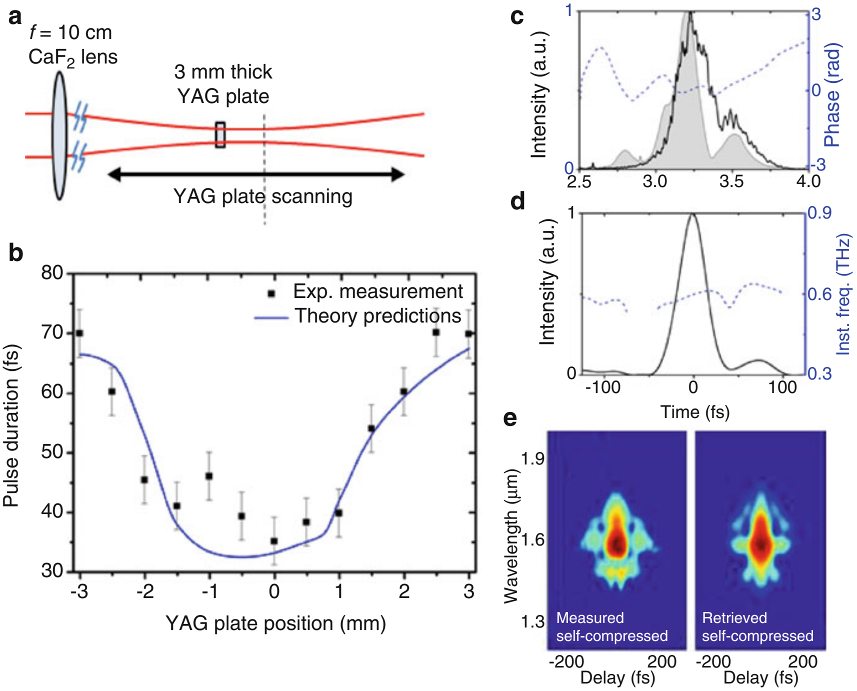

Fig. 7 (**a**) Layout of the self-compression setup. The input beam is focused by a 10 cm focal length CaF_2 lens into a 3 mm-thick YAG plate. The YAG plate is moved along the beam propagation axis, through focus. (**b**) Measured (*black dots*) and simulated (*blue line*) evolution of the pulse duration as a function of YAG plate position through focus. (**c**) Measured (*black line*) and retrieved (*shadow*) spectra of the self-compressed pulses. (**d**) Retrieved normalized 32 fs (2.9-cycle) duration intensity profile of the self-compressed pulses. (**e**) Measured and retrieved SHG-FROG traces of the self-compressed pulses on logarithmic color scale. Adapted from [3]

The results in Fig. 7c show measured and simulated durations of the emerging pulse as a function of the YAG plate position, representing the distance between the front of the YAG plate and the linear focus. Simulations and experiments are in good agreement. They indicate that self-compression to 32 fs (2.9 cycle) occurs and that no pulse splitting is observed. Optimum self-compression conditions for 3 μJ seed pulses were identified and the optimally self-compressed pulses were carefully characterized by sampling the inner part of the beam. Figure 7c–e show measured and retrieved FROG traces with a maximum 0.5 % error. Figure 7d shows the optimally self-compressed pulse. The measured spectrum in Fig. 7c for the optimally self-compressed pulse shows an extent of over 1000 nm and the retrieved spectrum from the FROG measurement is in good agreement with the measured spectrum confirming the consistency of the measurement. We retrieve a FWHM pulse duration of 32 fs which corresponds to 2.9-cycles of electric field at the slightly red-shifted output of 3200 nm. The spatial profile of the beam after self-compression was measured using a knife-edge technique and showed that the process left the seed spatial profile undisturbed.

5 Conical Emission

Nonlinear propagation of an intense laser pulse generates new frequencies leading to the supercontinuum. The angular spread in the visible wavelength range is regarded as conical emission, whose angles are set by dispersion-related phase matching conditions. In other words, for a given material, the phase matching condition entirely determines the loci of the far-field that can be populated in priority, i.e., the dependence of angles as a function of wavelength in the conical emission pattern. The effective scattering of a specific color at a given angle also depends on the nonlinear pulse–matter interaction ensuring that the phase matching condition is fulfilled over a certain propagation distance.

As shown in Figs. 4 and 5, the third harmonic does not always emerge from the supercontinuum and cannot always be distinguished from the spectral peak in the visible region. For instance, near-infrared pump pulses with central wavelength close to 2 μm usually undergo spectral broadening and frequency shift during nonlinear propagation leading to a loosely defined third harmonic wavelength in the visible range.

Figure 8 (right column) indicates the physical origin of the visible spectral peak. We compared the spectrally resolved far-fields obtained by numerical simulation of filamentation in fused silica for different pulse wavelengths ($\lambda_0 = 800, 1200, 1900$ nm, see Fig. 8). We found that the generation of the visible peak is consistent with the effective three wave mixing model proposed by Kolesik et al. [11]. Due to the reshaping of the pulse during nonlinear propagation, the peak field and therefore the nonlinear polarization wave induced by the pulse (2)–(5) travels at velocity v_p, usually slightly lower than the pulse group velocity in the conditions of anomalous dispersion [6, 11]. This constitutes a material wave, the velocity of

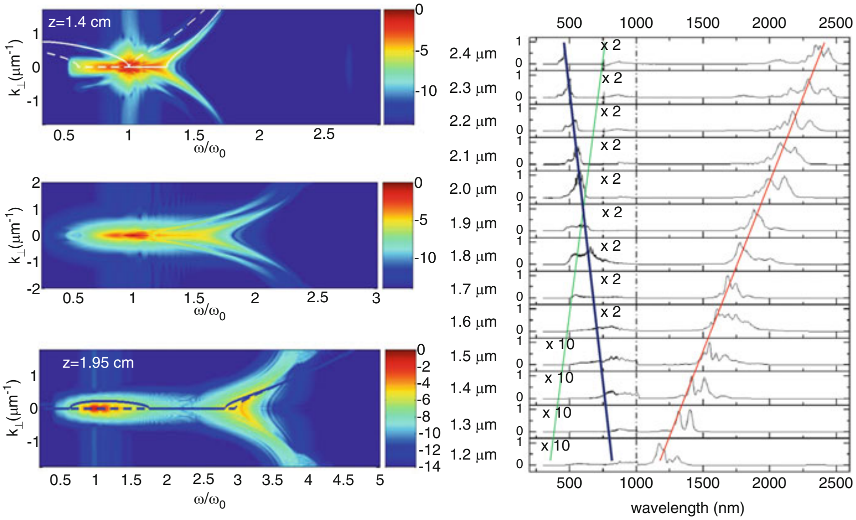

Fig. 8 *Left column*: Spectrally resolved far-fields $k_\perp - \omega$ obtained by numerical simulation of filamentation of 50 fs laser pulses in fused silica, for different pump wavelengths: *First row*: $\lambda_0 =$ 800 nm (normal dispersion). *Second row*: $\lambda_0 = 1200$ nm (close to zero dispersion). *Third row*: $\lambda_0 = 1900$ nm (anomalous dispersion). Units on the logarithmic colorbars correspond to decades in intensity. *Right column*: Supercontinuum spectra measured after filamentation in a 4 cm thick fused silica sample, with variable pump central wavelengths from 1.2 to 2.4 µm. For legibility, magnification factors were applied in the region of the spectra up to 1 µm (10× for $1.2 < \lambda_0 < 1.5$ µm) and 2× for $1.6 < \lambda_0 < 2.4$ µm). Adapted from [6]

which can be quantified from the results of numerical simulations by monitoring the temporal profile of the pulse along propagation (see example below in Fig. 12). Conical emission is essentially interpreted as a scattering process: the pump pulse is scattered off the material wave. Newly generated frequencies will populate the spectrum in regions where the longitudinal phase matching condition (6) between the pump pulse (axial wavenumber k_0), the material wave (axial wavenumber $(\omega - \omega_0)/v_p$), and the scattered wave (k_z) is fulfilled.

$$\Delta k \equiv k_0 + \frac{\omega - \omega_0}{v_p} - k_z(\omega, k_\perp) \simeq 0, \tag{6}$$

$$k_\perp^2 + k_z^2 = k^2(\omega). \tag{7}$$

Equation (7) links transverse and longitudinal components for dispersive waves in the medium, and $k(\omega)$ denotes a Sellmeier like dispersion relation characterizing the medium. The angular distribution of frequencies (or wavelengths) where the far-field is preferentially populated along propagation is obtained by the combination of (6) and (7):

$$k_\perp = \pm\sqrt{k^2(\omega) - [k_0 - \Delta k + \alpha(\omega - \omega_0)]^2} \tag{8}$$

where $\alpha \equiv v_p^{-1}$ and Δk is a free parameter (zero for perfect phase matching).

In Fig. 8, we plotted the phase matching condition (8) for both cases of normal and anomalous dispersion. For $\lambda_0 = 800$ nm, we used two different values of the α parameter, corresponding to the two velocities of the split pulses arising in filaments with normal dispersion [22, 23]. This leads to two pairs of hyperbolic branches (one pair for each velocity highlighted by the white continuous and dashed curves). For $\lambda_0 = 1900$ nm, the same procedure leads to two branches: one is elliptic around the pump, a second one is hyperbolic and marks the conical emission in the visible range. Note that measurements of the spectrally resolved far-field are very well fitted by these branches both in the normal and the anomalous dispersion regimes [11, 23–26], which confirms the physical origin of conical emission and highlights the nature of the spectral peak in visible region of the supercontinuum.

To further confirm that spectral peaks in the visible region originate from dispersive waves populating the supercontinuum and distinguish them from third harmonic generation, another set of experiments was performed on filamentation in fused silica, where the pulse wavelength was varied from 1.2 to 2.4 μm [6]. The experiments clearly confirmed that the visible spectral peak is not related to the third harmonic but corresponds to the axial part of conical emission. The laser source was an OPA pumped by a titanium:sapphire chirped-pulse amplified laser system. The pulses at the output of the OPA had energies up to 100 μJ, at 100 fs. The laser beam was focused with a 50 cm focal length lens inside a 3 cm-long fused silica hexagonal rod. The measurements taken by three spectrometers were combined to cover the spectral range from 300 to 2500 nm. Results are shown in the right column of Fig. 8.

The visible spectral peak, highlighted by a blue line, is clearly shifted to shorter wavelengths when the initial pulse wavelength (red line) is varied to longer wavelengths, ruling out third-harmonic generation as the mechanism at the origin of the visible emission. The green line marks the position of the third harmonic, showing clearly that it is well separated from the visible peak except for a short range of pump wavelengths around 2 μm.

We have finally applied this model to determine the position of the visible peak as a function of the input pulse wavelengths. The results plotted in Fig. 9. The comparison of the model prediction, in solid black curve, with the measurements in red dots, shows very good agreement in the range of pump wavelengths 1500–2000 nm and a slight redshift with respect to the prediction in the range 2000–2400 nm. The figure also shows the extent of the visible spectral peak.

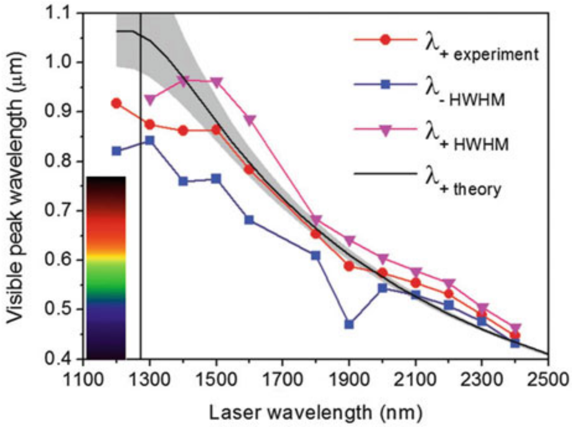

Fig. 9 Comparison of the wavelength of the spectral peak in the visible region obtained from the theory ($\lambda_{+,\text{theory}}$, *black curve*) with the measurements ($\lambda_{+,\text{experiment}}$, *red dotted curve*). The visible peak is generated during filamentation in a 3 cm-thick fused silica sample, as a function of the input pulse central wavelength. The curves $\lambda_{-,\text{HWHM}}$ and $\lambda_{+,\text{HWHM}}$ mark the extent of the visible peak. Adapted from [6]

6 Third Harmonic Generation

As shown in Fig. 4, third harmonic generation is clearly observed before the onset of spectral broadening and supercontinuum generation, in the transient regime of supercontinuum generation [4, 7]. Typically, the third harmonic radiation was detected with half the lowest pulse energies indicated in Fig. 4 in fused silica and in YAG, and the measured third harmonic efficiency varied from 10^{-6} to 10^{-4}, depending on the input-pulse energy.

A closer inspection of third harmonic spectra revealed a fast periodic modulation, whose frequency changed with the nonlinear material and its length. An example of third harmonic spectrum generated with a 15 fs input-pulse with 0.70 µJ energy, before the onset of supercontinuum generation, is shown in Fig. 10a, b for YAG and fused silica, respectively. This spectral modulation is a signature of a double-peaked third harmonic pulse, which occurs naturally, without the splitting of the input pulse. We interpret our results in the framework of large phase and group-velocity mismatched third harmonic generation [27]. The operating conditions impose that the third harmonic radiation consists of two pulses, the free and driven waves, which are solutions to the homogeneous and the inhomogeneous wave equations, respectively. The free third harmonic wave propagates at the velocity u_f set by the material dispersion, and walks-off from the pump pulse, i.e., the input-pulse at the fundamental frequency. The driven third harmonic wave propagates at the same velocity u_d as the nonlinear polarization and appears as locked under the pump, i.e., travels at the pump pulse group velocity (see Fig. 10a, b).

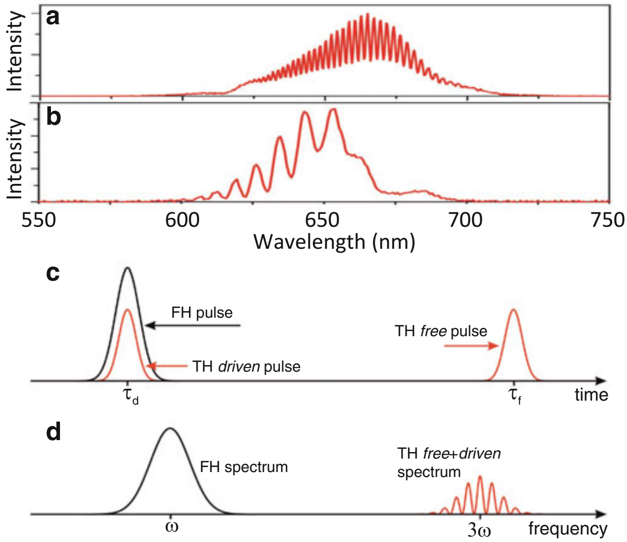

Fig. 10 (**a**), (**b**) Fringe pattern in the third harmonic spectra after propagation of a 15 fs pulse in (**a**) 6 mm of YAG, suggesting two pulses separated by 670 fs and (**b**) 5 mm of fused silica. (**c**), (**d**) Sketch for the generation of third harmonic radiation in the conditions of large phase and group velocity mismatch. (**c**) Time domain and (**d**) frequency domain

The emerging third harmonic radiation consists of two pulses separated in time by a duration $(u_f^{-1} - u_d^{-1})L$, proportional to the group velocity mismatch, where L denotes the medium length. This produces beating in the third harmonic spectrum with frequency inversely proportional to the temporal separation between the free and driven components. By inserting the relevant values for YAG: $L = 6$ mm and group velocity mismatch $u = 115$ fs/mm, the estimated temporal separation between the free and driven third harmonic pulses is 690 fs, which is very close to that of 670 fs, as retrieved from the fringe pattern shown in the spectrum.

In order to verify our interpretation, we performed numerical simulations with the model described in Sect. 2. Figure 11a shows the result of numerical simulation for the spectrally resolved far-field in the transient regime of spectral broadening in YAG. The inset shows the magnified portion of the third harmonic spectrum in the 550–750 nm range, highlighting the spectral beatings. The profiles in Fig. 11b show the respective temporal profiles of the main (pump) pulse (black curves) and pulses at the third harmonic wavelength (red curves), retrieved by using a super-Gaussian filter with full width at half maximum of 150 nm and centered at 660 nm. The retrieved third harmonic temporal profile consists of two distinct pulses temporally separated by 700 fs. They correspond to the *free* and *driven* third harmonic pulses, in fair agreement with our analytical interpretation and experimental results. The driven third harmonic pulse remains short as it is locked under the envelope of the fundamental (pump) pulse, which does not broaden much due to the interplay

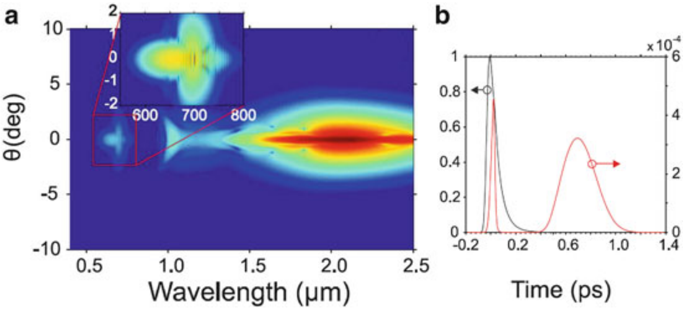

Fig. 11 (**a**) Spectrally resolved far-fields in YAG in the transient regime (**a**) of spectral broadening. The *inset* highlights the modulation around the third harmonic spectral range. (**b**) shows the normalized temporal profiles of the pump (*black curve*) and third harmonic (*red curves*) pulses after spectral filtering. Additional *arrows* in (**b**) indicate driven (*on the left*) and free (*on the right*) third harmonic pulses. Adapted from [4]

of self-phase modulation and anomalous dispersion, while the free third harmonic pulse moves away and experiences considerable temporal broadening due to normal dispersion.

7 Conical Light Bullets Generated by Filamentation in the Anomalous Dispersion

Figure 3 presented in introduction constitutes a typical result for filamentation in the anomalous dispersion regime of transparent solids. In an energy range above the threshold, the filament is very regular, featured by an absence of focusing-defocusing cycle sustaining filaments in the normal dispersion regime, at shorter wavelengths. These cycles, however, appear in the anomalous dispersion regime when the input pulse energy is increased and for slightly different focusing conditions [28] but after a few cycles, the filament regularizes and becomes regular as in Fig. 3 [5].

Numerical simulation results with the parameters of the experiments of Fig. 3 are shown in Fig. 12. The beam shrinks and forms the filament with a fairly constant diameter over more than 2 cm (Fig. 12a). Figure 12b shows the evolution of the axial temporal profile of the pulse, in the local frame, along the propagation distance. Both results show the emergence of a stable non-spreading structure in space of time at the origin of the filamentary track extending over a large part of the sample. This structure possesses some attributes of light-bullets, as introduced by Silberberg, referring to *a pulse that propagates without changing its temporal or spatial shape, held together by the nonlinear forces* [15]. Our measurements and simulations show quasi-stationary pulses, which do not change temporal or spatial shape for several diffraction lengths.

Fig. 12 Results of numerical simulation for the propagation through fused silica of an optical pulse at 1.9 µm of 110 µm diameter and 40 fs duration (FWHM) and 5×10^{11} W/cm^2 intensity collimated on the front sample surface. (**a**) Beam radius as a function of distance *z*. (**b**) Axial temporal profile of the laser pulse. Numbers on the colorbar denote TW / cm^2. Adapted from [5]

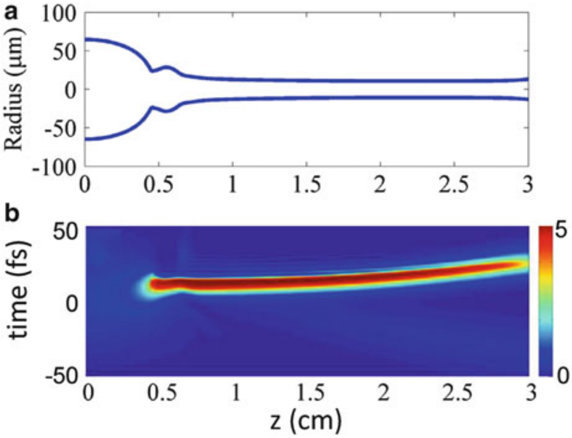

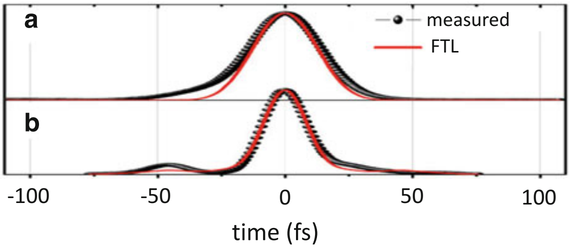

Fig. 13 Temporal pulse shape measured with the Wizzler for the initial pulse (40 fs FWHM) (**a**) and for filament lengths of 0.5 cm (20 fs FWHM) (**b**). Also shown in *red* is the Fourier Transform Limited (FTL) pulse. Adapted from [5]

For instance, the duration of the pulse emerging from the sample was characterized by a single-shot, self-referenced spectral interferometry technique called Wizzler operating in the near infrared region [29]. The measurement shown in Fig. 13 corresponds to a fused silica thickness of 5 mm and an integrated profile over 20 shots. A pulse duration of 20 fs was obtained, with a fair reproducibility. Propagation of the infrared pulse has led to self-compression by a factor of two. However, the self-compressed structure does not qualify as light-bullets in Silberberg's sense for two reasons: (1) they continuously lose energy due to multiphoton absorption and (2) they are stable whereas Silberberg's light bullets are unstable in more than one dimension.

In contrast, the pulse undergoing filamentation in the anomalous dispersion regime was shown in [8] to possess self-reconstruction properties and all the attributes of conical light bullets as proposed by Porras et al. [12]. The most important property of these structures is their conical nature allowing them to remain propagation invariant while undergoing multiphoton absorption. This is possible because the high intensity core where energy is lost is continually refueled by an energy flux from the low intensity energy reservoir of the wave. Invariant pulses in this form are found as mathematical solutions to a nonlinear Schrödinger equation accounting for the effects of diffraction, Kerr self-focusing, anomalous dispersion, and multiphoton absorption for any peak intensity up to a certain limit [12]. They are stable provided multiphoton absorption is sufficiently strong, and can therefore be observed in real experiments.

A confirmation of the conical nature of the filament was obtained from numerical simulation results, showing the evolution of the energy density flux along the propagation in the fused silica sample. The complex field (intensity and phase) allows us to reconstruct the energy density flux in the full spatial and temporal coordinates [30]:

$$\mathbf{F} = k_0^{-1} I[(\partial_r \phi)\mathbf{u}_r + \beta(\partial_\zeta \phi)\mathbf{u}_z], \tag{9}$$

where $I(r, \zeta)$ and $\phi(r, \zeta)$ denote the intensity and phase distributions along transverse r and longitudinal $\zeta \equiv k_0'^{-1} t - z$ axes, $\mathbf{u}_r$ and $\mathbf{u}_\eta$ are the unit vectors in the corresponding directions,

Figure 14 shows the energy flux components as arrows, along with an overlaid color plot of the intensity profiles at six distances along the propagation axis. Figure 14a–c evidence the pulse reshaping (compression in space and time) before the propagation invariant stage in Fig. 14d–f, sustained by a density flux essentially directed towards the leading and central part of the pulse from its periphery. A slow shift to the right corresponding to the subluminal motion of the pulse is the only visible change. The spatiotemporal distribution of the currents is almost identical to that of a conical light bullet [30]. We underline that Silberberg's bullets

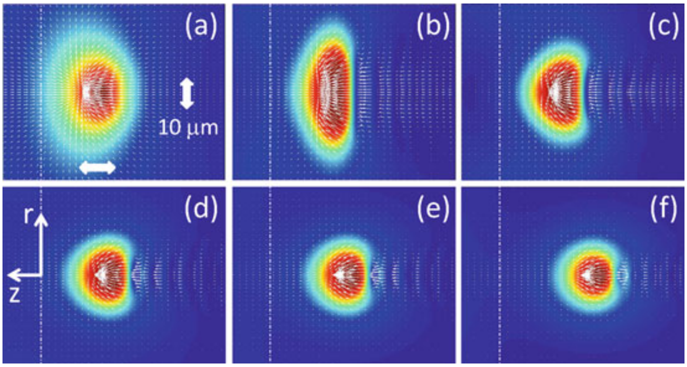

Fig. 14 Energy flux (*white arrows*) superimposed to intensity distribution (in *color*) obtained by numerical simulation at six propagation distances within a fused silica sample. (**a**) $z = 4.5$ mm. (**b**) $z = 6$ mm. (**c**) $z = 7.5$ mm. (**d**) $z = 12$ mm. (**e**) $z = 15$ mm. (**f**) $z = 19.5$ mm. The *dash-dotted lines* indicate the center of the input pulse (local frame center). The *white arrows* in (**a**) indicate the scale of 10 µm valid for all figures. The axis in (**f**) indicate the transverse and the longitudinal coordinates r, z, with the longitudinal direction corresponding to the propagation direction

and solitons exhibit a flat phase and hence no transverse energy density flow in the spatiotemporal domain. Conversely, the energy density flux unveiled by the simulations is inherent to conical light bullets. Together with detailed measurements further highlighting the reconstruction properties of these bullets [8, 9], these results unambiguously show the conical nature of the light bullets generated by self-focusing in a bulk dielectric medium with anomalous dispersion.

8 Conclusion

Laser pulse filamentation in transparent solids for near- and mid-infrared wavelengths leads to a significant spectral broadening and supercontinuum generation spanning more than three octaves. The pulse is efficiently self-compressed down to few-cycle pulse durations. Signatures in the form of free and driven third harmonic generation, conical emission and typical spectral peaks in the visible region, energy flux pointing toward the high intensity peak, propagation invariant O-shaped spatiotemporal intensity profile and characteristic angularly resolved spectrum all point out established properties of conical light bullets.

Acknowledgements We acknowledge support from the French National Agency for Research, the French DGA, the ONERA, the European Social Fund under the Global Grant measure (Grant No. VP1-3.1-ŠMM-07-K-03-001), the Lithuanian Science Council, the Spanish Ministerio De Economia Y Competitividad (MINECO) through "Plan Nacional" (FIS2011-30465-C02-01) and the Catalan Agencia de Gestió d'Ajuts Universitaris i de Recerca (AGAUR) with SGR 2014-2016. This research has been supported by Fundació Cellex Barcelona, LASERLAB-EUROPE grant agreement 284464 and COST Action MP1203. F.S. was partially supported by FCT-Fundaçãso para a Ciência e a Tecnologia grant SFRH/BD/69913/2010 and D.R.A. from the Marie Curie Intra-European Fellowship program, the European Research Council under the European Union's Seventh Framework Programme (FP/2007-2013)/ERC GA 306559. We acknowledge support from the US Army Research Office MURI Program and the State of Florida.

References

1. A. Couairon, A. Mysyrowicz, Phys. Rep. **441**(2–4), 47 (2007)
2. F. Silva, D.R. Austin, A. Thai, M. Baudisch, M. Hemmer, D. Faccio, A. Couairon, J. Biegert, Nat. Commun. **3**, 807 (2012)
3. M. Hemmer, M. Baudisch, A. Thai, A. Couairon, J. Biegert, Opt. Express **21**(23), 28095 (2013)
4. J. Darginavičius, D. Majus, V. Jukna, N. Garejev, G. Valiulis, A. Couairon, A. Dubietis, Opt. Express **21**(21), 25210 (2013)
5. M. Durand, A. Jarnac, A. Houard, Y. Liu, S. Grabielle, N. Forget, A. Durécu, A. Couairon, A. Mysyrowicz, Phys. Rev. Lett. **110**(11), 115003 (2013)
6. M. Durand, K. Lim, V. Jukna, E. McKee, M. Baudelet, A. Houard, M. Richardson, A. Mysyrowicz, A. Couairon, Phys. Rev. A **87**(4), 043820 (2013)
7. N. Garejev, I. Gražulevičiūtė, D. Majus, G. Tamošauskas, V. Jukna, A. Couairon, A. Dubietis, Phys. Rev. A **89**(3), 033856 (2014)

8. D. Majus, G. Tamošauskas, I. Gražulevičiūtė, N. Garejev, A. Lotti, A. Couairon, D. Faccio, A. Dubietis, Phys. Rev. Lett **112**(19), 193901 (2014)
9. I. Gražulevičiūtė, G. Tamošauskas, V. Jukna, A. Couairon, D. Faccio, A. Dubietis, Opt. Express **22**(25), 30613 (2014)
10. K.D. Moll, A.L. Gaeta, Opt. Lett. **29**(9), 995 (2004)
11. M. Kolesik, E.M. Wright, J.V. Moloney, Opt. Express **13**(26), 10729 (2005)
12. M.A. Porras, A. Parola, P. Di Trapani, J. Opt. Soc. Am. B **22**(7), 1406 (2005)
13. M.J. Weber, *Handbook of Optical Materials* (CRC Press, New York, 2003)
14. M. Bass, C. DeCusatis, J. Enoch, V. Lakshminarayanan, G. Li, C. MacDonald, V. Mahajan, E.V. Stryland, *Handbook of Optics*, vol. 4, 3rd edn. (McGraw Hill, New York, 2009)
15. Y. Silberberg, Opt. Lett. **15**(22), 1282 (1990)
16. M. Kolesik, J.V. Moloney, Phys. Rev. E **70**(3), 036604 (2004)
17. A. Couairon, E. Brambilla, T. Corti, D. Majus, O. de J. Ramírez-Góngora, M. Kolesik, Eur. Phys. J. Spec. Top. **199**(1), 5 (2011)
18. M.A. Porras, A. Dubietisand, E. Kučinskas, F. Bragheri, V. Degiorgio, A. Couairon, D. Faccio, P. Di Trapani, Opt. Lett. **30**(24), 3398 (2005)
19. D. Faccio, A. Averchi, A. Couairon, A. Dubietis, R. Piskarskas, A. Matijosius, F. Bragheri, M.A. Porras, A. Piskarskas, P. Di Trapani, Phys. Rev. E **74**(4), 047603 (2006)
20. M.A. Porras, A. Dubietis, A. Matijošius, R. Piskarskas, F. Bragheri, A. Averchi, P. Di Trapani, J. Opt. Soc. Am. B **24**(3), 581 (2007)
21. P.K. Bates, O. Chalus, J. Bieger, Opt. Lett. **35**(9), 1377 (2010)
22. M. Kolesik, E.M. Wright, J.V. Moloney, Phys. Rev. Lett. **92**(25), 253901 (2004)
23. D. Faccio, M. Porras, A. Dubietis, F. Bragheri, A. Couairon, P. Di Trapani, Phys. Rev. Lett. **96**(19), 193901 (2006)
24. D. Faccio, A. Matijosius, A. Dubietis, R. Piskarskas, A. Varanavičius, E. Gaižauskas, A. Piskarskas, A. Couairon, P. Di Trapani, Phys. Rev. E **72**(3), 037601 (2005)
25. D. Faccio, A. Averchi, A. Lotti, P. Di Trapani, A. Couairon, D. Papazoglou, S. Tzortzakis, Opt. Express **16**(3), 1565 (2008)
26. D. Faccio, M.A. Porras, A. Dubietis, G. Tamošauskas, E. Kučinskas, A. Couairon, P. Di Trapani, Opt. Commun. **265**(2), 672 (2006)
27. G. Valiulis, V. Jukna, O. Jedrkiewicz, M. Clerici, E. Rubino, P. Di Trapani, Phys. Rev. A **83**(4), 043834 (2011)
28. E.O. Smetanina, V.O. Kompanets, S.V. Chekalin, A.E. Dormidonov, V.P. Kandidov, Opt. Lett. **38**(1), 16 (2013)
29. T. Oksenhendler, S. Coudreau, N. Forget, V. Crozatier, S. Grabielle, R. Herzog, O. Gobert, D. Kaplan, Appl. Phys. B **99**(1–2), 7 (2010)
30. A. Lotti, A. Couairon, D. Faccio, P. Di Trapani, Phys. Rev. A **81**(2), 023810 (2010)

A4

THIRD- AND FIFTH-HARMONIC GENERATION IN TRANSPARENT SOLIDS WITH FEW-OPTICAL-CYCLE MIDINFRARED PULSES

N. Garejev, I. Gražulevičiūtė, D. Majus, G. Tamošauskas,
V. Jukna, A. Couairon, A. Dubietis

Phys. Rev. A **89**, 033846 (2014)

PHYSICAL REVIEW A **89**, 033846 (2014)

Third- and fifth-harmonic generation in transparent solids with few-optical-cycle midinfrared pulses

N. Garejev,[1] I. Gražulevičiūtė,[1] D. Majus,[1] G. Tamošauskas,[1] V. Jukna,[2] A. Couairon,[2] and A. Dubietis[1,*]
[1]*Department of Quantum Electronics, Vilnius University, Saulėtekio Avenue 9, Building 3, LT-10222 Vilnius, Lithuania*
[2]*Centre de Physique Théorique, CNRS, Ecole Polytechnique, F-91128 Palaiseau, France*
(Received 27 November 2013; revised manuscript received 18 February 2014; published 24 March 2014)

We report an experimental and numerical investigation of third- and fifth-harmonic generation in a CaF_2 crystal with 20 fs (three-optical-cycle), 2 μm driving pulses. The double-peaked temporal profile of the third-harmonic pulse and its propagation dynamics was captured by means of the cross-correlation technique, showing that the third-harmonic pulse naturally consists of free and driven components propagating with different group velocities, and which occur without the splitting of the driving pulse at the fundamental frequency. Relevant characteristics of the harmonics generation process, such as the harmonics spectra, energy oscillations, and conversion efficiency, were measured as functions of propagation length and input-pulse energy and intensity. Our results demonstrate that the fifth harmonic is generated solely via cascaded four-wave mixing between the fundamental and third-harmonic frequency pulses due to cubic nonlinearity, without any detectable contribution of six-wave mixing due to quintic nonlinearity in the process.

DOI: 10.1103/PhysRevA.89.033846　　PACS number(s): 42.65.Ky, 42.65.An

I. INTRODUCTION

Rapid development of high-peak-power near- and midinfrared ultrashort-pulse laser sources, which are exclusively based on optical parametric amplification [1–3], opens exciting possibilities in the emerging field of ultrafast midinfrared nonlinear optics and strong-field physics, allowing studies of nonlinear-optical phenomena in a new regime of laser-matter interaction [4]. Recent experiments established unprecedented landmarks in high-order harmonic generation in gaseous [5], solid-state [6], and liquid [7] dielectric media.

Self-focusing of ultrashort midinfrared pulses in transparent dielectrics gives rise to a qualitatively new filamentation regime [8,9], which emerges from the combined action of self-phase-modulation and anomalous group-velocity dispersion that leads to extended filament length and self-compression of the driving pulse [10,11], thus eventually producing an ultrabroadband, several-octave-spanning supercontinuum, as observed in gaseous [12–14] and solid-state media [15,16]. The ultrabroadband supercontinuum serves as a high-quality compressible seed signal for ultrafast optical parametric amplifiers [17], is used for synthesis of few-optical-cycle pulse shapes [18], and is considered as a potentially useful tool for midinfrared spectroscopy of complex molecular systems [19].

Generation of low-order odd harmonics (third, fifth, seventh, etc.) in the perturbative regime of laser-matter interaction provides a possibility of direct measurements of nonlinear-optical constants of the material, such as nonlinear-optical susceptibilities and optical nonlinearities. In the meantime, generation of low-order odd harmonics is attracting growing attention, since it might serve as an indicator enabling a test of the alleged role of the high-order Kerr effect and saturating nonlinearities in gaseous [20,21] and in solid-state media [22] in particular.

Third-harmonic generation is a frequently observed nonlinear-optical effect, which accompanies filamentation of near-infrared laser pulses in air, with [23] and without [24] the onset of supercontinuum generation; see also [25] and references therein for more details. Using midinfrared driving pulses, the wavelengths of low-order odd harmonics are shifted towards the visible and near infrared, into the transparency range of nonlinear dielectric media, where they could be readily detected by simple means. To this end, generation of third, fifth [26–28], and seventh [29] harmonics by filamentation of midinfrared laser pulses in air was recently experimentally observed. Generation of low-order odd harmonics was also reported under various experimental settings in semiconductors [30], and in liquid [31,32] and solid-state [15,16,33] dielectric media.

In this paper we report detailed experimental and numerical investigations of third- (TH) and fifth- (FH) harmonic generation in a CaF_2 sample of variable thickness as excited with 20 fs pulses at 2 μm. The cross-correlation measurements confirm the emergence of free and driven TH pulses, which produce evolving spectral interference with increasing propagation distance. A detailed study of the harmonics generation process provides direct proofs that the fifth harmonic is generated by means of only cascaded four-wave mixing between the fundamental frequency and third-harmonic pulses.

II. EXPERIMENTAL SETUP

In the experiment we used a home-built optical parametric amplifier, which was pumped by the fundamental frequency (800 nm) of the amplified Ti:sapphire laser (Spitfire-PRO, Newport-Spectra Physics) and delivered carrier-envelope phase-stable 20 fs (three-optical-cycle) pulses at a carrier wavelength of 1.98 μm with up to 10 μJ energy [34]. Its output beam was suitably attenuated and focused by an $f = +100$ mm lens onto a wedge-shaped CaF_2 sample, producing a 55-μm-diameter (FWHM) spot at the input face of the nonlinear medium. The propagation length inside the nonlinear medium was varied in the 110 μm–2 mm range by moving the CaF_2 sample across the focused beam by a motorized translation stage. The harmonics spectra were recorded using a fiber spectrometer with a 16-bit dynamic range detector (QE65000, Ocean Optics). Two automated Si

---

[*] Corresponding author: audrius.dubietis@ff.vu.lt

detectors with a sensitivity of 0.1 pJ/count and 5 fJ/count for the TH and FH energy measurements, respectively, while the energy of the fundamental frequency was measured using a standard energy meter (Ophir) with a pyroelectric sensor (PE9-SH). In that measurement, signals of the fundamental frequency, TH, and FH were separated by a fused silica prism with 60° apex angle. The cross-correlation measurements were performed by means of broadband sum-frequency generation in 0.2-mm-thick β–barium borate crystal (cut for type-I phase matching) by sampling the output pulses with 20 fs, 575 nm reference pulses from the noncollinear optical parametric amplifier (Topas-White, Light Conversion Ltd.), which was pumped by the second harmonic (400 nm) of the laser. The cross-correlation signals of either the driving pulse at fundamental frequency or the TH pulse were discriminated by setting a proper phase-matching angle of the sum-frequency-generating crystal and using a set of color glass filters.

III. THIRD-HARMONIC GENERATION

In isotropic dielectric media, TH generation is regarded as a simple nonlinear process mediated by the cubic (Kerr) nonlinearity. For efficient TH generation, the phase-matching condition $k(3\omega) = k(\omega) + k(\omega) + k(\omega)$ has to be fulfilled, where $k(\omega) = \omega n(\omega)/c$, ω is the frequency, and $n(\omega)$ is the frequency-dependent refractive index. However, owing to high dispersion in the transparency range of condensed media, TH generation is never phase matched in a collinear propagation geometry, and wave-vector mismatch, defined as $\Delta k = k(3\omega) - 3k(\omega)$, is always very large. This in turn imposes that the coherent buildup length, or simply, the coherence length, defined as $L_{\mathrm{coh}} = 2\pi/\Delta k$, is of the order of a few tens of microns and the energy conversion efficiency typically does not exceed several tenths of a percent. On the other hand, the group-velocity mismatch between the driving and TH pulses, $\nu_{13} = 1/u_1 - 1/u_3$, where u_1 and u_3 are the respective group velocities, is very large as well and becomes an equally important factor that strongly affects the dynamics of TH generation.

More specifically, in CaF$_2$ with 1.98 μm driving pulses the calculated $L_{\mathrm{coh}} = 78.5$ μm and $\nu_{13} = 32.4$ fs/mm. The latter converts to a walk-off length of $l_{13} = t_p/|\nu_{13}| = 620$ μm, as calculated for $t_p = 20$ fs input-pulse duration. The combination of large phase and group-velocity mismatches defines rather specific conditions for TH generation, which, in analogy with phase- and group-velocity-mismatched second-harmonic generation [35–38], leads to the occurrence of a double-peaked TH pulse, consisting of so-called free and driven components. Free and driven TH pulses are generated at the boundary between the vacuum and nonlinear medium and represent solutions of the homogenous and the inhomogenous wave equations, respectively [35]. Free and driven TH pulses propagate with different group velocities: a free TH pulse propagates with the group velocity u_3 set by the material dispersion, while a driven TH pulse propagates with the group velocity u_1 of the fundamental frequency (driving) pulse, which induces the nonlinear polarization. With propagation, the temporal separation between free and driven pulses increases as $\tau = |\nu_{13}|z$, where z is the propagation length, producing evolving interference pattern in the TH spectrum, which was recently experimentally observed in fused silica, sapphire, YAG, and CaF$_2$ [16].

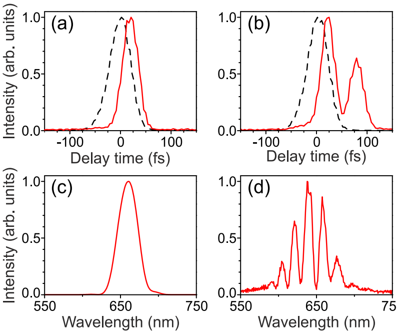

FIG. 1. (Color online) (a),(b) Cross-correlation functions of the fundamental frequency (dashed curves) and TH (solid curves) pulses, as measured with 20 fs sampling pulses, and (c),(d) TH spectra, measured at (a),(c) $z = 0.34$ mm and (b),(d) $z = 1.93$ mm of propagation in CaF$_2$. The input-pulse energy is 1.6 μJ. Fundamental and TH pulse intensities are not to scale.

So far, the existence of free and driven pulses in TH generation has been verified from numerical simulations and indirectly detected from spectral interference patterns [16]. In what follows, we thoroughly investigate TH generation in CaF$_2$ crystal of variable length and directly capture free and driven TH pulses by cross-correlation measurements. Figure 1 shows the cross-correlation functions of driving and TH pulses and the corresponding TH spectra, as recorded at $z = 0.34$ mm and $z = 1.93$ mm of propagation. At a shorter propagation distance, $z = 0.34$ mm, free and driven TH pulses still overlap and are temporally indistinguishable [Fig. 1(a)], resulting in a smooth and featureless TH spectrum, as shown in Fig. 1(c). After $z = 1.93$ mm of propagation, the free and driven pulses are separated due to the group-velocity mismatch [Fig. 1(b)]. Note that the driven TH pulse stays under the envelope of the fundamental frequency (driving) pulse, while the free TH pulse is clearly delayed; the measured temporal separation between their peaks is 59 fs, which is fairly close to the calculated value of 63 fs. A double-peaked structure of the TH pulse results in a distinct interference pattern in the TH spectrum, as seen in Fig. 1(d). A movie (see Movie 1 in the Supplemental Material [39]) shows in more detail the evolution of the TH spectrum versus propagation distance, indicating the emergence and evolution of a clear interference pattern resulting from the increase of the temporal separation between free and driven TH pulses. Note also that the driving pulse at the fundamental frequency is not considerably broadened or split in time due to the interplay between self-phase-modulation and anomalous group-velocity dispersion. It has to be mentioned that a double-peaked TH pulse was reported from air filaments under essentially different operating conditions as due to the splitting of the fundamental frequency pulse in the regime of normal group-velocity dispersion [24].

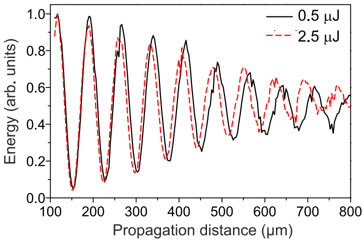

FIG. 2. (Color online) Normalized third-harmonic energy versus propagation distance, as measured with 0.5 μJ (black solid curve) and 2.5 μJ (red dashed curve) input pulses.

Figure 2 shows the variation of TH energy versus propagation distance, as measured with 0.5 and 2.5 μJ input pulses. In both cases we observe periodic oscillations of TH energy, as expected from the condition of large phase mismatch. Damping of energy oscillations results from an increase of temporal separation between the free and driven pulses due to the group-velocity mismatch [36].

At a lower input-pulse energy (0.5 μJ) the retrieved oscillation period of 76.7 ± 0.5 μm is slightly shorter than that calculated in the low-intensity limit in the plane and monochromatic wave approximation, which yields $L_{\text{coh}} = 78.5$ μm. Interestingly, at a higher input-pulse energy (2.5 μJ), the oscillation period shrinks even more, down to 73.2 ± 0.8 μm; its reduction becomes obvious at longer propagation distance, as seen from Fig. 2. The detailed dependence of the oscillation period on the input-pulse energy and intensity is illustrated in Fig. 3. Here the input-pulse energy was varied in the 0.5–3.5 μJ range, so as to avoid the onset of supercontinuum generation. The tail of the supercontinuum in the visible region of the electromagnetic spectrum becomes indeed detectable for input-pulse energies above 3.5 μJ and overlaps with the TH spectrum. This has deleterious effects on the observed energy oscillations.

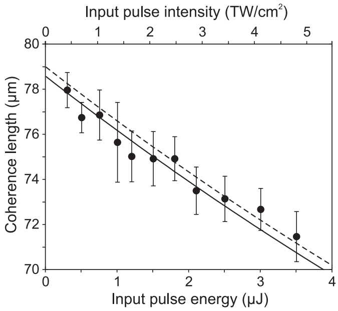

FIG. 3. Coherent buildup length as a function of the input-pulse energy and intensity. Full circles show the experimental data. Solid and dashed curves show the calculated coherent buildup length for 1.98 μm and 2.00 μm driving pulses, respectively.

The observed shortening of the coherent buildup length could be explained in simple terms, accounting for correction of the interacting wave vectors due to self- and cross-phase-modulation (intensity-dependent refractive index) effects:

$$\begin{aligned} k(\omega) &= \frac{\omega}{c}[n(\omega) + n_2 I], \\ k(3\omega) &= \frac{3\omega}{c}[n(3\omega) + 2n_2 I], \end{aligned} \tag{1}$$

where I is the input-pulse intensity and $n_2 = 1.9 \times 10^{-16}$ cm^2/W [40] is the nonlinear refractive index of CaF$_2$. According to Eq. (1), an increase of the input-pulse intensity results in unequal lengthening of the interacting wave vectors, and thus in shortening of the coherence length. The calculated intensity dependence of the coherence length is in fair agreement with experimental results, as seen in Fig. 3. Also note how critically the oscillation period depends on the carrier wavelength; examples of carrier wavelengths of 1.98 μm and 2.00 μm are presented by solid and dashed lines, respectively.

IV. FIFTH-HARMONIC GENERATION

Alongside TH generation we clearly detected a fifth-harmonic signal at around 390 nm. Figure 4(a) shows TH and FH spectra, as measured with the input-pulse energy of 5 μJ at $z = 190$ μm. The respective far-field intensity profiles of FH and TH beams, as recorded with a CCD camera placed at 15 cm distance from the output face of the CaF$_2$ sample, are shown in Figs. 4(b) and 4(c), demonstrating that the FH and TH beams are generated on the propagation axis and have Gaussian intensity distribution, in contrast to the cone-shaped

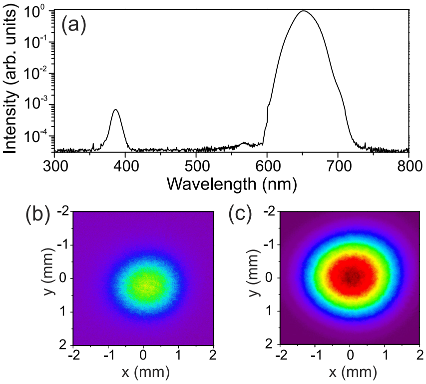

FIG. 4. (Color online) (a) TH and FH spectra as measured after $z = 190$ μm of propagation in CaF$_2$ with the input-pulse energy of 5 μJ. (b) and (c) show the far-field profiles of the FH and TH beams, respectively.

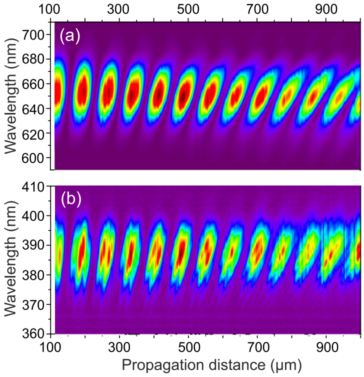

FIG. 5. (Color online) Spectra of (a) TH and (b) FH, as measured by varying the propagation length in CaF$_2$. The input-pulse energy is 2.8 μJ.

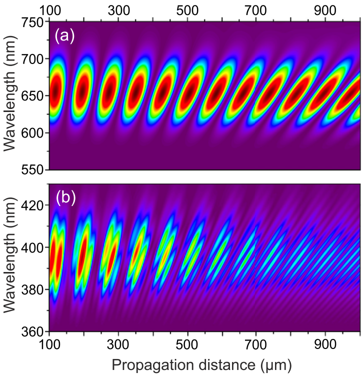

FIG. 6. (Color online) Numerically simulated (a) TH and (b) FH spectra as functions of propagation distance.

harmonic beams observed in high-numerical-aperture focusing conditions [33].

We consider three possible scenarios of FH generation. The first is based on direct FH generation (six-wave mixing) via the quintic nonlinearity $\chi^{(5)}$: $\omega + \omega + \omega + \omega + \omega = 5\omega$, with phase mismatch $\Delta k = k(5\omega) - 5k(\omega)$ and estimated coherent buildup length of $L_{\mathrm{coh}} = 21.8$ μm. The two remaining scenarios are based on four-wave mixing between the fundamental frequency and its TH via the cubic nonlinearity and represent two different cascaded processes [41]. The first cascaded process could be viewed as four-wave sum-frequency generation $3\omega + \omega + \omega = 5\omega$ with phase mismatch $\Delta k = k(5\omega) - k(3\omega) - 2k(\omega)$, which yields a coherent buildup length of 30.2 μm. The second cascaded process could be regarded as four-wave difference-frequency generation $3\omega + 3\omega - \omega = 5\omega$ with corresponding phase mismatch $\Delta k = k(5\omega) - 2k(3\omega) + k(\omega)$ and $L_{\mathrm{coh}} = 49.1$ μm.

In order to find out which processes are at play in the present case, we performed simultaneous spectral measurements of TH and FH radiation versus propagation distance. The experimental data are presented in Fig. 5. A sequence of TH spectral blobs, shown in Fig. 5(a), mimics the periodic oscillations of TH energy with propagation length. Wavelength integration of TH spectral blobs accurately reproduces the variation of TH energy with the oscillation period that matches perfectly the coherence length, as calculated taking into account the self- and cross-phase-modulation effects. The apparent slanting of the spectral blobs, which increases with increasing propagation distance, is attributed to interference between free and driven TH pulses: the cross section of the blobs at a fixed z yields actual shapes of TH spectra with evolving interference pattern, whose example is presented in the movie in the Supplemental Material [39]. The periodicity of FH spectral blobs, shown in Fig. 5(b), coincides with those recorded for the TH; however, with a clear onset of fine modulation, represented by much faster oscillations (sub-blobs), superimposed on the main blobs.

Figure 6 presents the results of numerical simulation, which reproduce the experimental data in great detail. The numerical model solves a simplified (one-dimensional) carrier-resolved pulse propagation equation accounting for full material dispersion and instantaneous Kerr nonlinearity. The detailed description of our model can be found elsewhere [42].

Figure 7(a) shows the measured oscillations of TH and FH spectral intensity at 650 nm and 380 nm, respectively, as extracted from Fig. 5. Figure 7(c) presents the corresponding Fourier spectra, which reveal that the FH intensity oscillates at three different frequencies, corresponding to oscillation periods of ~74 μm, ~28 μm, and ~20 μm. The longest (74 μm) oscillation period L_1 coincides with the oscillation period of TH intensity (its coherence length), and the 28 μm period L_2 corresponds to the coherence length of FH generation via the cascaded four-wave sum-frequency generation process $\omega + \omega + 3\omega = 5\omega$; therefore these two periods are the signatures of the cascaded nature of FH generation. The third detected distinct oscillation period of 20 μm L_3 matches the calculated coherence length for FH generation via a pure six-wave-mixing process. On the other hand, it is easy to ascertain that the oscillation period of 20 μm results from the beating between the oscillating TH intensity and FH generation via the cascaded frequency mixing process: $L_3 = L_{\mathrm{beat}} = (1/L_1 + 1/L_2)^{-1} = 20$ μm, which in turn yields the cascaded (effective) fifth-order nonlinearity [41].

Since direct and cascaded FH generation processes provide coincident positions of the coherence peaks, unambiguous determination of their relative contributions requires more extensive analysis. Experimentally, these contributions could be verified by performing the same measurement with higher input-pulse energy and monitoring the ratio of L_2 and L_3 peak amplitudes, and expecting an increase of the L_3 peak due to the increased contribution of the direct FH generation

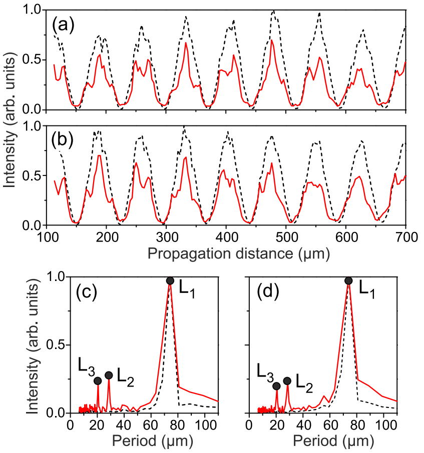

FIG. 7. (Color online) Experimentally measured oscillations of TH (black dashed curves) and FH (red solid curves) spectral intensity versus the propagation distance with the input-pulse energy of (a) 2.8 μJ and (b) 3.8 μJ. TH and FH intensities are not to scale. (c) and (d) show the corresponding Fourier spectra of TH (black dashed curves) and FH (red solid curves) oscillations. Black dots indicate the oscillation periods of the FH.

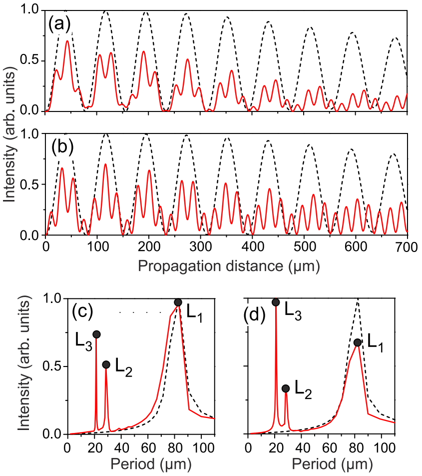

FIG. 8. (Color online) Numerically simulated oscillations of TH (black dashed curves) and FH (red solid curves) spectral intensity versus the propagation distance, using models (a) with cubic nonlinearity only, and (b) with inclusion of quintic nonlinearity. (c) and (d) show the corresponding Fourier spectra of TH (black dashed curves) and FH (red solid curves) oscillations. The input-pulse energy is 3.8 μJ.

process at higher input-pulse intensity. Figures 7(b) and 7(d) present the results obtained with higher input-pulse energy (3.8 μJ), which show that the character of the FH spectral intensity oscillations as well as the amplitudes of the L_2 and L_3 peaks in the Fourier spectra remain fairly the same. However, it must be mentioned that the input-pulse energy range in performing such a measurement is quite limited. Further increase of the input-pulse energy leads to the manifestation of unwanted nonlinear propagation effects: self-focusing of the beam leads to a marked increase of the pulse intensity with propagation, which in turn induces the change of the oscillation period, as can be easily verified from Fig. 2. Self-focusing eventually ends up with supercontinuum generation at the nonlinear focus, which continuously shifts closer to the input face of the sample as the input-pulse energy is increased. The supercontinuum radiation overlaps with the TH and FH signals and completely spoils their oscillatory character.

Therefore we extended our analysis by numerical simulations, performed using a simple model, which accounted for cubic nonlinearity only, and with an updated model, which included the quintic nonlinearity through the higher-order nonlinear refractive index n_4. In the latter simulation we used $n_4 = -2.9 \times 10^{-38}$ m^4/W^2, which was taken to be slightly higher than the value for the cascaded $n_{4,\text{casc}} = -1.4 \times 10^{-38}$ m^4/W^2, as estimated from [41], thus assuming comparable contributions of the direct and cascaded nonlinearities to the FH generation processes. The results of numerical simulations using a model which accounts for cubic nonlinearity only are presented in Figs. 8(a) and 8(c), and favorably compare with the experimental data. In contrast, inclusion of the quintic nonlinearity term in the model reveals some specific features in the FH oscillation series, namely, emergence of FH peaks associated with pure six-wave mixing, which occur at the positions of TH minima, as shown in Fig. 8(b). Furthermore, the Fourier spectra of these oscillation series, as shown in Fig. 8(d), indicate a much stronger amplitude of the L_3 peak, which starts dominating the amplitudes of FH oscillations associated with cubic nonlinearity. Even a simple qualitative comparison with the experiment (see Fig. 7) shows a complete absence of these specific signatures related to direct six-wave mixing in the experimental data.

Note that neither in the experiment nor in the simulation is an oscillation with the period of 49 μm detected, which would be associated with the coherence length of the four-wave difference-frequency mixing process $3\omega + 3\omega - \omega = 5\omega$, suggesting its negligible contribution to FH generation, in line with the results of other related studies [28]. Indeed, the nonlinear polarization, oscillating at the FH frequency in this case is proportional to $\chi^{(3)} E_{\text{TH}}^2 E^*$, where E denotes the complex amplitude of the electric field and is much smaller than that produced by the first cascaded process, which yields a nonlinear polarization proportional to $\chi^{(3)} E^2 E_{\text{TH}}$.

Finally, we carried out measurements and numerical simulations of the harmonics energy as a function of the input-pulse energy and intensity at a fixed propagation length. The

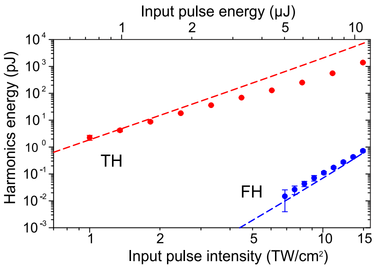

FIG. 9. (Color online) Measured (full circles) and numerically simulated (dashed lines) TH and FH energy as functions of the input-pulse energy and intensity.

measurements were performed over a wide input-pulse energy (intensity) range by setting the propagation length $z = 120\ \mu\text{m}$ in the nonlinear medium, which coincides with the first experimentally accessible energy conversion maximum, and whose shift due to the intensity-dependent phase-matching condition is very small and where nonlinear propagation effects of the beam (self-focusing and filamentation) are still negligible. This in turn guaranteed that there was no supercontinuum generation up to the highest input-pulse energy used. Note that in this measurement we were able to reliably detect the FH signal in a single-shot regime only with input-pulse energy higher than $5\ \mu\text{J}$, whereas in the spectral measurements FH spectra were detected at much lower input-pulse energy due to the possibility of increasing the acquisition time of the spectrometer. Figure 9 shows the measured and numerically simulated trends of TH and FH energy with increasing input-pulse energy (intensity). The energy curves of both harmonics exhibit a power dependence (linear on a log-log scale) and do not saturate in the investigated input-pulse intensity range.

The measured TH energy trend coincides with that obtained from the numerical simulations within the range of low input-pulse energies; however, at high input-pulse energies the measured TH energy values are consistently lower. On the other hand, there is almost perfect agreement between the experimental and numerical data on FH conversion. The disagreement between measured and numerically simulated TH energy at high input-pulse energies could be attributed to limitations of the simplified one-dimensional numerical model; however, the discrepancy obtained is not essential in terms of evaluation of ratio between FH and TH yields, which might serve as an indicator of the role of higher-order Kerr nonlinearities [20]. More precisely, at the highest input-pulse energy of $10.85\ \mu\text{J}$, which is equivalent to an input-pulse intensity of $14.9\ \text{TW/cm}^2$, the measured TH and FH energies were 1.4 nJ and 0.72 pJ, respectively. The corresponding measured TH and FH conversion efficiencies were 1.3×10^{-4} and 6.6×10^{-8}. The experimental values are consistent with data from numerical simulations, which yield TH and FH energies of 7.5 nJ and 0.64 pJ, respectively, and which convert to corresponding energy conversions of 6.8×10^{-4} and 5.8×10^{-8}. The experimental and numerically simulated ratios between FH and TH yields are found as 5.1×10^{-4} and 8.5×10^{-5}, respectively. These results are very much in line with analogous experimental values obtained from filamentation in air [27] and agree with numerical estimations of these parameters using a standard model of intense pulse propagation in a dielectric medium with instantaneous nonlinearity and linear dependence of the refractive index on the intensity [20].

V. CONCLUSIONS

In this work we carried out a detailed experimental and numerical investigation of third- and fifth-harmonic generation in CaF_2 crystals of variable thickness with 20 fs pulses at $2\ \mu\text{m}$. The cross-correlation measurements directly retrieved a double-peaked temporal structure of TH radiation, consisting of free and driven components, which are generated at the boundary of a vacuum and a nonlinear dielectric medium in the conditions of large phase and group-velocity mismatch. The free and driven TH pulses propagate with different group velocities; the temporal separation between the pulses increases with propagation and produces an evolving interference pattern in the TH spectrum. We also demonstrated that the period of the TH energy oscillations (the coherent buildup length) slightly shrinks with an increase of the input-pulse energy (intensity), and the observed change was explained by wave-vector lengthening of the interacting waves due to self- and cross-phase-modulation effects.

A detailed measurements of TH and FH spectra as functions of propagation distance, followed by analysis of TH and FH oscillation periods, and combined with supporting numerical simulations, showed that the FH is generated via cascaded four-wave mixing between the fundamental and third harmonics, $5\omega = 3\omega + \omega + \omega$. A good agreement between the experiments and numerical simulations was obtained when the model accounted for cubic nonlinearity only, whereas the agreement is lost when quintic nonlinearity is included, suggesting that the contribution of pure six-wave mixing due to quintic nonlinearity in the FH generation process is undetectable with input-pulse intensities up to $5\ \text{TW/cm}^2$, which are typical input-pulse intensity values used in filamentation, supercontinuum generation, and self-compression experiments in bulk solid-state media in the midinfrared spectral range [8–11,15,16]. The measured power law of the TH and FH energy dependence on the input-pulse energy along with the related low conversion efficiencies allow the extension of our conclusion regarding the negligible role of higher-order nonlinearities for input-pulse intensities up to $15\ \text{TW/cm}^2$.

ACKNOWLEDGMENTS

This research was funded by the European Social Fund under the Global Grant measure, Grant No. VP1-3.1-ŠMM-07-K-03-001. The authors acknowledge G. Valiulis for useful discussions.

[1] D. Brida, C. Manzoni, G. Cirmi, M. Marangoni, S. Bonora, P. Villoresi, S. De Silvestri, and G. Cerullo, J. Opt. **12**, 013001 (2010).
[2] G. Andriukaitis, T. Balčiūnas, S. Ališauskas, A. Pugžlys, A. Baltuška, T. Popmintchev, M.-C. Chen, M. M. Murnane, and H. C. Kapteyn, Opt. Lett. **36**, 2755 (2011).
[3] J. Biegert, P. K. Bates, and O. Chalus, IEEE J. Sel. Top. Quantum Electron. **18**, 531 (2012).
[4] C. Vozzi, M. Negro, and S. Stagira, J. Mod. Opt. **59**, 1283 (2012).
[5] T. Popmintchev, M.-C. Chen, D. Popmintchev, P. Arpin, S. Brown, S. Ališauskas, G. Andriukaitis, T. Balčiunas, O. D. Mücke, A. Pugžlys, A. Baltuška, B. Shim, S. E. Schrauth, A. Gaeta, C. Hernández-Garcia, L. Plaja, A. Becker, A. Jaron-Becker, M. M. Murnane, and H. C. Kapteyn, Science **336**, 1287 (2012).
[6] S. Ghimire, A. D. DiChiara, E. Sistrunk, P. Agostini, L. F. DiMauro, and D. A. Reis, Nat. Phys. **7**, 138 (2011).
[7] A. D. DiChiara, E. Sistrunk, T. A. Miller, P. Agostini, and L. F. DiMauro, Opt. Express **17**, 20959 (2009).
[8] M. Durand, A. Jarnac, A. Houard, Y. Liu, S. Grabielle, N. Forget, A. Durécu, A. Couairon, and A. Mysyrowicz, Phys. Rev. Lett. **110**, 115003 (2013).
[9] M. Durand, K. Lim, V. Jukna, E. McKee, M. Baudelet, A. Houard, M. Richardson, A. Mysyrowicz, and A. Couairon, Phys. Rev. A **87**, 043820 (2013).
[10] E. O. Smetanina, V. O. Kompanets, A. E. Dormidonov, S. V. Chekalin, and V. P. Kandidov, Laser Phys. Lett. **10**, 105401 (2013).
[11] M. Hemmer, M. Baudisch, A. Thai, A. Couairon, and J. Biegert, Opt. Express **21**, 28095 (2013).
[12] D. Kartashov, S. Ališauskas, A. Pugžlys, A. Voronin, A. Zheltikov, M. Petrarca, P. Béjot, J. Kasparian, J.-P. Wolf, and A. Baltuška, Opt. Lett. **37**, 3456 (2012).
[13] M. Cheng, A. Reynolds, H. Widgren, and M. Khalil, Opt. Lett. **37**, 1787 (2012).
[14] D. Kartashov, S. Ališauskas, A. Pugžlys, A. Voronin, A. Zheltikov, M. Petrarca, P. Béjot, J. Kasparian, J.-P. Wolf, and A. Baltuška, Opt. Lett. **38**, 3194 (2013).
[15] F. Silva, D. R. Austin, A. Thai, M. Baudisch, M. Hemmer, D. Faccio, A. Couairon, and J. Biegert, Nat. Commun. **3**, 807 (2012).
[16] J. Darginavičius, D. Majus, V. Jukna, N. Garejev, G. Valiulis, A. Couairon, and A. Dubietis, Opt. Express **21**, 25210 (2013).
[17] I. Nikolov, A. Gaydardzhiev, I. Buchvarov, P. Tzankov, F. Noack, and V. Petrov, Opt. Lett. **32**, 3342 (2007).
[18] F. Hagemann, O. Gause, L. Wöste, and T. Siebert, Opt. Express **21**, 5536 (2013).
[19] C. Calabrese, A. M. Stingel, L. Shen, and P. B. Petersen, Opt. Lett. **37**, 2265 (2012).
[20] M. Kolesik, E. M. Wright, and J. V. Moloney, Opt. Lett. **35**, 2550 (2010).
[21] M. Kolesik, D. Mirell, J.-C. Diels, and J. V. Moloney, Opt. Lett. **35**, 3685 (2010).
[22] B. Borchers, C. Brée, S. Birkholz, A. Demircan, and G. Steinmeyer, Opt. Lett. **37**, 1541 (2012).
[23] M. Kolesik, E. M. Wright, A. Becker, and J. V. Moloney, Appl. Phys. B: Lasers Opt. **85**, 531 (2006).
[24] N. Akozbek, A. Iwasaki, A. Becker, M. Scalora, S. L. Chin, and C. M. Bowden, Phys. Rev. Lett. **89**, 143901 (2002).
[25] Y. Liu, M. Durand, A. Houard, B. Forestier, A. Couairon, and A. Mysyrowicz, Opt. Commun. **284**, 4706 (2011).
[26] J. Ni, J. Yao, B. Zeng, W. Chu, G. Li, H. Zhang, C. Jing, S. L. Chin, Y. Cheng, and Z. Xu, Phys. Rev. A **84**, 063846 (2011).
[27] G. O. Ariunbold, P. Polynkin, and J. V. Moloney, Opt. Express **20**, 1662 (2012).
[28] D. Kartashov, S. Ališauskas, A. Pugžlys, A. A. Voronin, A. M. Zheltikov, and A. Baltuška, Opt. Lett. **37**, 2268 (2012).
[29] A. Nath, J. A. Dharmadhikari, A. K. Dharmadhikari, and D. Mathur, Opt. Lett. **38**, 2560 (2013).
[30] A. H. Chin, O. G. Calderón, and J. Kono, Phys. Rev. Lett. **86**, 3292 (2001).
[31] R. Zurl and H. Graener, Appl. Phys. B **66**, 213 (1998).
[32] G. Mao, Y. Wu, and K. D. Singer, Opt. Express **15**, 4857 (2007).
[33] K. D. Moll, D. Homoelle, A. L. Gaeta, and R. W. Boyd, Phys. Rev. Lett. **88**, 153901 (2002).
[34] J. Darginavičius, N. Garejev, and A. Dubietis, Opt. Lett. **37**, 4805 (2012).
[35] M. Mlejnek, E. M. Wright, J. V. Moloney, and N. Bloembergen, Phys. Rev. Lett. **83**, 2934 (1999).
[36] V. Roppo, M. Centini, C. Sibilia, M. Bertolotti, D. de Ceglia, M. Scalora, N. Akozbek, M. J. Bloemer, J. W. Haus, O. G. Kosareva, and V. P. Kandidov, Phys. Rev. A **76**, 033829 (2007).
[37] E. Fazio, F. Pettazzi, M. Centini, M. Chauvet, A. Belardini, M. Alonzo, C. Sibilia, M. Bertolotti, and M. Scalora, Opt. Express **17**, 3141 (2009).
[38] G. Valiulis, V. Jukna, O. Jedrkiewicz, M. Clerici, E. Rubino, and P. Di Trapani, Phys. Rev. A **83**, 043834 (2011).
[39] See Supplemental Material at http://link.aps.org/supplemental/10.1103/PhysRevA.89.033846 for the evolution of the interference pattern in the TH spectrum as measured by gradually increasing propagation distance in CaF_2 crystal.
[40] D. Milam, M. J. Weber, and A. J. Glass, Appl. Phys. Lett. **31**, 822 (1977).
[41] M. Bache, F. Eilenberger, and S. Minardi, Opt. Lett. **37**, 4612 (2012).
[42] A. Couairon, E. Brambilla, T. Corti, D. Majus, O. de J. Ramírez-Góngora, and M. Kolesik, Eur. Phys. J. Special Topics **199**, 5 (2011).

A5

ODD HARMONICS-ENHANCED SUPERCONTINUUM IN BULK SOLID-STATE DIELECTRIC MEDIUM

N. Garejev, V. Jukna, G. Tamošauskas, M. Veličkė, R. Šuminas,
A. Couairon, A. Dubietis

Opt. Express **24**, 17060–17068 (2016)

Preprint version reprinted

Odd harmonics-enhanced supercontinuum in bulk solid-state dielectric medium

N. GAREJEV,[1] V. JUKNA,[2] G. TAMOŠAUSKAS,[1] M. VELIČKĖ,[1] R. ŠUMINAS,[1] A. COUAIRON,[3] AND A. DUBIETIS[1,*]

[1] *Department of Quantum Electronics, Vilnius University, Saulėtekio Avenue 10, LT-10223 Vilnius, Lithuania*
[2] *Laboratoire d'Optique Appliquée, ENSTA ParisTech, Ecole Polytechnique, Université Paris-Saclay, F-91762 Palaiseau, France*
[3] *Centre de Physique Théorique, CNRS, Ecole Polytechnique, Université Paris-Saclay, F-91128 Palaiseau, France*
[*] *audrius.dubietis@ff.vu.lt*

Abstract: We report on generation of ultrabroadband, more than 4 octave spanning supercontinuum in thin CaF_2 crystal, as pumped by intense mid-infrared laser pulses with central wavelength of 2.4 μm. The supercontinuum spectrum covers wavelength range from the ultraviolet to the mid-infrared and its short wavelength side is strongly enhanced by cascaded generation of third, fifth and seventh harmonics. Our results capture the transition from Kerr-dominated to plasma-dominated filamentation regime and uncover that in the latter the spectral superbroadening originates from dramatic plasma-induced compression of the driving pulse, which in turn induces broadening of the harmonics spectra due to cross-phase modulation effects. The experimental measurements are backed up by the numerical simulations based on a nonparaxial unidirectional propagation equation for the electric field of the pulse, which accounts for the cubic nonlinearity-induced effects, and which reproduce the experimental data in great detail.

OCIS codes: (190.2620) Harmonic generation and mixing; (190.4380) Nonlinear optics, four-wave mixing; (190.5940) Self-action effects; (320.6629) Supercontinuum generation; (190.7110) Ultrafast nonlinear optics.

References and links

1. A. Braun, G. Korn, X. Liu, D. Du, J. Squier, and G. Mourou, "Self-channeling of high-peak-power femtosecond laser pulses in air," Opt. Lett. **20**, 73–75 (1995).
2. A. Couairon and A. Mysyrowicz, "Femtosecond filamentation in transparent media," Phys. Rep. **441**, 47–189 (2007).
3. F. Silva, D. R. Austin, A. Thai, M. Baudisch, M. Hemmer, D. Faccio, A. Couairon, and J. Biegert, "Multi-octave supercontinuum generation from mid-infrared filamentation in a bulk crystal," Nature Commun. **3**, 807 (2012).
4. J. Darginavičius, D. Majus, V. Jukna, N. Garejev, G. Valiulis, A. Couairon, and A. Dubietis, "Ultrabroadband supercontinuum and third-harmonic generation in bulk solids with two optical-cycle carrier-envelope phase-stable pulses at 2 μm," Opt. Express **21**, 25210–25220 (2013).
5. H. Liang, P. Krogen, R. Grynko, O. Novak, C.-L. Chang, G. J. Stein, D. Weerawarne, B. Shim, F. X. Kärtner, and K.-H. Hong, "Three-octave-spanning supercontinuum generation and sub-two-cycle self-compression of mid-infrared filaments in dielectrics," Opt. Lett. **40**, 1069–1072 (2015).
6. E. O. Smetanina, V. O. Kompanets, A. E. Dormidonov, S. V. Chekalin, and V. P. Kandidov, "Light bullets from near-IR filament in fused silica," Laser Phys. Lett. **10**, 105401 (2013).
7. M. Hemmer, M. Baudisch, A. Thai, A. Couairon, and J. Biegert, "Self-compression to sub-3-cycle duration of mid-infrared optical pulses in dielectrics," Opt. Express **21**, 28095–28102 (2013).
8. I. Gražulevičiūtė, N. Garejev, D. Majus, V. Jukna, G. Tamošauskas, and A Dubietis "Filamentation and light bullet formation dynamics in solid-state dielectric media with weak, moderate and strong anomalous group velocity dispersion," J. Opt. **18**, 025502 (2016).
9. M. Durand, A. Jarnac, A. Houard, Y. Liu, S. Grabielle, N. Forget, A. Durécu, A. Couairon, and A. Mysyrowicz, "Self-guided propagation of ultrashort laser pulses in the anomalous dispersion region of transparent solids: a new regime of filamentation," Phys. Rev. Lett. **110**, 115003 (2013).
10. D. Majus, G. Tamošauskas, I. Gražulevičiūtė, N. Garejev, A. Lotti, A. Couairon, D. Faccio, and A. Dubietis, "Nature of spatiotemporal light bullets in bulk Kerr media," Phys. Rev. Lett. **112**, 193901 (2014).
11. S. V. Chekalin, A. E. Dokukina, A. E. Dormidonov, V. O. Kompanets, E. O. Smetanina, and V. P. Kandidov, "Light bullets from a femtosecond filament," J. Phys. B **48**, 094008 (2015).

12. I. Gražulevičiūtė, R. Šuminas, G. Tamošauskas, A. Couairon, and A. Dubietis, "Carrier-envelope phase-stable spatiotemporal light bullets," Opt. Lett. **40**, 3719–3722 (2015).
13. R. Šuminas, G. Tamošauskas, G. Valiulis, and A. Dubietis, "Spatiotemporal light bullets and supercontinuum generation in β-BBO crystal with competing quadratic and cubic nonlinearities," Opt. Lett. **41**, 2097–2100 (2016).
14. E. O. Smetanina, V. O. Kompanets, S. V. Chekalin, A. E. Dormidonov, and V. P. Kandidov, "Anti-Stokes wing of femtosecond laser filament supercontinuum in fused silica," Opt. Lett. **38**, 16–18 (2013).
15. M. Durand, K. Lim, V. Jukna, E. McKee, M. Baudelet, A. Houard, M. Richardson, A. Mysyrowicz, and A. Couairon, "Blueshifted continuum peaks from filamentation in the anomalous dispersion regime," Phys. Rev. A **87**, 043820 (2013).
16. A. E. Dormidonov, V. O. Kompanets, S. V. Chekalin, and V. P. Kandidov, "Giantically blue-shifted visible light in femtosecond mid-IR filament in fluorides," Opt. Express **23**, 29202–29210 (2015).
17. N. Garejev, I. Gražulevičiūtė, D. Majus, G. Tamošauskas, V. Jukna, A. Couairon, and A. Dubietis, "Third- and fifth-harmonic generation in transparent solids with few-optical-cycle mid-infrared pulses," Phys. Rev. A **89**, 033846 (2014).
18. P. Panagiotopoulos, P. Whalen, M. Kolesik, and J. V. Moloney, "Super high power mid-infrared femtosecond light bullet," Nature Photon. **9**, 543–548 (2015).
19. P. Béjot, G. Karras, F. Billard, E. Hertz, B. Lavorel, E. Cormier, and O. Faucher, "Harmonic generation and nonlinear propagation: when secondary radiations have primary consequences," Phys. Rev. Lett. **112**, 203902 (2014).
20. C. R. Loures, A. Armaroli, and F. Biancalana, "Contribution of third-harmonic and negative-frequency polarization fields to self-phase modulation in nonlinear media," Opt. Lett. **40**, 613–616 (2015).
21. J. Doussot, P. Béjot, and O. Faucher, "Impact of third-harmonic generation on the filamentation process," Phys. Rev. A **93**, 033857 (2016).
22. A. V. Mitrofanov, A. A. Voronin, D. A. Sidorov-Biryukov, A. Pugžlys, E. A. Stepanov, G. Andriukaitis, T. Flöry, S. Ališauskas, A. B. Fedotov, A. Baltuška, and A. M. Zheltikov, "Mid-infrared laser filaments in the atmosphere," Sci. Rep. **5**, 8368 (2015).
23. A. V. Mitrofanov, A. A. Voronin, S. I. Mitryukovskiy, D. A. Sidorov-Biryukov, A. Pugžlys G. Andriukaitis, T. Flöry, E. A. Stepanov, A. B. Fedotov, A. Baltuška, and A. M. Zheltikov, "Mid-infrared-to-mid-ultraviolet supercontinuum enhanced by third-to-fifteenth odd harmonics," Opt. Lett. **40**, 2068–2071 (2015).
24. A. Couairon, E. Brambilla, T. Corti, D. Majus, O. de J. Ramírez-Góngora, and M. Kolesik, "Practitioners' guide to laser pulse propagation models and simulation," Eur. Phys. J. Special Topics **199**, 5–76 (2011).
25. M. Bache, F. Eilenberger, and S. Minardi, "Higher-order Kerr effect and harmonic cascading in gases," Opt. Lett. **37**, 4612–4614 (2012).
26. A. Couairon, J. Biegert, C. P. Hauri, W. Kornelis, F. W. Helbing, U. Keller, and A. Mysyrowicz, "Self-compression of ultra-short laser pulses down to one optical cycle by filamentation," J. Mod. Opt. **53**, 75–85 (2006).
27. K. Lim, M. Durand, M. Baudelet, and M. Richardson, "Transition from linear- to nonlinear-focusing regime in filamentation," Sci. Rep. **4**, 7217 (2014).
28. P. Chessa, E. De Wispelaere, F. Dorchies, V. Malka, J. R. Marques, G. Hamoniaux, P. Mora, and F. Amiranoff, "Temporal and angular resolution of the ionization-induced refraction of a short laser pulse in helium gas," Phys. Rev. Lett. **82**, 552–555 (1999).
29. A. Houard, V. Jukna, G. Point, Y.-B. André, S. Klingebiel, M. Schultze, K. Michel, T. Metzger, and A. Mysyrowicz, "Study of filamentation with a high power high repetition rate ps laser at 1.03 μm," Opt. Express **24**, 7437–7448 (2016).
30. J. Galinis, G. Tamošauskas, I. Gražulevičiūtė, E. Keblytė, V. Jukna, and A. Dubietis, "Filamentation and supercontinuum generation in solid-state dielectric media with picosecond laser pulses," Phys. Rev. A **92**, 033857 (2015).

---

1. Introduction

Self-focusing of intense ultrashort laser pulses in dielectric media leads to a fascinating propagation regime, termed femtosecond filamentation, which was discovered in 1995 [1] and since then has been remaining an active research topic. Femtosecond filaments emerge from the interplay between a wealth of linear and nonlinear effects, while in the simplest approximation filamentary propagation is sustained by a dynamic competition between self-focusing, diffraction, and multiphoton absorption/ionization-induced free electron plasma [2].

In recent years a considerable effort was directed to study filamentation phenomena in solid-state dielectric media with ultrashort mid-infrared laser pulses, that give an access to the range of anomalous group velocity dispersion, where the interplay of self-action effects with anomalous group velocity dispersion facilitates generation of ultrabroadband supercontinuum [3–5], self-compression of the pulse down to few optical cycle duration [5–8] and eventually, formation of propagation invariant spatiotemporal light bullets [6, 9–13]. These studies also uncovered interesting features of the supercontinuum spectra, such as the occurrence of distinct blue peaks, whose spectral shifts vary form large to giant with increasing the input pulse wavelength [14–16]. In addition, they reported on occasional observations of third [3–5, 12] and fifth [17] harmonics, which were detected before the onset of supercontinuum generation.

So far, under typical experimental settings (loose focusing condition) for filamentation in solid-state dielectric media, which refer to Kerr-dominated filamentation regime, the harmonics spectra are overlaid by much more intense supercontinuum emission, and harmonics generation is regarded as an interesting, but generally irrelevant phenomenon. However, recent theoretical and numerical studies suggest that odd harmonics generation may produce a non-negligible impact on the filament propagation dynamics and contribute to spectral broadening [18–21]. In that regard, a supercontinuum in air spanning almost 5 octaves from the mid-infrared to the mid-ultraviolet regions accompanied by enhanced generation of odd-harmonics was recently reported to be induced by filamentation with 3.9 μm, 80 fs laser pulses from a multigigawatt OPCPA system [22, 23].

In this paper we show that odd harmonics generation brings a relevant contribution to spectral superbroadening in a solid-state dielectric medium as the plasma-dominated filamentation regime is accessed. More specifically, such regime is uncovered by self-focusing of 170 fs, 2.4 μm input pulses for short propagation lengths and few TW/cm^2 input intensities in CaF$_2$ crystal, in the absence of optical damage of the nonlinear medium. We demonstrate that plasma-induced compression of the driving pulse induces spectral superbroadening around the carrier wavelength as well as facilitates spectral broadening of third, fifth and seventh harmonics via cross phase modulation, giving rise to the generation of an extremely broadband supercontinuum spanning more than 4 octaves from the ultraviolet to the mid-infrared regions.

2. Experimental setup and numerical model

The experiment was performed using linearly polarized idler pulse with a central wavelength of 2.4 μm, duration of 170 fs and an energy up to 50 μJ from a commercial optical parametric amplifier, OPA (Topas-Prime, Light Conversion Ltd.) pumped by an amplified Ti:sapphire laser system (Spitfire-PRO, Newport-Spectra Physics). The idler beam from an OPA was spatially filtered, suitably attenuated and focused by an f = +100 mm lens into 55 μm FWHM spot located on the input face of CaF$_2$ crystal.

The successive dynamics of harmonics generation and spectral broadening processes was investigated by fine tuning of the crystal length and the input pulse energy (intensity). For that purpose, a wedge-shaped CaF$_2$ sample was mounted on a motorized translation stage and was moved across the input beam, allowing precise scanning of propagation length in the 300 μm-2 mm range. The input energy (intensity) was varied using a neutral metal-coated gradient filter (NDL-25C-2, Thorlabs Inc.) in the $5-35$ μJ ($0.8-5.5$ TW/cm^2) range, which corresponds to a peak power range of $0.7-5.2$ P_{cr}, where $P_{\mathrm{cr}} = 0.15\lambda^2/n_0n_2 = 40$ MW is the critical power for self-focusing in CaF$_2$, with $n_0 = 1.42$ and $n_2 = 1.5 \times 10^{-16}$cm^2/W being linear and nonlinear refractive indexes, respectively. The energies of individual harmonics were measured by dispersing the harmonics beams in space using a fused silica prism with 60° apex angle and by using automated 16-bit digitized detectors: the TH energy was measured using a silicon photodiode SFH 291 (Siemens) with a sensitivity of 0.66 pJ/count, the FH energy was measured using a silicon photodiode BPW 34 B (Osram) with a sensitivity of 1.6 fJ/count, while the SH energy was measured using a photomultiplier tube FEU-84 with a sensitivity of 40 aJ/count. High dynamic range spectral measurements are described in the last section of the paper.

The experimental observations were backed up by the numerical simulations, which were performed using a model based on solving the nonparaxial unidirectional carrier-resolved propagation equation for the electric field E. It is written in the spectral domain and in the local pulse frame [24]:

$$\frac{\partial \tilde{E}}{\partial z} = i(\sqrt{k^2(\omega) - k_\perp^2} - \frac{\omega}{v_g})\tilde{E} + \frac{i\omega}{2\varepsilon_0 c^2 k(\omega)}[\omega \tilde{P} + i\tilde{J}] \tag{1}$$

where $k(\omega) = \omega n(\omega)/c$ is the dispersion relation and $v_g = (\partial k/\partial \omega)^{-1}_{\omega_0}$ is the group velocity of the driving pulse. $\tilde{P}$ and $\tilde{J}$ are the nonlinear polarization and current, respectively, which are expressed as

$$P = \varepsilon_0 \chi^{(3)} E^3, \tag{2}$$

where $\chi^{(3)} = 4\varepsilon_0 c n_2 n_0^2/3$ is the third-order nonlinear optical susceptibility, and

$$J = c\sigma\varepsilon_0(1 + i\omega\tau_c)\rho E + c n_0 \varepsilon_0 \frac{W(I)U_i}{I}(1 - \frac{\rho}{\rho_{nt}})E, \tag{3}$$

where $\rho_{nt} = 2.1 \times 10^{22}$ cm^{-3} is the neutral atom density, $\sigma = 3.47 \times 10^{-21}$ m^2 is the cross section for inverse Bremsstrahlung, $\tau_c = 3$ fs is the electron collision time. We used the Keldysh ionization rates, where $W(I)$ is the ionization rate, calculated as a function of the intensity of the field $I = \varepsilon_0 c n_0 |E|^2/2$, and $U_i = 12$ eV is the bandgap. The plasma density ρ was calculated from the equation:

$$\frac{\partial \rho}{\partial t} = W(I)(\rho_{nt} - \rho) + \frac{\sigma}{U_i}\rho I - \frac{\rho}{\tau_{rec}}, \tag{4}$$

where $\tau_{rec} = 150$ fs is the recombination time.

3. Odd harmonics generation

First of all, under these operating conditions, third (TH), fifth (FH) and seventh (SH) harmonics with center wavelengths of 800 nm, 480 nm and 343 nm, respectively, were experimentally detected and successive dynamics of their energy versus the propagation length z are shown in Figs. 1(a)-1(c). Each data point in the plots represents an average of 40 consecutive laser shots, exposed to the same area of the crystal. The solid white curves mark the range of experimental parameter values (the input pulse intensity and propagation length) above which the optical damage on the output face of the crystal develops after that number of shots, as verified by monitoring an abrupt decrease of harmonics energies due to light scattering from the damage spot and by visual inspection of the crystal volume and output face under white-light illumination using a microscope objective with 10× magnification. We also verified that operation just slightly below that line, e.g. by decreasing the input pulse intensity by 7%, no optical damage of the crystal is observed after exposure of at least 1000 consecutive laser shots at 200 Hz repetition rate with pulse-to-pulse stability of 0.4% rms. Also, at these operating conditions, no apparent signatures that point to formation of color centers (change of crystal color or reduction of the blue shifted part of the spectrum) were detected.

Figures 1(d)-1(f) show the results of the numerical simulations, which reproduce the experimental data in great detail. The evolutions of TH, FH and SH energies versus the propagation distance z show a typical oscillatory behavior, as expected from strongly phase mismatched interactions. Indeed, the measured period of TH energy oscillations (85 μm) in the low intensity limit (with the input pulse intensity below 1 TW/cm^2) well coincides with the calculated double coherent build-up length $2L_{\mathrm{coh}} = 2\pi/|\Delta k| = 91$ μm, where $\Delta k = k(3\omega) - 3k(\omega) = 69.2$ mm^{-1} is the phase mismatch for TH generation in CaF$_2$ with 2.4 μm input pulses. Interestingly, FH and SH energies oscillate with the same period as the TH energy, suggesting that FH and SH are generated by cascaded four-wave mixing processes based on the lowest, i.e. cubic nonlinearity [25]. Indeed, an extensive analysis of the FH oscillation periods performed in an earlier work [17] demonstrated that FH is generated via four-wave mixing between the TH and fundamental harmonics: $5\omega = 3\omega + \omega + \omega$. Similar consideration applies to the SH generation; there are two possible four-wave mixing configurations, which involve either mixing between the fundamental and TH ($7\omega = 3\omega + 3\omega + \omega$) or mixing between the fundamental and FH frequencies ($7\omega = 5\omega + \omega + \omega$). However, the relative contributions of these two processes could not be unambiguously revealed in the present study.

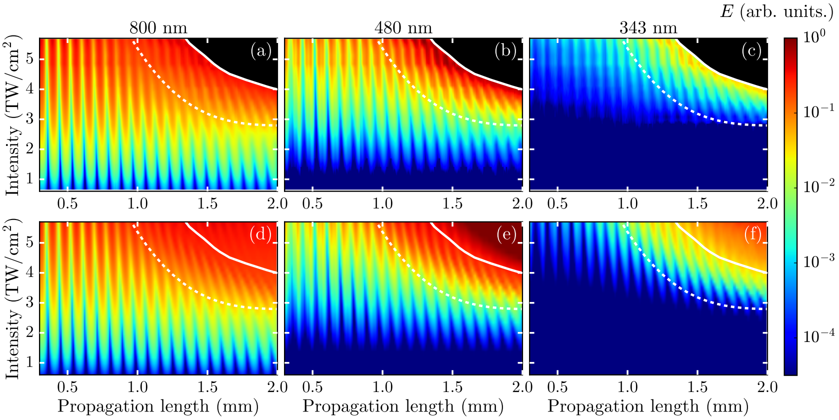

Fig. 1. Experimentally measured (top row) and numerically simulated (bottom row) energies of (a,d) TH, (b,e) FH and (c,f) SH as functions of the driving pulse energy (intensity) and propagation length z. Dashed curves mark a virtual borderline between the Kerr-dominated and plasma-dominated filamentation regimes (see text for details). The black areas in the experimental graphs denote the region of the optical damage that occurs on the output face of the crystal, whose threshold is depicted by a solid curve.

The cascaded origin of harmonics generation is further confirmed by a rapid decrease of the harmonics energy with increasing their order. For instance, with a fixed parameter set (the input pulse intensity of 4.1 TW/cm^2 and $z = 0.31$ mm), the experimentally measured energy conversion efficiencies of TH, FH and SH are 1.9×10^{-4}, 8.7×10^{-8} and 1.4×10^{-11}, respectively, which are the rather typical values for the cascaded harmonics generation process in a solid-state medium. These values agree very well with the numerically computed energy conversion efficiencies that yield 1.6×10^{-4}, 9.7×10^{-8} and 7.8×10^{-11} for TH, TH and SH, respectively. Notice, that the numerical model takes into account the third-order nonlinearity only, and therefore by definition considers the cascading origin of harmonics generation.

More careful inspection of Fig. 1 reveals further interesting features of harmonics generation process. Firstly, TH, FH and SH energy oscillation periods are not constant; they slightly shrink with increasing the input pulse intensity, as evident from slightly tilted harmonics energy oscillation patterns with respect to the vertical axes. The reduction of the oscillation periods is attributed to self- and cross-phase modulation effects [17], which contribute to the changes in the wavevector length of the interacting waves and so the net reduction of the coherent build-up length.

Secondly, there occurs an abrupt change of the tilt angle of harmonics energy oscillation patterns, which coincides with a notable increase of the harmonics (FH and SH, in particular) energies. With increasing the input pulse intensity, a virtual borderline that marks the change of the character of harmonics energy oscillations, shifts closer to the input face of the crystal as highlighted by dashed curves in Fig. 1, which serve as guides for the eye. Figure 2 shows the

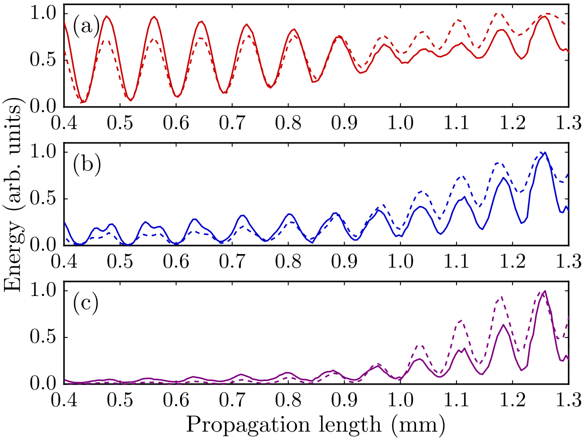

Fig. 2. Energy oscillations of (a) TH, (b) FH and (c) SH as functions of the propagation distance z. Solid and dashed curves represent the experimental and numerical data, respectively. The input pulse intensity is 4.8 TW/cm^2.

experimentally measured and numerically computed harmonics energy oscillations at a fixed input pulse intensity of 4.8 TW/cm^2 in the z range around that virtual borderline in more detail. Figure 2(a) depicts the TH energy oscillations vs z, where an apparent change of the TH oscillation character takes place at around $z = 1$ mm, and thereafter the energy of the TH starts to increase. Similar features are observed in FH and SH energy oscillations, as shown in Figs. 2(b) and 2(c); here however, the growth of FH and SH energies is more dramatic.

4. Spectral broadening and supercontinuum generation

In order to explain the above observations, we refer to the numerically simulated temporal and spectral dynamics presented in Fig. 3. Figure 3(a) shows the evolution of the on-axis intensity profile of the driving pulse at the fundamental frequency. In the early stage of the self-focusing (in the z range below 1 mm) there is just a slight increase of the peak intensity of the driving pulse, without an apparent change of its temporal profile. Thereafter (for $z > 1$ mm) the driving pulse experiences a remarkable (8.5-fold) self-compression from 170 fs to 20 fs, which is induced by rapidly increasing density of the free electron plasma, as shown in Fig. 3(b). The self-compression takes place in the most intense part of the beam, and the self-compressed pulse contains $\sim 10\%$ of the input energy.

Figure 3(c) illustrates the successive evolution of the spectrum, which exhibits a dramatic broadening around the carrier wavelength for $z > 1$ mm, where plasma-induced pulse compression takes place. More interestingly, at the same time the spectra of the individual harmonics experience considerable broadenings as well. The spectral broadening of the individual harmonics may be attributed to the cross-phase modulation induced by an intense driving pulse. Eventually, for longer propagation lengths, $z > 1.4$ mm, the spectral broadenings around the carrier wavelength and the individual harmonics overlap, covering an extremely wide spectral range from the ultraviolet to the mid-infrared.

The temporal and spectral dynamics therefore suitably explain the change in the character of harmonics energy oscillations. A rapid increase of the driving pulse intensity due to plasma-induced compression results in an abrupt reduction of harmonics oscillation periods, as well as in an increase of the harmonics energies. From a more general viewpoint, these findings man-

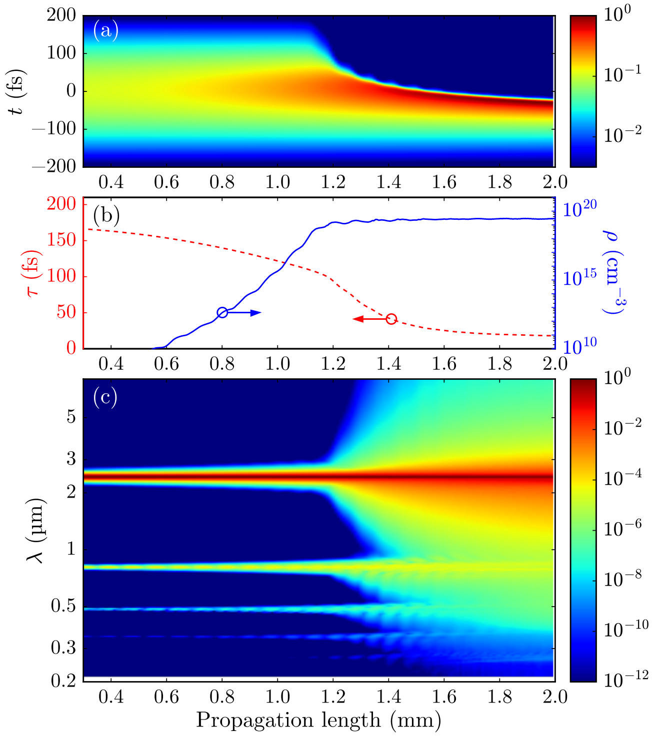

Fig. 3. Numerically simulated dynamics of (a) on-axis intensity profile of the driving pulse at 2.4 μm, (b) pulse duration (red curve) and free electron plasma density (blue curve), and (c) successive evolution of the spectrum. The input pulse intensity is 4.8 TW/cm^2.

ifest the onset of the plasma-dominated filamentation regime, where self-compression of the driving pulse is due to plasma defocusing that pushes the rear part of the pulse out of propagation axis. The plasma-induced pulse compression mechanism is essentially similar to that reported in normally dispersive gaseous media in femtosecond [26, 27] and picosecond [28, 29] filamentation regimes, as well as in normally dispersive solid-state media with picosecond laser pulses [30], where plasma generation results in a catastrophic blow-up of the trailing part of the pulse. Our present findings suggest that, in the first approximation, this compression mechanism is regardless of the sign of group velocity dispersion and is in much contrast to the Kerr-dominated filamentation regime in the range of anomalous group velocity dispersion, where pulse compression is achieved due to opposite effects of self-phase modulation and anomalous group velocity dispersion, see e.g. [6, 9, 10]. In order to justify the negligible role of dispersion, we calculate the nonlinear and dispersive lengths, which are expressed as $L_n = 1/(n_2 k_0 I_0)$ and $L_d = \tau^2_{\mathrm{FWHM}}/(4\ln 2k'')$, respectively, where $k_0 = \omega n_0/c$, I_0 is the pulse intensity, τ_{FWHM} is the pulsewidth and $k'' = d^2k/d\omega^2$. For the input pulse with $\tau_{\mathrm{FWHM}} = 170$ fs and $I_0 = 4.8$ TW/cm^2 we get $L_n = 0.36$ mm and $L_d = 212$ mm. Even if the compressed pulse and the increase of the peak intensity along propagation are taken into account, (e.g. $\tau_{\mathrm{FWHM}} = 25$ fs and $I_0 = 50$ TW/cm^2 at $z = 1.6$ mm), $L_d = 0.46$ mm, which is still larger than the nonlinear length L_n=0.04 mm. Therefore a virtual borderline in Fig. 1, which marks the change in the character of harmonics energy oscillations, in fact indicates the transition from the Kerr-dominated to the plasma-dominated filamentation regimes.

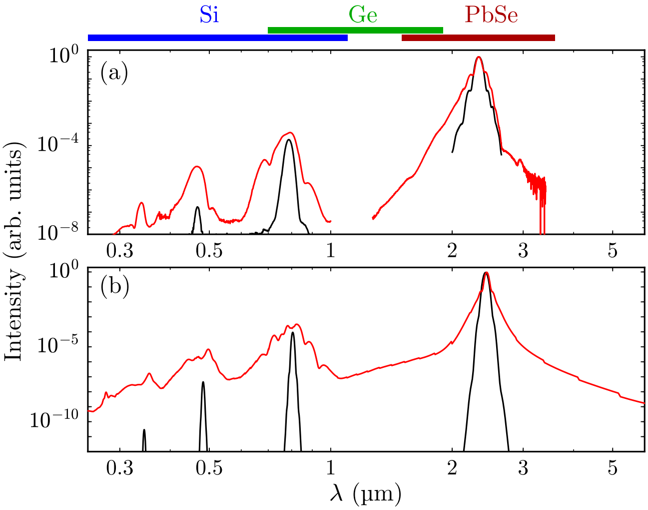

Fig. 4. The output spectra which correspond to Kerr-dominated (black curves) and plasma-dominated (red curves) filamentation regimes: (a) experimental data; here the horizontal bars on the top indicate the spectral regions of the detectors, (b) numerical simulation.

Figure 4 presents the experimentally measured and numerically computed spectra highlighting the relevant spectral features associated with Kerr-dominated and plasma-dominated filamentation regimes, which were accessed for lower input pulse intensity and shorter propagation length (3.4 TW/cm^2, $z = 0.48$ mm) and for higher intensity and longer propagation length (4.1 TW/cm^2, $z = 1.94$ mm), respectively. In the experiment, high dynamic range spectral measurements were performed using a home-built scanning spectrometer with Si, Ge and PbSe detectors, operating in the 0.2-1.1 μm, 0.7-1.9 μm and 1.5-3.6 μm spectral ranges, respectively, as schematically illustrated on the top of Fig. 4(a). The measured spectra where corrected to sensitivity functions of the detectors and transmission of the bandpass optical filters used in the measurement. Finally, spectra from each detector were slightly scaled to achieve consistency in the overlap regions.

In the Kerr-dominated filamentation regime, the output spectrum consists of a series of isolated narrow-band spectral peaks corresponding to the driving pulse and its odd harmonics. In the plasma-dominated filamentation regime, the individual spectral peaks show considerable broadenings, which overlap and merge into an ultrabroadband, multi-octave supercontinuum radiation, which covers the wavelength range from 250 nm in the ultraviolet to more than 7 μm in the mid-infrared (at the 10^{-12} intensity level), approaching the infrared absorption edge of CaF$_2$ crystal. Note that even a broad spectral peak around the ninth harmonics at 267 nm appears in the numerical simulation, as shown in Fig. 4(b); however its energy was beyond the experimental detection range. A good agreement between the experimentally measured and numerically computed spectra is achieved although the experimental spectra were recorded within a reduced dynamic (10^{-8}) and wavelength (from 200 nm to 3.6 μm) ranges, as due to sensitivity limitations of our detection apparatus.

5. Conclusion

In conclusion, we performed experimental and numerical investigation of odd-harmonics and supercontinuum generation with intense mid-infrared femtosecond laser pulses in thin CaF_2 crystal within a wide range of input pulse intensities and propagation lengths. Such a broad operating parameter space allowed us to capture in detail the dynamics of odd harmonics generation and spectral broadening processes, leading to a clear distinction between two filamentation regimes. The Kerr-dominated filamentation regime is detected for low input pulse intensities and short propagation lengths and is characterized by phase-mismatched generation of third, fifth and seventh harmonics with characteristic energy oscillations, which also demonstrate that fifth and seventh harmonics are generated by cascaded four-wave mixing via cubic nonlinearity. In contrast, the plasma-dominated filamentation regime leads to plasma-induced compression of the driving pulse, which in turn induces spectral superbroadening around the carrier wavelength as well as facilitates large scale spectral broadening of third, fifth and seventh harmonics via cross phase modulation, eventually giving rise to the generation of a supercontinuum spanning more than 4 octaves from the ultraviolet to the mid-infrared spectral regions. We believe that the uncovered nonlinear propagation regime is of importance for better understanding the light-matter interaction processes in solid state dielectric media and revealing a debated role of odd-harmonics generation, in particular.

Funding

This research was funded by a grant No. APP-8/2016 from the Research Council of Lithuania.

A6

COMPARATIVE STUDY OF MULTIOCTAVE SUPERCONTINUUM GENERATION IN FUSED SILICA, YAG, AND LiF IN THE RANGE OF ANOMALOUS GROUP VELOCITY DISPERSION

N. Garejev, G. Tamošauskas, A. Dubietis

J. Opt. Soc. Am. B **34**, 88–94 (2017)

Preprint version reprinted

Comparative study of multioctave supercontinuum generation in fused silica, YAG and LiF in the range of anomalous group velocity dispersion

NAIL GAREJEV[1], **GINTARAS TAMOŠAUSKAS**[1], **AND AUDRIUS DUBIETIS**[1,*]

[1] *Department of Quantum Electronics, Vilnius University, Saulėtekio Avenue 10, LT-10223 Vilnius, Lithuania*
[*] *Corresponding author: audrius.dubietis@ff.vu.lt*

Compiled November 18, 2016

We present spectral measurements that uncover the detailed dynamics of the supercontinuum generation in fused silica, YAG and LiF crystals when pumped with 100 fs pulses with a central wavelength of 2.3 μm, which falls into the range of anomalous group velocity dispersion of the media. The multi-octave supercontinuum spectra, which span from the ultraviolet to the mid-infrared, are recorded by means of high-dynamic range measurements over the entire wavelength range covered by the supercontinuum radiation. The spectral dynamics versus the input pulse energy uncovers different mechanisms of spectral broadening, which are characterized by the occurrence of specific, but well-distinguished spectral signatures and which are interpreted in terms of plasma-induced and anomalous group velocity dispersion-induced compression of the driving pulse.

OCIS codes: *(320.6629) Supercontinuum generation; (190.5940) Self-action effects; (190.7110) Ultrafast nonlinear optics.*

http://dx.doi.org/10.1364/ao.XX.XXXXXX

1. INTRODUCTION

The first demonstration of white light generation with femtosecond laser pulses in a bulk medium [1] revealed that a considerable improvement of pulse-to-pulse reproducibility and spatial uniformity of broadband radiation benefits from the short duration of the pump pulse. Since then, femtosecond supercontinuum (SC) became recognized as an indispensable tool for many applications ranging from time-resolved spectroscopy to few optical cycle pulse generation.

The SC generation with femtosecond laser pulses in various solid-state dielectric media in the range of normal group velocity dispersion (GVD) was widely studied experimentally, see e.g. [2–5], and its physical mechanism is fairly well understood in the framework of femtosecond filamentation [6]. In a normally dispersive nonlinear medium, the catastrophic self-focusing is halted by the pulse splitting, which produces wavelength-shifted leading and trailing sub-pulses, and which are responsible for the red-shifted and blue-shifted spectral broadenings, respectively [7–9].

Advances in the near and mid-infrared ultrashort-pulse laser sources, which are exclusively based on optical parametric frequency conversion, provided an access to experimentally investigate femtosecond filamentation and supercontinuum generation phenomena in the range of anomalous GVD of wide bandgap dielectric media. The first experiments performed in this spectral range demonstrated notable extension of the SC spectra in fused silica [10, 11]. These early findings facilitated the discovery of a qualitatively new filamentation regime, where simultaneous compression in space and time leads to formation of quasistationary self-compressed objects – spatiotemporal light bullets [12–16]. Such filamentation conditions yielded multi-octave SC spectra with unprecedented wavelength coverage, as generated in wide bandgap dielectric crystalline materials, such as YAG, sapphire, CaF_2 and BaF_2 [17–22], in water [23], in various types of glasses: fused silica [24–27], BK7 [28], fluoride (ZBLAN) [29], tellurite [30, 31] and chalcogenide glass [32], as well as in birefringent nonlinear crystals, such as DAST [33] and beta-barium borate (BBO) [34]. The numerical simulations suggest that even broader SC spectra could be obtained in sodium chloride and potassium iodide crystals [35]. By tuning the wavelength of the input pulses deeply into the mid-infrared, the ultrabroadband mid-infrared SC was generated by accessing the zero and anomalous GVD range of semiconductor media, such as GaAs [36, 37] and ZnSe [38].

More recently, filamentation of intense femtosecond laser pulses with central wavelength of 3.9 μm in air demonstrated a notable enhancement of the SC spectrum by odd-harmonics generation [39]. Such SC generation regime was also accessed in a thin solid state medium (CaF_2 crystal) under tight focusing condition and uncovered a different scenario of the spectral broadening, which originates from the plasma-induced compression of the driving pulse and subsequent spectral broadening of the individual harmonics peaks via cross-phase modulation, resulting in generation of odd harmonics-enhanced SC, whose spectrum spans over more than 4 octaves [40].

In this paper, we investigate the dynamics of mid-infrared laser pulse-induced spectral broadening and multioctave SC generation in fused silica, yttrium aluminium garnet (YAG) and lithium fluoride (LiF). By increasing the input pulse energy, we capture different mechanisms of spectral broadening, which originate either from plasma-induced or GVD-induced compression of the driving pulse, and which are clearly distinguished by the occurrence of specific spectral features.

2. EXPERIMENTAL SETUP AND MATERIAL PROPERTIES

The experiment was performed using a commercial optical parametric amplifier, OPA (Topas-Prime, Light Conversion Ltd.), pumped by an amplified Ti:sapphire laser system (Spitfire-PRO, Newport-Spectra Physics). The idler pulse from the OPA with a central wavelength of 2.3 μm, duration of 100 fs and an energy up to 50 μJ served as the pump.

The pump beam was spatially filtered, suitably attenuated and focused by an f = +100 mm lens into the focal spot of 30 μm FWHM diameter (NA=0.01). The focal spot was located inside the nonlinear medium; its position was found experimentally so as to achieve the spectral broadening with the lowest input pulse energy. 10-mm long ZnSe crystal was used to compensate the dispersive broadening of the pump pulse in the signal-idler beam separation optics as well as in other optical elements in the beam path. As the nonlinear media, we used thin samples (of 3 mm thickness) of three different wide-bandgap nonlinear dielectric materials: UV-grade fused silica, YAG and LiF, whose relevant linear and nonlinear optical parameters are listed in Table 1. The wavelength of the pump pulse (2.3 μm) was chosen so as to fall into the range of anomalous GVD of all three investigated materials.

Table 1. Linear and nonlinear parameters of UV-grade fused silica, YAG and LiF. n_0 and g are the linear refractive index the GVD coefficient at $\lambda = 2.3$ μm, respectively, E_g is the bandgap energy, λ_0 is the wavelength of zero GVD. T is the transmission range defined at 10% transmission level in 1 mm thick sample [41]. n_2 is the nonlinear refractive index taken from Refs. [12], [18] and [42], respectively, and P_{cr} is the estimated critical power for self-focusing.

	SiO_2	YAG	LiF
E_g, eV	9.0	6.5	13.6
T, μm	$0.16 - 4.0$	$0.21 - 5.2$	$0.12 - 6.6$
n_0	1.43	1.80	1.38
λ_0, μm	1.27	1.61	1.24
g, fs^2/mm	-180	-123	-98
$n_2 \times 10^{-16}$, cm^2/W	2.3	7.0	1.05
P_{cr}, MW	24.1	6.3	54.8

The input pulse energy was varied by using a neutral metal-coated gradient filter (NDL-25C-2, Thorlabs Inc.). High dynamic range spectral measurements were performed with a home-built scanning spectrometer with Si and PbSe detectors, operating in the $0.28 - 1.1$ μm and $0.8 - 4.0$ μm spectral ranges, respectively. The output spectra were collected into the slit of the spectrometer using a pair of Al-coated concave mirrors. The estimated angular acceptance of the spectrometer was ±50 mrad from the beam propagation axis, so the spectrometer captures the on-axis part of the SC and only a fraction of the conical emission. The measured spectra where corrected to sensitivity functions of the detectors and transmission of the bandpass optical filters used in the measurement. Finally, the spectra from each detector were slightly scaled to achieve consistency in the overlap region.

3. RESULTS AND DISCUSSION

A. Fused silica

Fused silica is a versatile material used for a variety of applications in linear and nonlinear optics, so there is no wonder that to date, a large fraction of the SC generation experiments in the range of anomalous GVD were performed in that nonlinear medium [10, 11, 18, 24–27, 43, 44]. These studies uncovered a number of general features, which characterize the SC spectrum. First of all, the angular distribution of the conical emission takes a specific shape, which consists of multiple elliptical structures around the carrier wavelength (in the region of anomalous GVD) and a V-shaped tail in the visible spectral range (in the region of normal GVD) [25, 43, 44]. Secondly, the angle-integrated SC spectrum shows an intense blue-shifted peak in the visible range [18, 24, 25], which is identified as an axial component of the conical emission and whose blue-shift increases with increasing the wavelength of the driving pulse [24, 25]. However, to date and to the best of our knowledge, the entire spectral extent of the SC generated with mid-infrared laser pulses in fused silica was never measured so far.

Figure 1 presents the spectral dynamics versus the input pulse energy, which uncovers two distinct phases of the spectral broadening, which are characterized by the occurrence of specific spectral features and which are attributed to different mechanisms of pulse compression.

In the input pulse energy range of $1.1 - 1.9$ μJ (the power below P_{cr}), we observe a weak third harmonic (TH) peak centered at 767 nm. The TH generation is a simplest third-order nonlinear process, however, due to large phase mismatch, the TH peak is relatively weak [18, 27] and hence is often overlooked in the SC generation experiments, where the dynamic range of the detection apparatus is typically limited to three-four orders of magnitude. Thereafter, in the input pulse energy range of $2.0 - 2.7$ μJ ($0.8 - 1.1$ P_{cr}), an almost symmetric spectral broadening around the carrier wavelength along with dominant blue-shifted spectral broadening of the TH peak is observed. The TH spectrum extends into the visible spectral range and becomes detectable by the naked eye, appearing as a faint red spot, as shown in the inset of Fig. 1. These spectral features are presented in more detail by plotting the lineouts of the spectra in Fig. 2(a). The spectral broadening around the carrier wavelength could be attributed to plasma-induced compression of the driving pulse, where plasma generation results in blow-up of the trailing part of the pulse, in analogy with recent observations in CaF_2 [40]. The blue-shifted spectral broadening of the TH peak could be explained by the difference of the group velocities of the driving and TH pulses: since the driving pulse

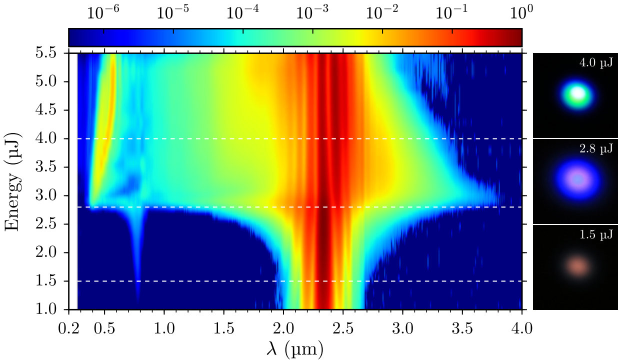

Fig. 1. Spectral broadening in fused silica versus the input pulse energy. The insets on the right show the visual appearance of the output beam in the far field at various stages of spectral broadening. The dimensions of the insets in the following figures are of the same scale.

travels with the largest group velocity, the slower TH pulse shifts toward its trailing front, as a result experiencing large spectral blue shift via cross-phase modulation. Along with spectrally broadened TH, we also capture a very weak spectral peak at 425 nm, which is almost unresolved in Fig. 1, but quite clearly present in Fig. 2(a). That spectral peak corresponds to fifth harmonic, which is generated by the cascaded four wave mixing between the fundamental and TH frequencies [40, 45].

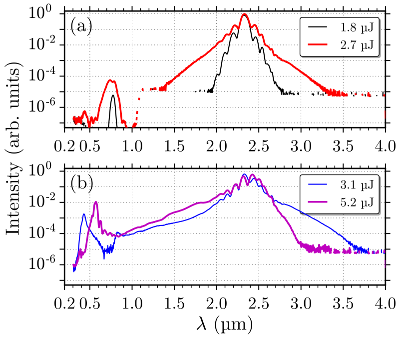

Fig. 2. Characteristic spectra in fused silica, originating from (a) plasma-induced pulse compression, (b) GVD-induced pulse compression and formation of the light bullet. A stepwise change in the background is due to different noise levels of the detectors.

An explosive spectral broadening is observed with the input pulse energy of 2.8 μJ (corresponding to 1.2 P_{cr}), which yields an ultrabroadband SC extending from the ultraviolet (310 nm, at the 10^{-6} intensity level) to the mid-infrared (3.75 μm at the 10^{-5} intensity level). The SC spectrum features the characteristic intense blue-shifted peak, which is centered at 430 nm, while the TH peak becomes quickly masked by much more intense SC emission. Such a broad spectrum is produced by formation of the light bullet, which emerges from simultaneous compression in space due to self-focusing and in time due to opposite effects of self-phase modulation and anomalous GVD [12–16], which is further referred as the regime of GVD-induced pulse compression.

Interestingly, with further increase of the input pulse energy, the central wavelength of the blue peak continuously shifts to longer wavelengths, for instance, to 570 nm at 5.2 μJ, as depicted in Fig. 2(b). The wavelength shift of the blue peak is easily detected by visual means, as evident from the change of the color appearance of the output beam from blue to green, as shown in the inset of Fig. 1, suggesting that the phase matching condition, which yields the position of the blue peak is intensity-dependent. At the same time, we observe gradual shrinking of the mid-infrared part of the SC spectrum. Such peculiar spectral behavior is also observed in other investigated nonlinear media (as will be shown below) and could be attributed to periodic "breathing" nature of propagation of the light bullet [15].

B. YAG

YAG is an attractive nonlinear material because of its high nonlinearity, wide transparency range and high optical damage threshold. In particular, owing to its large nonlinear index of refraction, the SC is generated at reasonably low input pulse energies, as reported with mid-infrared laser pulses with carrier wavelengths of 2 μm [18] and 3 μm [17].

Figure 3 presents the dynamics of the spectral broadening in YAG versus the input pulse energy. In general, in the input pulse energy range of $0.7-2.0$ μJ ($1.1-3.2$ P_{cr}) the spectral dynamics in YAG is qualitatively similar to those observed in fused silica and captures both phases of spectral broadening

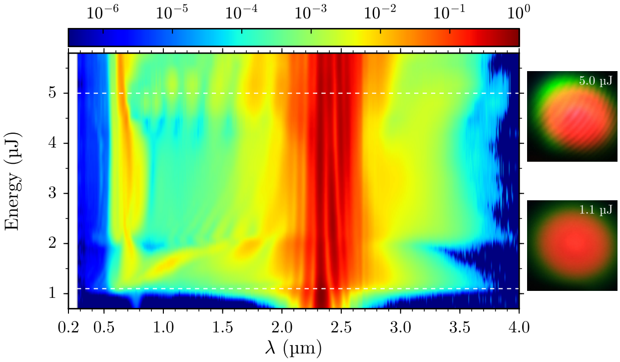

Fig. 3. Spectral broadening in YAG versus the input pulse energy. The insets on the right show the visual appearance of the output beam in the far field at various stages of spectral broadening.

associated with plasma-induced and GVD-induced pulse compression, respectively, as highlighted in more detail in Fig. 4. Figure 4(a) illustrates the characteristic output spectra in the early phase of spectral broadening, associated with plasma-induced compression of the driving pulse. The TH generation at lower input pulse energy is followed by spectral broadenings around the carrier wavelength and the TH peak, which overlap with the input pulse energy of 1.0 μJ. However, owing to very large phase mismatch for TH generation as due to large dispersion of the crystal, the detected TH peak is much weaker than that in fused silica and hence is not observed by visual means.

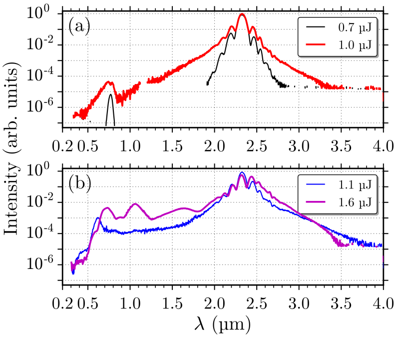

Fig. 4. Characteristic spectra in YAG, originating from (a) plasma-induced pulse compression, (b) GVD-induced pulse compression and formation of the light bullet.

The spectral superbroadening, which is associated with GVD-induced self-compression of the driving pulse and formation of the light bullet, is observed with an input pulse energy of 1.05 μJ, corresponding to the input pulse power of 1.6 P_{cr}. The widest SC spectrum is measured with the input pulse energy of 1.1 μJ and spans from 350 nm to 3.8 μm, with the blue-shifted peak centered at 620 nm, as shown in Fig. 4(b). Notice the apparent differences in the spectral intensities obtained in the plasma-induced and GVD-induced pulse compression regimes and a wide angular distribution of the visible part of the SC produced in the latter, as shown in the inset of Fig. 3 (the angular dimensions of the insets in Fig. 1 and Fig. 3 are to scale).

Thereafter with further increase the input pulse energy up to 2.0 μJ, we observe a narrowing of the SC spectrum as due to the red shift of the blue peak and gradual shrinking of the mid-infrared part. At the same time, in the input pulse energy range of $1.2 - 2.0$ μJ, the SC spectrum shows a development of two distinct spectral humps around 1 μm and 1.7 μm [as shown in more detail in Fig. 4(b)], whose origins are unclear, and which progressively shift toward longer wavelengths with increasing the input pulse energy.

A second boost of the SC spectrum, which is expressed by spectrally broadened and intensified blue peak, as well as intensified mid-infrared portion of the spectrum, is observed with the input pulse energy above 2.1 μJ. However, the spectral intensity of the SC in the $0.9 - 1.5$ μm range becomes notably reduced and shows a development of an interference pattern, which indicates filament refocusing and splitting of the light bullet after a secondary nonlinear focus [27]. Finally, with the input pulse energy above 4 μJ (6.3 P_{cr}), a very clear interference pattern across the visible and near infrared spectral range develops as a result of the filament break-up into two filaments, which also produce the interference fringes in the far field pattern, as illustrated in the inset of Fig. 3.

C. LiF

Although LiF has the largest bandgap among the solid-state dielectric media, formation of long-living color centers resulting from irradiation by intense laser pulses is often considered as a major drawback to its potential applications in nonlinear optics and SC generation in particular. However, recent experiments demonstrate that the color centers only weakly modify the UV portion of the SC spectrum on the long-term time scale [46]. Color centers are also shown to produce intense luminescent tracks in the sample under mid-infrared excitation, which nevertheless do not alter the filamentation process in general [47].

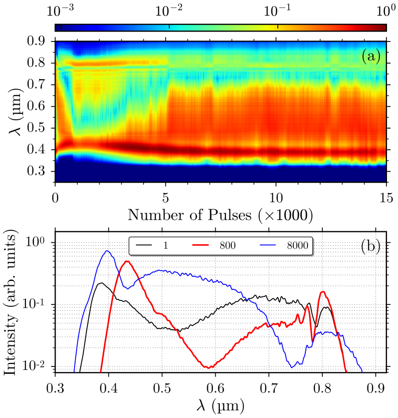

Fig. 5. (a) Time evolution of the ultraviolet-near infrared part of the SC spectrum in LiF as recorded with the input pulse energy of 10.2 μJ. (b) Examples of the individual SC spectra after a different number of laser shots.

Therefore, we first investigated the impact of color center formation on the SC spectrum. The time evolution of the SC spectrum was recorded in the ultraviolet – near infrared spectral range (200-900 nm) using a fiber spectrometer (QE65000, Ocean Optics), which operated in a single shot regime. Figure 5 shows the modification of the SC spectrum as a function of the number of laser shots, as recorded with a fixed input pulse energy of 10.2 μJ.

Formation of the color centers starts almost immediately, after just a few tens of laser shots, as manifested by the changes of the SC spectrum. More specifically, the SC spectrum shows a slight shrinking of its ultraviolet edge, a red shift of the blue peak, an enhancement of the spectral intensity around 800 nm and the occurrence of a prominent spectral dip whose central wavelength is exposure time-dependent. These spectral modifications exhibit rapid evolution with increasing number of laser shots, and the most dramatic change of the SC spectrum is recorded after 800 laser shots, as shown in more detail in Fig. 5(b). Interestingly, thereafter the SC spectrum starts to broaden again and after approximately 5000 laser shots, the shape of the SC spectrum eventually stabilizes and remains unchanged over the rest of the measurement time. The final SC spectrum in a modified crystal shows a marked increase of the spectral intensity in the visible spectral range and even broader ultraviolet extension as compared to that measured in an unmodified crystal, as shown in Fig. 5(b).

These findings suggest that although the color center formation alters the SC spectral shape, the process of spectral broadening and SC generation in a modified volume of the crystal remains almost unaffected. This is verified by studying the dynamics of the spectral broadening in a modified crystal, which captures the above discussed phases of the spectral broadening, associated with plasma-induced and GVD-induced pulse compression, as shown in Fig. 6.

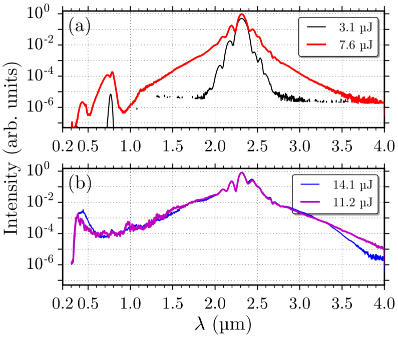

Fig. 7. Characteristic spectra in LiF, originating from (a) plasma-induced pulse compression, (b) GVD-induced pulse compression and formation of the light bullet.

An apparently intense TH peak at 767 nm is readily detected even in the range of low input pulse energies, which correspond to the input pulse power range well below the critical power of self-focusing. Thereafter the plasma-induced pulse compression produces spectral broadenings around the carrier wavelength and TH; the blue shift of the latter makes the TH radiation easily observable by the naked eye, as illustrated in the inset of Fig. 6 and in Fig. 7(a). In the input pulse energy range of $6-8$ μJ, alongside the spectrally broadened TH, we capture a relatively strong peak of fifth harmonic, which experiences spectral broadening as well. Eventually, the spectral broadenings around the carrier, third and fifth harmonic frequencies overlap, resulting in the so-called odd harmonics-enhanced supercontinuum [40].

With an input pulse energy of 8.5 μJ (1.5 $P_{\rm cr}$) an explosive spectral superbroadening due to GVD-induced pulse compression is observed. The broadest SC spectrum, which continuously covers the wavelength range from 290 nm in the ultraviolet to 4.0 μm in the mid infrared, as estimated at the 10^{-6} intensity level, is measured within an input pulse energy range of $9-13$ μJ, see also Fig. 7(b). Since the upper wavelength limit of our spectrometer is 4.0 μm and there is still an appreciable signal of the SC, the wavelength of the mid-infrared cut-off edge of the SC could be extrapolated at $4.3-4.4$ μm. The generated SC spectrum exhibits an intense blue-shifted peak, which is centered at 380 nm. With further increase of the input pulse energy, a slight red shifting of the blue peak along with a slight shrinking of the mid-infrared side of the SC spectrum is observed, as shown in more detail in Fig. 7(b). However, the effect of spectral shrinking in the case of LiF are less pronounced as compared to measurements in fused silica and YAG.

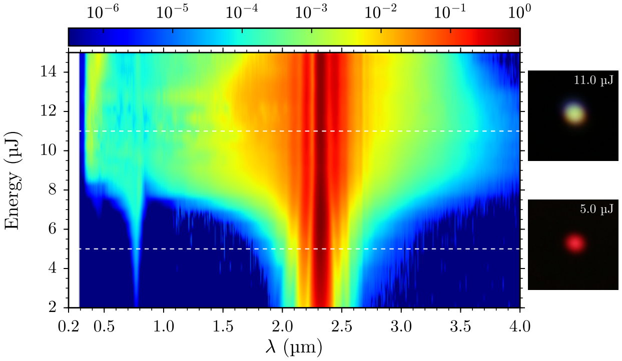

Fig. 6. Spectral broadening in LiF versus the input pulse energy. The insets on the right show the visual appearance of the output beam in the far field at various stages of spectral broadening.

4. CONCLUSION

In conclusion, we investigated the dynamics of spectral broadening and supercontinuum generation in the range of anomalous GVD in fused silica, YAG and LiF nonlinear crystals. High dynamic range measurements were performed over wide spectral range, demonstrating the generation of ultrabroadband, multioctave SC, which continuously covers the wavelength range from the ultraviolet to the mid-infrared, namely, from 310 nm to 3.75 µm (3.6 octaves) in fused silica, from 350 nm to 3.8 µm (3.4 octaves) in YAG and from 290 nm to 4.3 µm (3.9 octaves) in LiF.

The dynamics of the spectral broadening versus the input pulse energy was found to be very similar in all investigated nonlinear media, despite the differences of their relevant linear and nonlinear parameters. The spectral diagnostics uncovered two different phases of spectral broadening, which were characterized by the occurrence of specific spectral signatures and which were interpreted in terms of plasma-induced and anomalous group velocity dispersion-induced compression of the driving pulse. More specifically, the plasma-induced pulse compression, which occurs due to blow-up of the trailing part of the pulse by free electron plasma, produces spectral broadening around the carrier and third (or even fifth, as observed in LiF) harmonic frequencies. Eventually, these spectral broadenings overlap, producing a low intensity broadband radiation in the visible-mid infrared spectral range. In contrast, the group velocity dispersion-induced pulse compression, which originates from the opposite effects of self-phase modulation and anomalous GVD and leads to formation of the light bullets, produces an intense multioctave SC emission, whose spectrum spans from the ultraviolet to the mid-infrared with a characteristic blue peak located in the visible spectral range. We also show that the formation of the color centers in LiF crystal alters the SC spectral shape, however the SC generation process in a modified volume of the crystal remains almost unaffected.

Finally, our measurements demonstrate that under given operating conditions (the input pulsewidth, the length of the nonlinear medium and the focusing condition), there exists an optimum input pulse energy, which produces the broadest SC spectrum, allowing to optimize the practical setups for SC generation with mid-infrared laser pulses.

Funding. Research Council of Lithuania (APP-8/2016).

REFERENCES

1. R. L. Fork, C. V. Shank, C. Hirlimann, R. Yen, and W. J. Tomlinson, "Femtosecond white-light continuum pulses," Opt. Lett. **8**, 1–3 (1983).
2. A. Brodeur and S. L. Chin, "Ultrafast white-light continuum generation and self-focusing in transparent condensed media," J. Opt. Soc. Am. B **16**, 637–650 (1999).
3. C. Nagura, A. Suda, H. Kawano, M. Obara, and K. Midorikawa, "Generation and characterization of ultrafast white-light continuum in condensed media," Appl. Opt. **41**, 3735–3742 (2002).
4. A. K. Dharmadhikari, F. A. Rajgara, and D. Mathur, "Systematic study of highly efficient white-light generation in transparent materials using intense femtosecond pulses," Appl. Phys. B **80**, 61–66 (2005).
5. M. Bradler, P. Baum, and E. Riedle, "Femtosecond continuum generation in bulk laser host materials with sub-µJ pump pulses," Appl. Phys. B **97**, 561–574 (2009).
6. A. Couairon and A. Mysyrowicz, "Femtosecond filamentation in transparent media," Phys. Rep. **441**, 47–189 (2007).
7. G. Fibich and G. C. Papanicolaou, "Self-focusing in the presence of small time dispersion and nonparaxiality," Opt. Lett. **22**, 1397–1399 (1997).
8. A. L. Gaeta, "Catastrophic collapse of ultrashort pulses," Phys. Rev. Lett. **84**, 3582–3585 (2000).
9. D. Faccio, M. A. Porras, A. Dubietis, F. Bragheri, A. Couairon, and P. Di Trapani, "Conical emission, pulse splitting, and X-wave parametric amplification in nonlinear dynamics of ultrashort light pulses," Phys. Rev. Lett. **96**, 193901 (2006).
10. A. Saliminia, S. L. Chin, and R. Vallée, "Ultra-broad and coherent white light generation in silica glass by focused femtosecond pulses at 1.5 µm," Opt. Express **13**, 5731–5738 (2005).
11. M. L. Naudeau, R. J. Law, T. S. Luk, T. R. Nelson, and S. M. Cameron, "Observation of nonlinear optical phenomena in air and fused silica using a 100 GW, 1.54 µm source," Opt. Express **14**, 6194–6200 (2006).
12. M. Durand, A. Jarnac, A. Houard, Y. Liu, S. Grabielle, N. Forget, A. Durécu, A. Couairon, and A. Mysyrowicz, "Self-guided propagation of ultrashort laser pulses in the anomalous dispersion region of transpar-

ent solids: a new regime of filamentation," Phys. Rev. Lett. **110**, 115003 (2013).

13. S. V. Chekalin, V. O. Kompanets, E. O. Smetanina, and V. P. Kandidov, "Light bullets and supercontinuum spectrum during femtosecond pulse filamentation under conditions of anomalous group-velocity dispersion in fused silica," Quantum Electron. **43**, 326–331 (2013).
14. D. Majus, G. Tamošauskas, I. Gražulevičiūtė, N. Garejev, A. Lotti, A. Couairon, D. Faccio, and A. Dubietis, "Nature of spatiotemporal light bullets in bulk Kerr media," Phys. Rev. Lett. **112**, 193901 (2014).
15. S. V. Chekalin, A. E. Dokukina, A. E. Dormidonov, V. O. Kompanets, E. O. Smetanina, and V. P. Kandidov, "Light bullets from a femtosecond filament," J. Phys. B **48**, 094008 (2015).
16. I. Gražulevičiūtė, N. Garejev, D. Majus, V. Jukna, G. Tamošauskas, and A. Dubietis "Filamentation and light bullet formation dynamics in solid-state dielectric media with weak, moderate and strong anomalous group velocity dispersion," J. Opt. **18**, 025502 (2016).
17. F. Silva, D. R. Austin, A. Thai, M. Baudisch, M. Hemmer, D. Faccio, A. Couairon, and J. Biegert, "Multi-octave supercontinuum generation from mid-infrared filamentation in a bulk crystal," Nature Commun. **3**, 807 (2012).
18. J. Darginavičius, D. Majus, V. Jukna, N. Garejev, G. Valiulis, A. Couairon, and A. Dubietis, "Ultrabroadband supercontinuum and third-harmonic generation in bulk solids with two optical-cycle carrier-envelope phase-stable pulses at 2 μm," Opt. Express **21**, 25210–25220 (2013).
19. J. A. Dharmadhikari, R. A. Deshpande, A. Nath, K. Dota, D. Mathur, and A. K. Dharmadhikari, "Effect of group velocity dispersion on supercontinuum generation and filamentation in transparent solids," Appl. Phys. B **117**, 471–479 (2014).
20. H. Liang, P. Krogen, R. Grynko, O. Novak, C.-L. Chang, G. J. Stein, D. Weerawarne, B. Shim, F. X. Kärtner, and K.-H. Hong, "Three-octave-spanning supercontinuum generation and sub-two-cycle self-compression of mid-infrared filaments in dielectrics," Opt. Lett. **40**, 1069–1072 (2015).
21. A. E. Dormidonov, V. O. Kompanets, S. V. Chekalin, and V. P. Kandidov, "Giantically blue-shifted visible light in femtosecond mid-IR filament in fluorides," Opt. Express **23**, 29202–29210 (2015).
22. V. Shumakova, P. Malevich, S. Ališauskas, A. Voronin, A. M. Zheltikov, D. Faccio, D. Kartashov, A. Baltuška, and A. Pugžlys, "Multi-millijoule few-cycle mid-infrared pulses through nonlinear self-compression in bulk," Nature Commun. **7**, 12877 (2016).
23. P. Vasa, J. A. Dharmadhikari, A. K. Dharmadhikari, R. Sharma, M. Singh, and D. Mathur, "Supercontinuum generation in water by intense, femtosecond laser pulses under anomalous chromatic dispersion," Phys. Rev. A **89**, 043834 (2014).
24. E. O. Smetanina, V. O. Kompanets, S. V. Chekalin, A. E. Dormidonov, and V. P. Kandidov, "Anti-Stokes wing of femtosecond laser filament supercontinuum in fused silica," Opt. Lett. **38**, 16–18 (2013).
25. M. Durand, K. Lim, V. Jukna, E. McKee, M. Baudelet, A. Houard, M. Richardson, A. Mysyrowicz, and A. Couairon, "Blueshifted continuum peaks from filamentation in the anomalous dispersion regime," Phys. Rev. A **87**, 043820 (2013).
26. S. V. Chekalin, V. O. Kompanets, A. E. Dokukina, A. E. Dormidonov, E. O. Smetanina, and V. P. Kandidov, Visible supercontinuum radiation of light bullets in the femtosecond filamentation of IR pulses in fused silica, Quantum Electron. **45**, 401–407 (2015).
27. I. Gražulevičiūtė, R. Šuminas, G. Tamošauskas, A. Couairon, and A. Dubietis, "Carrier-envelope phase-stable spatiotemporal light bullets," Opt. Lett. **40**, 3719–3722 (2015).
28. J. Jiang, Y. Zhong, Y. Zheng, Z. Zeng, X. Ge, and R. Li, "Broadening of white-light continuum by filamentation in BK7 glass at its zero-dispersion point," Phys. Lett. A **379**, 1929–1933 (2015).
29. M. Liao, W. Gao, T. Cheng, X. Xue, Z. Duan, D. Deng, H. Kawashima, T. Suzuki, and Y. Ohishi, "Five-octave-spanning supercontinuum generation in fluoride glass," Appl. Phys. Express **6**, 032503 (2013).
30. M. Liao, W. Gao, T. Cheng, Z. Duan, X. Xue, H. Kawashima, T. Suzuki and Y. Ohishi, "Ultrabroad supercontinuum generation through filamentation in tellurite glass," Laser Phys. Lett. **10**, 036002 (2013).
31. P. Béjot, F. Billard, C. Peureux, T. Diard, J. Picot-Clémente, C. Strutynski, P. Mathey, O. Mouawad, O. Faucher, K. Nagasaka, Y. Ohishi, and F. Smektala, "Filamentation-induced spectral broadening and pulse shortening of infrared pulses in Tellurite glass", Opt. Commun. **380**, 245–249 (2016).
32. O. Mouawad, P. Béjot, F. Billard, P. Mathey, B. Kibler, F. Désévédavy, G. Gadret, J.-C. Jules, O. Faucher, and F. Smektala, "Mid-infrared filamentation-induced supercontinuum in As-S and an As-free Ge-S counterpart chalcogenide glasses," Appl. Phys. B **121**, 433–438 (2015).
33. C. Vicario, B Monoszlai, G. Arisholm, and C. P. Hauri, "Generation of 1.5-octave intense infrared pulses by nonlinear interactions in DAST crystal," J. Opt. **17**, 094005 (2015).
34. R. Šuminas, G. Tamošauskas, G. Valiulis, and A. Dubietis, "Spatiotemporal light bullets and supercontinuum generation in β-BBO crystal with competing quadratic and cubic nonlinearities," Opt. Lett. **41**, 2097–2100 (2016).
35. S. A. Frolov, V. I. Trunov, V. E. Leshchenko, and E. V. Pestryakov, "Multi-octave supercontinuum generation with IR radiation filamentation in transparent solid-state media," Appl. Phys. B **122**, 124 (2016).
36. A. A. Lanin, A. A. Voronin, E. A. Stepanov, A. B. Fedotov, and A. M. Zheltikov, "Multioctave, $3-18\ \mu$m sub-two-cycle supercontinua from self-compressing, self-focusing soliton transients in a solid," Opt. Lett. **40**, 974–977 (2015).
37. E. A. Stepanov, A. A. Lanin, A. A. Voronin, A. B. Fedotov, and A. M. Zheltikov, "Solid-state source of subcycle pulses in the midinfrared," Phys. Rev. Lett. **117**, 043901 (2016).
38. O. Mouawad, P. Béjot, F. Billard, P. Mathey, B. Kibler, F. Désévédavy, G. Gadret, J.-C. Jules, O. Faucher, and F. Smektala, "Filament-induced visible-to-mid-IR supercontinuum in a ZnSe crystal: Towards multi-octave supercontinuum absorption spectroscopy," Opt. Mater. **60**, 355–358 (2016).
39. A. V. Mitrofanov, A. A. Voronin, S. I. Mitryukovskiy, D. A. Sidorov-Biryukov, A. Pugžlys, G. Andriukaitis, T. Flöry, E. A. Stepanov, A. B. Fedotov, A. Baltuška, and A. M. Zheltikov, "Mid-infrared-to-mid-ultraviolet supercontinuum enhanced by third-to-fifteenth odd harmonics," Opt. Lett. **40**, 2068–2071 (2015).
40. N. Garejev, V. Jukna, G. Tamošauskas, M. Veličkė, R. Šuminas, A. Couairon, and A. Dubietis, "Odd harmonics-enhanced supercontinuum in bulk solid-state dielectric medium," Opt. Express **24**, 17060–17068 (2016).
41. M. J. Weber, *Handbook of optical materials* (CRC, 2003).
42. D. Milam, M. J. Weber, and A. J. Glass, "Nonlinear refractive index of fluoride crystals," Appl. Phys. Lett. **31**, 822–825 (1977).
43. D. Faccio, A. Averchi, A. Couairon, A. Dubietis, R. Piskarskas, A. Matijošius, F. Bragheri, M. A. Porras, A. Piskarskas, and P. Di Trapani, "Competition between phase-matching and stationarity in Kerr-driven optical pulse filamentation," Phys. Rev. E **74**, 047603 (2006).
44. M. A. Porras, A. Dubietis, A. Matijošius, R. Piskarskas, F. Bragheri, A. Averchi, and P. Di Trapani, "Characterization of conical emission of light filaments in media with anomalous dispersion," J. Opt. Soc. Am. B **24**, 581–584 (2007).
45. N. Garejev, I. Gražulevičiūtė, D. Majus, G. Tamošauskas, V. Jukna, A. Couairon, and A. Dubietis, "Third- and fifth-harmonic generation in transparent solids with few-optical-cycle mid-infrared pulses," Phys. Rev. A **89**, 033846 (2014).
46. J. Kohl-Landgraf, J.-E. Nimsch, and J. Wachtveitl, "LiF, an underestimated supercontinuum source in femtosecond transient absorption spectroscopy," Opt. Express **21**, 17060–17065 (2013).
47. A. V. Kuznetsov, V. O. Kompanets, A. E. Dormidonov, S. V. Chekalin, S. A. Shlenov, and V. P. Kandidov, "Periodic colour-centre structure formed under filamentation of mid-IR femtosecond laser radiation in a LiF crystal," Quantum Electron. **46**, 379–386 (2016).

NOTES

Vilnius University Press
Saulėtekio al. 9, LT-10222 Vilnius
e-mail: info@leidykla.vu.lt,
www.leidykla.vu.lt
Print run copies 15